

An Experimental Test Facility for Studying the Effects of
Turbulence on the Evaporation of Fuel Droplets at
Elevated Pressure and Temperature Conditions

by

Sean Fabbro

A Thesis submitted to the Faculty of Graduate Studies of

The University of Manitoba

in partial fulfilment of the requirements of the degree of

MASTER OF SCIENCE

Department of Mechanical Engineering

University of Manitoba

Winnipeg

Copyright © 2012 by Sean Fabbro

Abstract

A test rig was developed in an effort to perform droplet evaporation and combustion experiments at high levels of turbulent intensity under elevated pressures and temperatures. The detailed explanation of the design and operation of the various components that are part of the testing apparatus is presented. Once the apparatus was completed, 2D Laser Doppler Velocimetry measurements were used to fully characterize the turbulent field inside the chamber. The results showed that the test rig was capable of producing homogenous isotropic turbulence with a 40 mm central region of the chamber at turbulent kinetic energy levels of up to 5.0 m/s. From the characterization data a correlation of turbulent kinetic energy vs fan speed was produced. The produced correlation is valid at standard conditions as well as elevated pressures and temperatures. After determination of the turbulent field, droplet evaporation experiments were performed, first at standard conditions and then elevated temperature and pressure. The results show that turbulence continued to enhance droplet evaporation at elevated temperature and pressures, 298-348°K and 1-21 bar respectively. Broad conclusions are then drawn from the work performed in the study and recommendations are made for future work and improvements to the test apparatus.

Acknowledgements

The author would like to extend his thanks to all of the people who have provided assistance and guidance through out the time spent working on this thesis. Particularly, I would like to extend my deepest gratitude to my supervisor Dr. Birouk for giving me the opportunity and also guiding me throughout the course of this thesis. As well I would also thank my two best friends Joe and Masha Fabbro along with all my other family and friends that have always shown nothing but support for my pursuit of a graduate degree. From the faculty at the university I could not possibly name all of the individuals that have given their time to aiding me in the design and building of the apparatus for this thesis. I would however like to give an extra thanks to the guys in the mechanical engineering machine shop, Irwin Penner and Dan Rossong as well as John Finken, all of whom have put an incredible amount of time into the building of the combustion chamber and who's help and guidance in the design has given me important tools that will serve me well in my future endeavours. I wish also to make a special mention of Dr. Sepehri, Dr Richards and Dr. Kuhn for all their support and knowledge they have given me. It is through their gifts of sharing knowledge and experiences that I have been able to become a better engineer and person.

Table of Contents

Abstract.....	i
Acknowledgements.....	ii
Table of Contents.....	iii
List of Figures.....	v
Nomenclature.....	vi
Chapter 1. Introduction.....	1
Chapter 2: Experimental Facility.....	4
2.1 Introduction.....	4
2.2 Design of a Spherical Turbulence Chamber.....	4
2.2.1 Viewing Ports.....	6
2.2.2 Fan Mounting Ports.....	7
2.2.3 Accessory Ports.....	8
2.2.4 Chamber Leg Assemblies.....	10
2.3 Turbulence Generation and Fan Design.....	11
2.3.1 Fan Transmission Assembly.....	11
2.3.1.1 Transmission Shaft Design.....	13
2.3.1.2 Coupler Design.....	14
2.3.2 Seal Enhancements.....	15
2.3.3 Servomotor Setup.....	16
2.3.3.1 Servomotors.....	16
2.3.3.2 Servo-drives.....	17
2.3.3.3 Servomotor Synchronization.....	17
2.3.4 Fan Design.....	18
2.3.4.1 Fan Design Parameters.....	19
2.3.4.2 Fan Redesign Method and Findings.....	20
2.4 Heating System.....	22
2.4.1 Heating Panel Design.....	23
2.4.2 Heating Panel Arrangement.....	24
2.5 Droplet Suspension System.....	25
2.5.1 Quartz Fibre and Holder.....	26
2.5.2 Injector and Syringe Pump.....	27
2.6 Ignition System.....	28
2.7 Instrumentation and Control.....	29
2.7.1 Sensors and Outputs.....	30
2.7.2 Over Pressure Safety System.....	31
2.7.3 Control Panels.....	30
2.7.3.1 Main Electrical Panel.....	31
2.7.3.2 Electronic & Pneumatic Control Panel.....	32
2.7.3.3 LabView™ Experiment Control Panel.....	34
2.8 Image Capture Set-up and Procedure.....	35
2.9 Image Processing Procedure.....	36
Chapter 3: Results and Discussion.....	37
3.1 Introduction.....	37
3.2 Turbulence Characterization.....	37
3.2.1 Introduction.....	37

3.2.2 Characterization Procedure.....	38
3.2.3 Characterization Results.....	39
3.3 Turbulent Droplet Vaporization.....	42
3.3.1 Introduction.....	42
3.3.2 Experimental Procedure.....	43
3.3.3 Results.....	44
3.3.3.1 Standard Pressures and Temperatures.....	44
3.3.3.2 Elevated Temperatures.....	46
3.3.3.3 Elevated Pressures.....	48
Chapter 4: Conclusions and Recommendations.....	50
4.1 Conclusions.....	50
4.2 Recommendations for Future work.....	50
References.....	53
Appendices.....	56
Appendix A - Seal Manufacturing Procedures.....	A1-2
Appendix B - Matlab Code and Error Calculations.....	B1-7
Appendix C - Drawings.....	C1-53

List of Figures

Figure 2.1.	Schematic diagram of the high-pressure spherical vessel/chamber.....	5
Figure 2.2.	Location of protective windows.....	6
Figure 2.3.	Side view of chamber.....	8
Figure 2.4.	Chamber Flange Arrangement.....	10
Figure 2.5.	Chamber Legs.....	11
Figure 2.6.	Fan Transmission Assembly.....	12
Figure 2.7.	Transmission Shaft Assembly.....	14
Figure 2.8.	Finned Coupler Design.....	15
Figure 2.9a.	Velocity profile of original fan.....	18
Figure 2.9b.	Fan testing rig	18
Figure 2.10.	New Fan Design.....	20
Figure 2.11.	The Original Fan Design.....	20
Figure 2.12.	Picture of adjustable prototype.....	21
Figure 2.13.	New rapid prototype fan blade.....	21
Figure 2.14.	Heating panel stack-up.....	24
Figure 2.15.	Heating plate chamber arrangement.....	25
Figure 2.16.	Quartz filament Assembly.....	27
Figure 2.17.	Injection system with syringe pump.....	28
Figure 2.18.	Wire Element Ignition Head.....	29
Figure 2.19.	Main electrical panel.....	32
Figure 2.20.	Electronic Control Panel.....	33
Figure 2.21.	Electronic Control Sub Panel.....	33
Figure 2.22.	LabView™ Control Panel.....	34
Figure 2.23.	Schematic diagram of image capture setup.....	35
Figure 3.1.	Variation of u'/v' for various fan speeds.....	40
Figure 3.2.	Variation of average turbulence intensity.....	40
Figure 3.3.	Variation of turbulence intensity vs fan speed.....	41
Figure 3.4.	Best Fit for Turbulence Kinetic Energy vs. fan speed.....	42
Figure 3.5.	Normalized squared diameter vs time of n-heptane droplet.....	45
Figure 3.6.	Evaporate rate K vs. RPM at atmospheric pressure.....	46
Figure 3.7.	Evaporation of heptane in elevated temperatures.....	47
Figure 3.8.	Normalized evaporation rate versus fan speed.....	47
Figure 3.9.	Dependency of evaporation rate on pressure and turbulence intensity..	49
Figure 3.10.	Normalized evaporation rates vs. fan speed for various pressures.....	49

Nomenclature

K	Evaporation Rate	(m ² /s)
K ₀	Evaporation rate in quiescent air at standard conditions	(m ² /s)
d	diameter	(mm)
Hz	Frequency in hertz	(1/s)
q	Turbulent kinetic energy	(m ² /s ²)
RPM	Revolutions per minute	(Rev/min)
T	Temperature	(C)
t	Time	(s)
U	Mean velocity in the X direction	(m/s)
V	Mean velocity in the Y direction	(m/s)
u'	Mean fluctuating velocity component in the X direction	(m/s)
v'	Mean fluctuating velocity component in the Y direction	(m/s)
w'	Mean fluctuating velocity component in the Z direction	(m/s)
x	Horizontal distance measured from the centre of the chamber	(mm)
y	Vertical distance measured from the centre of the chamber	(mm)

Chapter 1. Introduction

Modern technological society has become intrinsically dependant on the combustion of liquid fuels to provide the mechanisms that it uses to feed, transport, shelter and sustain its people. Due to the economical scale, even small improvement in the efficiency of combustion systems can represent a significant savings in fuel. These savings provide both direct and indirect benefits to society. The most notable benefits and the motivations for the present study, are environmental impact and monetary savings. Most studies in combustion are driven by one of these two streams of reasoning.

Historically, the majority of knowledge gained in liquid fuel (spray) combustion has been obtained through studying the gasification (via the evaporation and/or combustion) of a single droplet. This started with the pioneering work of Godsave [1] in the early 1950s which led to the development of a theoretical model capable of describing the gasification process of a droplet. The model developed by Godsave [1], which is termed the Quasi-Steady model also known as the d^2 -Law, demonstrated that the square of the droplet diameter decreases linearly with time, as described in Equation (1) of Section 3.3.2. In the same year, Spalding [2] provided additional important insight regarding the various mechanisms governing the droplet heat and mass transfer.

While the original models proposed in the 1950s were very successful in describing the gasification process of a droplet, a tremendous amount of research has been published since (e.g., Faeth [3,4,5]; Law [6]; Sirignano [7]; Williams [8], Ohta [9], Birouk and Gökalp [10], Abramzon and Sirignano[11], Birouk et al.[12], Yang et al.[13], Sato [14], Marchese [15], Yang[16], Sazhin et al. [17], Masoudi and Sirignano[18], Wu et al.

[19], Jangi et al.[20], Pan et al.[21], just to cite a few). While it may seem that the study of an isolated droplet is simple compared to spray combustion, an understanding of its vaporization and combustion is still not completely established. This is because the gasification process of a fuel droplet in a combustion chamber is subjected to numerous interrelated parameters which include flow properties (laminar or turbulent flow), high-pressure and temperature environments, variable composition medium. Moreover, the initial conditions, such as droplet size, have also been found to be an important parameter in gaining thorough understanding of spray combustion (e.g., Abou Al-Sood and Birouk [22]; Chauveau et al.[23], Jackson and Avedisian [24], Monaghan et al. [25]). Recently, there has been significant progress made in understanding the gasification process of a fuel droplet, unfortunately however there is still a lack of data especially under more realistic conditions. In fact, the majority of recently published studies ignored the effect of key flow properties, particularly the effect of turbulence. This lack of data has been mentioned in a number of recent publications (e.g., Abou Al-Sood and Birouk [22,26,27,28], Birouk and Gökalp [10], Birouk et al [12], Morin et al.[29]). The present thesis was initiated with the goal of developing a test facility capable of generating controlled test conditions of practical importance which include pressure, temperature and turbulence of the ambient surroundings of a fuel droplet. As will be described in the next chapter, the test facility used to conduct this research has the ability to generate a high level of turbulence intensity at pressures and temperatures of up to 21 atm and 200°C respectively.

The type of turbulence that is desired for our study has perfect homogeneity over the entire measured volume as well as perfect isotropic. Since perfect homogeneity is not

attainable for the entire region of study, a region that has a mean velocity fluctuation that is within 90% of the value at the centre point will be determined. Since the droplet evaporation and combustion process occurs within a small region of the chamber, if the region of homogeneity that was defined above is significantly larger than the droplet size it is reasonable to conclude that homogeneity testing requirement has been met. It is also important to provide a definition for acceptable isotropy levels. For this thesis an acceptable isotropy level can be defined by the requirement that the u'/v' ratio must be maintained between .90 to 1.10.

The thesis is organized as follows. Chapter 2 provides a detailed description of the test rig designed and manufactured during the course of this study. The turbulence characteristics are then presented for standard as well as elevated pressures and temperatures in Chapter 3. A sample of results on the effect of turbulence on the droplet gasification (via vaporization or combustion) at high pressure and elevated temperature conditions is also presented in Chapter 3. The main findings along with suggestions for future work are then presented in Chapter 4.

Chapter 2: Experimental Facility

2.1 Introduction

The conventional approach to the generation of isotropic and homogenous turbulence is by placing a grid (a perforated plate) downstream of jet flow (e.g., Batchelor and Townsend [30]; Compte-Bellot and Corrsin [31]; Mydlarski and Warhaft [32]). However, this approach was found to produce only low levels of isotropic turbulence (e.g., Birouk et al. [33]). A better approach was found by using pairs of opposed fans inside a chamber. While the original concept used four fans placed symmetrical arranged along the circumference of a cylindrical chamber (e.g. Ohta et al. [9]; Semenov [34]; Fansler and Todd [35]); a novel approach was developed by Birouk et al [12] which consists of eight fans rather than four fans placed symmetrically inside a quasi-spherical vessel. This concept was latter adopted by several research groups (e.g., Meng et la. [36], Fallon et al. [37], de Jong et al. [38]). The eight fans configuration was found to produce improved isotropy (Birouk et al. [10,12, 33, 39]). The vessel configuration and turbulence generation method adopted in this thesis consists of spherical chamber with eight fans to generate turbulence but with the capability of operating at elevated pressures and temperatures. Detail of the apparatus developed in the Energy and Combustion Laboratory (ECL) at the University of Manitoba is presented in the following sections of this chapter.

2.2 Design of a Spherical Turbulence Chamber

The ultimate aim was to design a spherical chamber capable of generating

controlled isotropic homogeneous turbulence under elevated pressure and temperature conditions. The materials and dimensions of the chamber were selected with safety and cost being the limiting factors. The chamber (see Fig. 2.1) has a spherical shape in order to handle the largest pressure possible with the least amount of material. This provides the chamber with the lowest cost and weight while still maintaining a high margin of safety. The original vessel design and analysis was performed by Surminski[60] as part of an undergraduate thesis. The chamber material was selected to be stainless steel due to the corrosion potential inside the chamber from the combustion products. The chamber has an inner and an outer diameter of 380 mm and 405 mm, respectively. The chamber was constructed from two stainless steel hemispheres that were pressed from plate stock and welded together at the seam. The chamber also has four viewing ports, eight mounting flanges for fan blade assemblies and ten accessory ports for sensor and probe access. These ports were welded to the outer wall of the chamber. The chamber was pressure tested after welding to ensure compliance with all regulations governing high pressure experimental testing chambers.

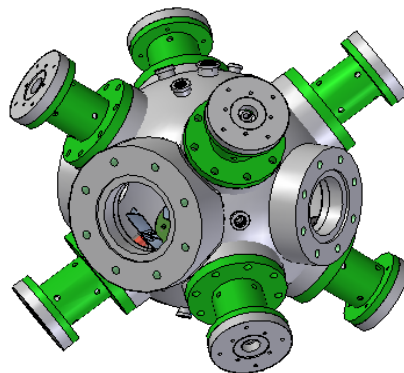


Figure 2.1) Schematic diagram of the high-pressure spherical vessel/chamber

2.2.1 Viewing Ports

There are four viewing ports that are positioned along the equator of the chamber. These viewing ports are equally spaced around the equator, i.e. they are located 90° apart from each other, when viewing the chamber from the top or bottom. Two of these viewing ports are designed to have a five inch inner diameter, and are located 180° apart from each other. The two remaining viewing ports have a four inch inner diameter, and are also located 180° apart from each other. In order to handle high pressure the thickness of the optical quartz glass was selected to be 40 mm. In order to protect the quartz glass from oil deposit, when seeding the airflow inside the chamber, a 6 mm ordinary glass (purchased from a local glass distributor) was installed at the inner side of the viewing ports, as shown schematically in Figure 2.2. These protective glass windows are significantly cheaper compared to quartz glass, and therefore can be regularly replaced after becoming scratched from repetitive cleaning.

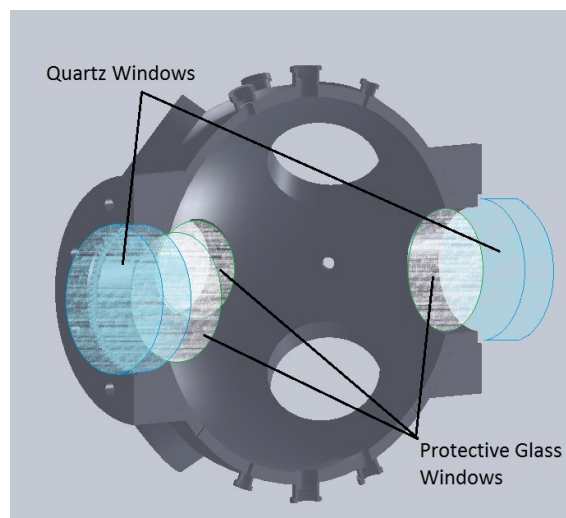


Figure 2.2) Location of protective windows, the windows maintain spherical shape increasing isotropy and homogeneity.

The position of the protective glass, as shown in Figure 2.2, helps to maintain the spherical internal shape of the chamber. The spherical shape is critical in maintaining nearly identical boundary flow conditions. These protective viewing windows are not designed to handle pressure and are vented to the inside of the chamber to equalize the pressure between the two windows. Their main purpose is to act as a shield for the quartz glass from seeding particles and deposition of combustion products.

2.2.2 Fan Mounting Ports

There are eight fan mounting ports located equidistantly about the centre of the chamber. They are located 90° apart from each other, circumferential about the horizontal axis of the chamber, as can be seen in Figure 2.1. In addition, the axis of the fan mounting ports are shifted exactly 45° from the axis of the viewing ports. Symmetrically, four of these ports are located on the 45° South Latitude and are spaced 70° apart from each along the vertical axis of the chamber (see Figure 2.3). Therefore, each fan mounting port faces another fan mounting port located 180° across the chamber. It was important that the fan mounting ports be precisely located to ensure the generation of isotropic and homogeneous turbulence with quasi-zero mean velocity components as discussed in Birouk et al. [10,12, 33, 39].

The inner diameter of the fan mounting ports is precisely four and a half inches, which is critical as it forms a sealing surface for the o-ringed surface of the fan assembly (Figures 2.3 & 2.4). The outer diameter was specified based on certification standards. The outer surface of the fan mounting flanges has an approximate length of $7/8''$ beyond the outer surface of the chamber. Each mounting flange includes eight equally spaced $5/8$ inch fine threaded holes. Studs are inserted into these holes and used to fasten the fan

assembly flanges. Once the flanges of the fan assemblies are in place, nuts are used to lock down the flanges.

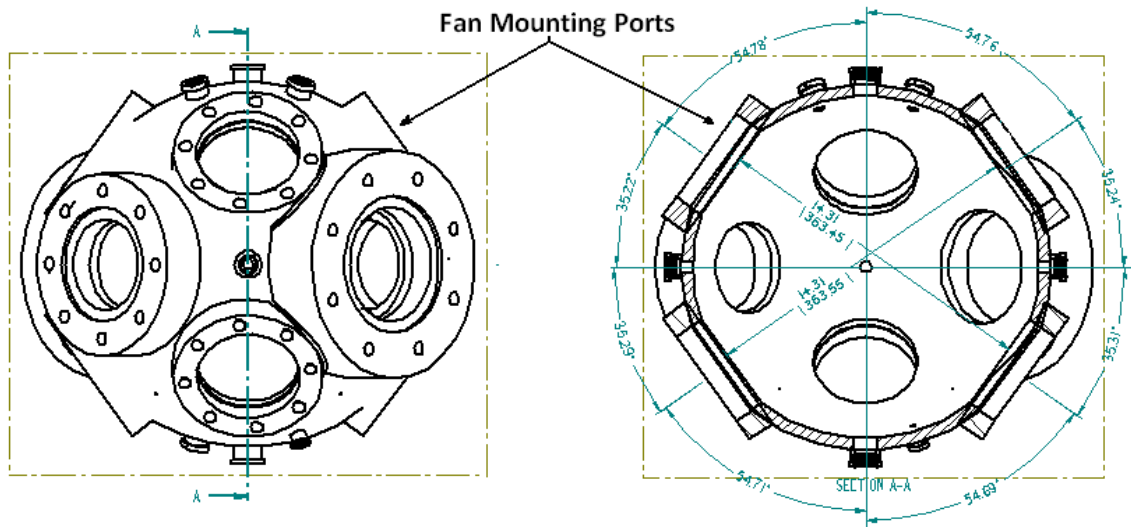


Figure 2.3) Side view of chamber, positioning of the 4.5" mounting ports.

2.2.3 Accessory Ports

There are ten accessory ports mounted onto the surface of the chamber. These ports which can be seen in Figure 2.4, range in size and position depending on their function. The ports can be separated into functional groups and are explained below as to their position and utility.

- The four main accessory ports are located on the equator of the chamber at 45° from the viewing ports. They are equally spaced about the vertical axis of the chamber, such that they are 90° apart from each other. Looking from the top of the chamber, they are located on the same axis as the fan mounting ports. Each has a nominal inner hole size of $5/8$ " and outer flange size of 2.5 inches. They have eight $1/4$ " course

threaded holes equally spaced around a pitch diameter of 1.75 inches.

- One port is located on the very top of the chamber. This port has an extension that is used to hold a quartz fibre in place. This port has a nominal inner hole size of 5/8" and outer flange size of 2.5 inches. The flange for this port has eight 1/4" course threaded holes located equally spaced around a pitch diameter of 1.75 inches.
- One scavenging/exhaust port is located at the bottom of the chamber. This port allows for the drainage of any fluids that may build up as well as the evacuation of gases after testing. This port has a nominal inner hole size of 5/8" and outer flange size of 2.5 inches. The flange for this port has eight 1/4" course threaded holes located equally spaced around a pitch diameter of 1.75 inches.
- Four sensor ports are located along the 67.5° North Latitude (As can be seen in Figure 2.4). They are equally spaced about the vertical axis of the chamber, such that they are 90° apart from each other. From the top view, they are located on the same axis as the viewing ports. The outer diameter of the flanges for these ports are 2.5" and the flange has eight 1/4" course threaded holes equally spaced around a pitch diameter of 1.5 inches.

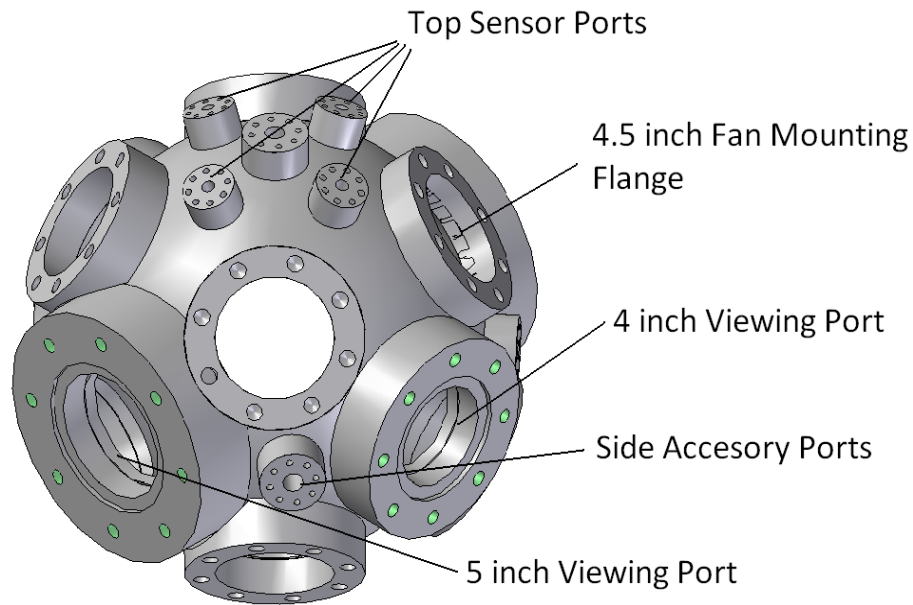


Figure 2.4) Chamber Flange Arrangement

2.2.4 Chamber Leg Assemblies

There are four chamber legs that are located 90° from each other. The chamber legs hold the chamber in position at the four lower fan mounting flanges. When assembled the fan flanges are installed and the chamber is lowered onto the leg assembly, bolts are placed through the legs and fan mounting flanges to secured the chamber to the table. The mounting legs are therefore located along the same axis as the fan mounting ports. The chamber legs are made of mild steel and are approximately 7" x 7" x 1.5". During assembly to facilitate easier assembly the chamber legs are bolted to the chamber first. Then the entire assembly is lowered on the chamber mounting flange adaptor. The adaptor is made of four interlocking steel bars that permits the legs to sit at 10° from the stand which allows for a more stable weight distribution, as shown in below in Figure 2.5.

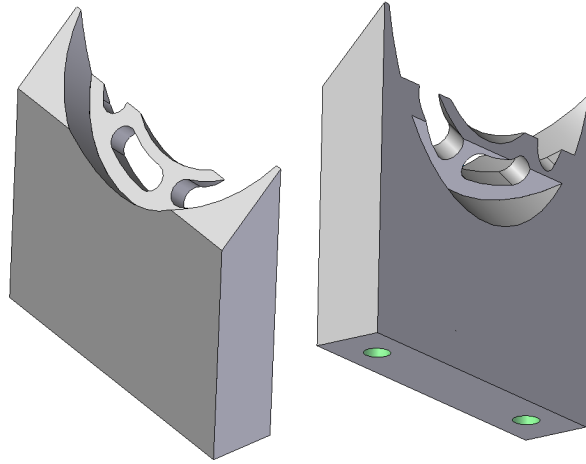


Figure 2.5) Chamber Legs

2.3 Turbulence Generation and Fan Design

Isotropic turbulence is generated in the centre of the vessel by four pairs of axial opposed fans. The front face of the eight six bladed fans are located at a distance of 200 mm across from one to another inside the spherical vessel. Each fan is driven by a servomotor connected through a fan transmission assembly. Details of the servomotor and fan assemblies are provided below.

2.3.1 Fan Transmission Assembly

Due to the high differential pressure between the atmosphere and the gas inside the chamber, as well as the high rotational speed of the shaft (up to 7000 RPM), finding a readily available and reliable industrial sealing method was not possible. To resolve this

issue, a solution was devised which consisted of a two pronged approach. The first was to develop a more robust seal; this design will be discussed in the following section. The second was to devise a system of enhancing the heat transfer from the seal running surface. This heat transfer capability was incorporated directly into the fan transmission assembly. The fan rotation is accomplished through a shaft coupled to a servomotor. Material selection was crucial to attaining this goal but no single material was able to handle all the design requirements mentioned below. Instead the shaft was redesigned into multiple sections as shown in Figure 2.6. This made it possible to attain the necessary surface finish and hardness required on the sealing surface while still providing effective heat transfer.

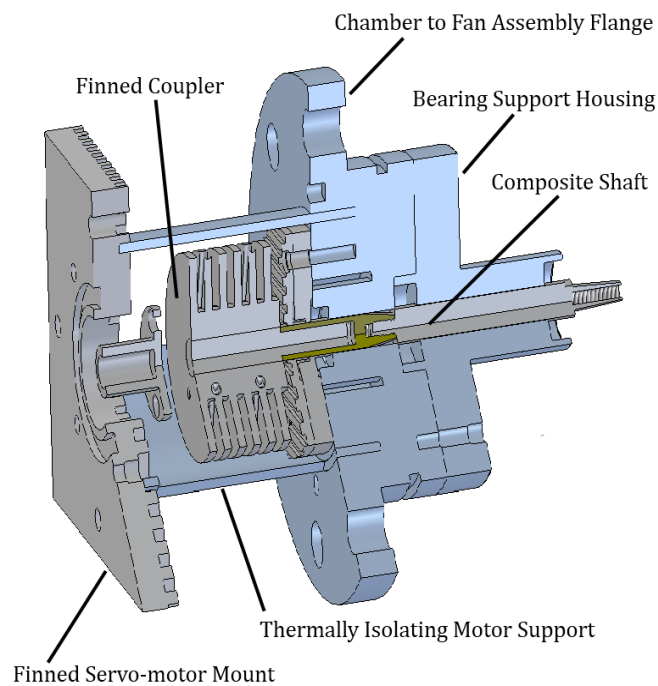


Figure 2.6) Fan Transmission Assembly

2.3.1.1 Transmission Shaft Design

The transmission shaft consists of three sections, as shown in Figure 2.7. The first section is a stainless steel shaft that runs on two alignment bearings. The fan is attached to this section. This section of the shaft was designed to prevent heat transfer from the combustion chamber gases to the sealing surface. Stainless steel was selected for this section because of its poor heat transfer capability and good corrosion resistance. The second section is the seal running surface. This section was required to be very hard but also be able to transfer heat effectively away from the sealing surface. These two requirements could not be met using only one type of material so this section was designed hollow, and a third shaft section was created to be inserted into the hollowed out section. The hardest commercially available material that could be found for the shaft was SAE4340. The middle shaft was then hardened to 60 Rockwell-C and ground to the correct surface finish (Ra of 6 μ in or better). The third shaft was press-fit into the inner diameter of the middle shaft. This inner shaft was made from aluminium which has a high thermal conductivity and would be able to conduct heat away from the hottest area (seal running surface). Effectively the third shaft acts as a heat transfer conduit providing a path for the heat created at the sealing surface to escape via the coupler.

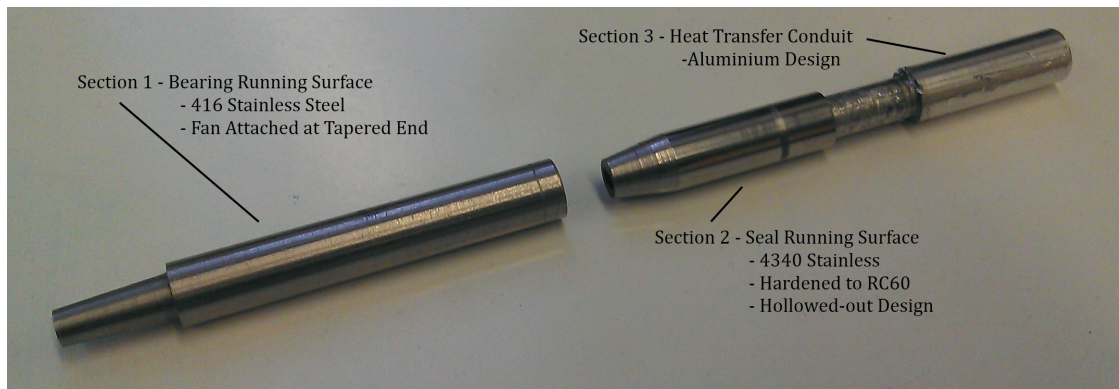


Figure 2.7) *Transmission Shaft Assembly*

2.3.1.2 Coupler Design

In order to remove the heat from the sealing surface via the transmission shaft, the coupler was redesigned. Radial fins were added to the coupler and the coupler material was changed from stainless steel to aluminium in order to facilitate heat transfer to the surroundings (Figure 2.8). An external fan was also added to increase the heat transfer from the coupler to the outside surroundings. The fan was attached to the finned servo-mount seen in Figure 2.6. The use of an external fan was necessary because natural convection alone cannot provide enough cooling at high rotational shaft speeds. Another reason for adding a fan is the limitations imposed by the servomotors maximum ambient temperature of 40°C. Since the fan flow traverses the servo-motors finned mounting flange the fan aids in cooling the motor as well helping to prevent the servomotor from overheating.

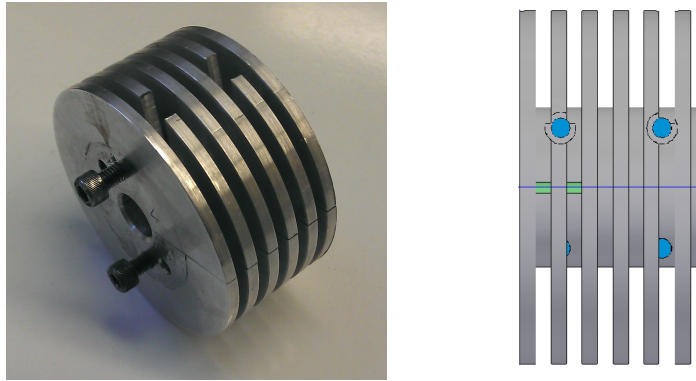


Figure 2.8) Finned Coupler Design for Increased Heat Transfer

2.3.2 Seal Enhancements

There are only a few types of seals commonly used for high rotational speed applications, the ones that were researched for the present application were labyrinth seals, lip seals and carbon seals. Because of the lack of lubrication it quickly became apparent that lip seals were the best choice for this application. Again material selection played an important role. The first seals tested used graphite filled Teflon. These types of seals are common for harsh environments and since graphite has a very low coefficient of friction their use should have helped in decreasing the amount of heat being generated during rotation. Unfortunately, these seals did not perform as expected and after significant testing and research it was found that in certain situations graphite acts as an abrasive instead of lubrication which lead to premature failure. An alternative to graphite filled Teflon was poly-amide filled Teflon. The testing showed a noticeable improvement over graphite but seal failure was still too quick(<8hrs). Analysis of the failed seals showed that the rear sealing surface was always failing first. Testing of a constant width dual lipped seal led to a hypothesis that providing a third lip as well as modifying lip

thickness could prolong service life. However, the only issue with the design requirements generated from the analysis was that these types of seals were not commercially available. This required engineering the process to manufacture the seal with the required dimensions. This led to the development of specialized cutting tools that could create the profiles required. Details of this manufacturing process are provided in Appendix A.

2.3.3 Servomotor Setup

The servomotor setup consists of a motor, feedback device and servomotor drive. Encoders are used as the feedback system for this apparatus. The encoder together with the motor make-up the servomotor unit. The servomotor is driven by a servo-drive that adjusts the power provided to the system ensuring constant rotational speed that is specified by a command signal. Since there are eight independent servomotors, they must all be calibrated to rotate at approximately the same speed. The servomotor system and drives are discussed in the following sections along with the synchronization method used throughout the experiments performed in this study.

2.3.3.1 Servomotors

Servomotor selection was chosen based on rotational speed and torque requirements determined in a undergrad thesis by Surminski[60]. Brush-less servomotors from Servodynamics, Model number HR70E4-32 were selected for the chamber. The HR70E4-32 servomotors have a maximum rotational speed of 8000 RPM and a continuous stall torque of 1.81Nm (16 in•lbs) at a continuous stall current of 4.8 amps

rms. Speed control is provided through encoder model ENC.307 which generates 1000 pulse/second signal.

2.3.3.2 Servo-drives

The 1224-BLS servo-drives selected for this application were recommended by the servomotor provider and includes all of the features required by the initial design requirements of the application. The drives are controlled using a ± 10 volt signal which provides for both positive and negative rotation. The peak power is 7.2 kilowatts which provides enough power to rotate the fans up to a maximum speed of approximately 7700 RPM at 20 atm. The variable rotational fan speed allows for the generation of turbulent flow inside the chamber with different turbulence intensity levels. The complete specifications of the servo-drives are provided in [62].

2.3.3.3 Servomotor Synchronization

These motors are synchronized prior to testing using a digital stroboscope which has an accuracy of 0.1 revolutions per minute. The digital stroboscope is placed in the viewing port of the chamber and set to the test point frequency. The motors are then adjusted to the desired speed using the control panel discussed in LabView™ control panel section. Manual adjustment of the fans is necessary to achieve the same speed for all fans. Fan 1 is adjusted first, then 2 and so on until they are all running at the same speed. The manual adjustment of the servomotor drive amplifiers allows for the synchronization of the fans to approximately ± 5 revolutions per minute. The small amount of error between the fans is considered to be acceptable and represents the error

introduced by using a visual method of calibration.

2.3.4 Fan Design

The initial fan design concept was aimed at moving the largest amount of air possible given the diametrical size constraint. With only a general understanding applied to the design, the fans were successful in generating high turbulence levels even at low rotational speeds. It was found however that the region of homogeneity and isotropy was limited to a central region which was smaller than what was originally expected. Several design attempts were conducted to try to expand the region of isotropic homogenous turbulence including changing rotational direction and installation of glass at the edge of the viewing port. These attempts to expand the region were only marginally successful. However, it was found during testing, in an alternate test rig (Figure 2.9b), that the restriction of airflow created by the fans being close to the chamber wall was effectively limiting the velocity of the flow from the fans.

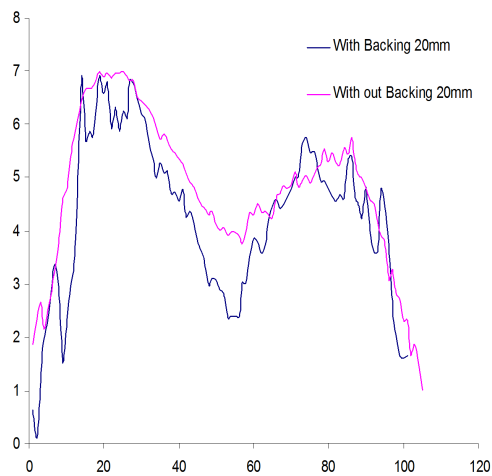


Figure 2.9a) Velocity profile of original fan.

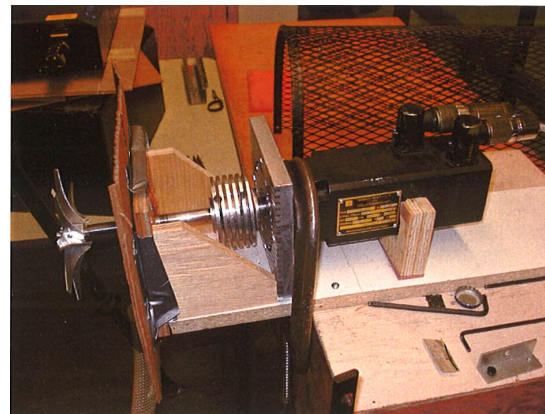


Figure 2.9b) Fan testing rig.

The decreased velocity was most pronounced at the central regions than near the edge of the blades (Figure 2.9a). It was hypothesized that the low velocity at the central region of the fan profile led to the limited central region of isotropic homogenous turbulence. A new fan design was then launched with the aim to generate a constant velocity profile across the entire blade surface (Work performed in an undergrad thesis by Grierson and Grodecki [40]).

2.3.4.1 Fan Design Parameters

A review of pertinent literature on fan design revealed a number of parameters that could aid in optimizing fans that would potentially improve the flatness of the velocity profile downstream of the fan. Amongst the variables found were the following three listed below;

- Cord length - The length of the blade through the centre of the air foil.
- Angle of attack – The angle of the blade relative to its motion.
- Number of blades – The amount of blades that are attached to the centre hub.

The fan blade redesign took advantage of the parameters by varying cord length and angle of attack along the radial direction of the blade so as to even out the velocity profile from tip to hub centre. Also, the number of blades was changed from 4, 6 or 8 in an attempt to maximize the velocity without affecting velocity profile.

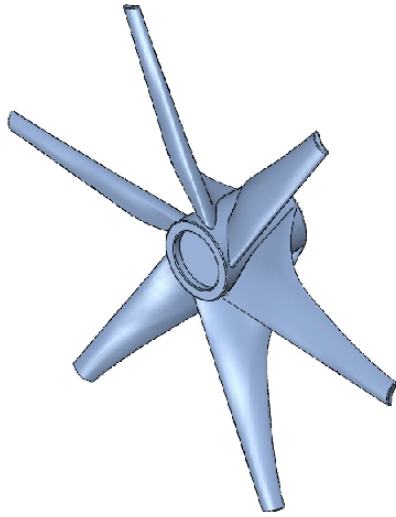


Figure 2.10) *New Fan Design*

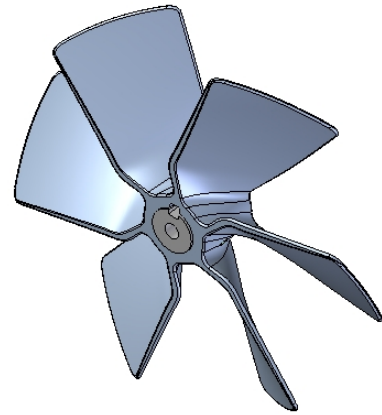


Figure 2.11) *The Original Fan Design*

2.3.4.2 Fan Redesign Method and Findings

In order to expedite the testing of new designs, adjustable prototype fans were made (see Figure 2.12). These fans were able to change angle of attack and number of blades. After analysis of the flows created by a combination of fan blade numbers and angle of attack, the optimum parameters were selected. With these design parameters set, new fixed position fan blades were created using rapid prototyping (see Figure 2.13). The new fan design was then tested inside the combustion chamber and compared with results of the previous/original fan design. Result of the testing showed that the new fans produced a more homogenous turbulence. The better homogeneity however came at the expenses of a large drop in turbulence intensity level. The new fans were therefore found not suitable due to the increased rotational speed that would be required to achieve the desired levels of turbulence intensity. The design of a new set of fan blades, which has a

blend of the old and new features, is still in progress.



Figure 2.12) Picture of adjustable prototype

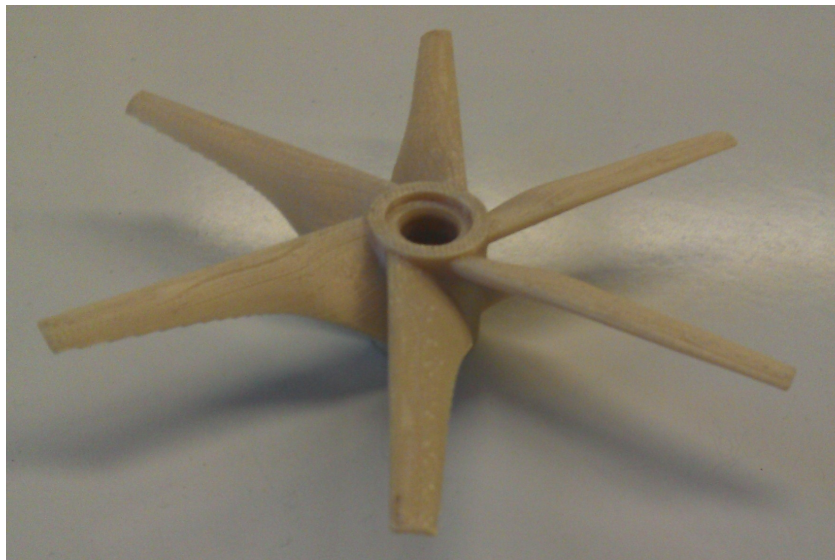


Figure 2.13) New rapid prototype fan blade

2.4 Heating System

The experimental requirements make it necessary to heat the gas inside the chamber to create test conditions that are realistic to many combustion systems. Heating of the chamber was attempted using three different methods and has produced varying degrees of success. The first method used resistance wire which was mounted on ceramic pads inside the chamber. This method achieved the desired air temperatures quickly but could not maintain the chamber temperature for prolonged periods of time due to the high heat loss to the unheated chamber walls. The system also produced non-uniform heat flux which added unknown radiative heating effects. As well, during characterization of the chamber, the exposed elements quickly destroyed the seeding particles via vaporization when flowing near the heating elements. The second method consisted of heating belts that were strapped to the outside wall of the chamber. This method eliminated the non-uniform radiant heat effect and did not interfere with seeding particles inside the chamber. The main disadvantage of this system was the extremely long time required to reach the test temperature. Also, the maximum temperature that could be reached was 80°C. These drawbacks were a consequence of the thick stainless steel chamber walls which meant the large mass of the walls made the heat up period exorbitantly high (8 hours to reach 80°C). Since the heating was from the outside of the chamber, the chamber walls acted like an insulation and thus prevented a high maximum temperature from being reached. The relatively large viewing ports exacerbated the problem, as they act as heat sinks which further reduced the ability of the chamber to reach high temperatures. The third system to be implemented eliminated the drawbacks of both aforementioned systems, producing an even heating that not only raised the air temperature quickly but also provided a high

maximum interior air temperature that could be sustained. This was accomplished by using heating panels that cover the entire interior surface of the chamber, eliminating the loss of heat to the chamber walls. This final design is discussed in detail in the following sections.

2.4.1 Heating Panel Design

The heating panels were made using resistance wire sandwiched between two metal plates (Figure 2.14). The chambers inward facing plates are made from 1/8th inch aluminium metal sheet. The aluminium was selected because of its high thermal conductivity which would help disperse the heat evenly on the interior side of the panel. For the outwards or wall facing plate material, stainless steel was selected. The stainless steel has a poor heat transfer coefficient and would thereby act as an insulation that shields the chamber wall from the heat of the elements. Added heat transfer resistance in the form of a layer of insulation was placed between the wall of the chamber and the heating panel as well as between the heating element and the outward facing plate (Figure 2.14). Because aluminium is conductive, a layer of electrically insulative tape was used between the heating elements and the inner side of the inward facing plate. The tape is made of silica fibre that can withstand high temperatures. This tape does add some heat transfer resistance because it is sandwiched between the electrical wire and inner aluminium plate, but its use could not be avoided since the wire would have shorted out on the inward facing plate without it. The chamber required six different shaped panels to cover the entire inner surface, as indicated by different colours (Figure 2.15). In order to maintain a constant heat flux and thus minimize the non-uniform radiant effect, the length

of wire in each panel was adjusted to match the inward facing surface area of the panel. This ensured that a constant heat flux per unit area was maintained.

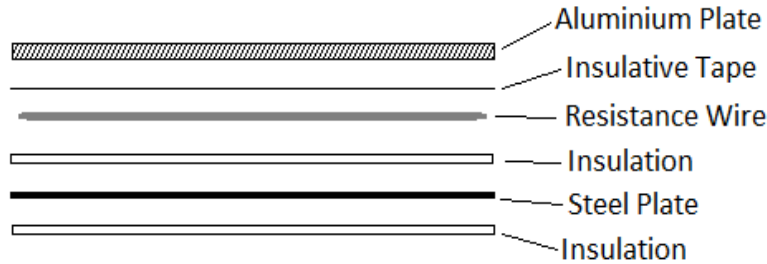


Figure 2.14) Heating panel stack-up.

2.4.2 Heating Panel Arrangement

In order to keep the inside of the chamber as spherical as possible, the largest heating plate of the heating system was designed to be less than five inches in the shortest direction. Four different configurations of heating panels were designed (see Appendix C). Six rows of a single design of panel was placed around the circumference of the chamber and spanned 45° , requiring eight sections of each row to be produced. The entire thirty two panels were inserted one by one into the chamber through the larger viewing port on the front side of the chamber. The panels were installed in six sections from top to bottom and glued in place using a high temperature epoxy (JB-Weld™). Once the panels were installed and soldered together in series they produced a system that has a total resistance of 14.8 ohms. The entire heating system draws 832 watts at 110 volts. The system has been tested at 110 volts which produced a panel surface temperature of over 100°C within 25 minutes and a chamber air temperature of 130°C within an hour.

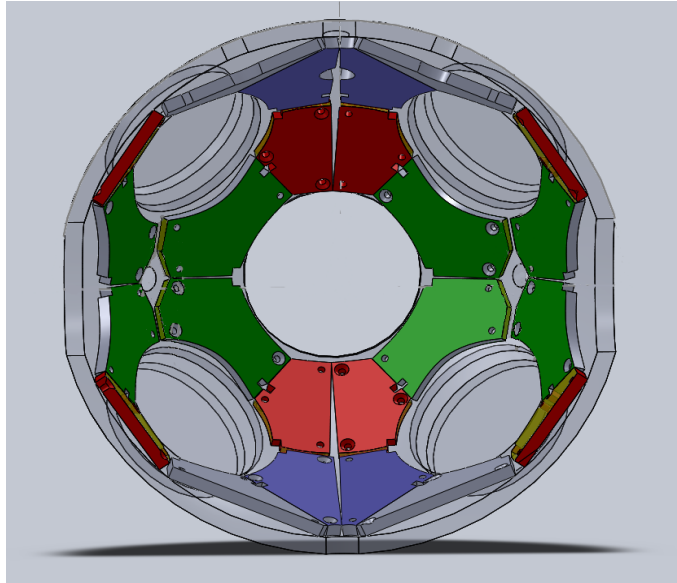


Figure 2.15) Heating plate chamber arrangement

2.5 Droplet Suspension System

One of the most common method of suspension is the use of a quartz filament. A quartz fibre is used because it provides a rigid support even with a very small diameter, it is chemically stable, will not be affected by or take part in combustion, and has a low thermal conduction coefficient. The fibre suspended droplet experiment can be set up easily and since it is stationary, imaging is very simple. The down size of using a quartz fibre is that even though the fibre is quiet small ($\sim 100\mu\text{m}$) it is difficult to suspend a droplet much smaller that 1mm in diameter which is much larger than the average droplet size in a typical spray. Another concern when using quart fibres is that they distort the droplet shape, especially near the end of the droplet's life. Experimentation also showed that there is heat transfer from the flame to the fibre. This creates a heat loss from the flame to the fibre but also a heat gain where the heat is then transferred from the flame

through the fibre to the droplet. Law et al. [41] and Miyasaka and Law [42] have shown that interference from distortion and heat loss can be considered to be negligible during most of the droplets life time for a fibre that is less than 100 μ m. This is supported experimentally by Chauveau et al. [23] as well as Jackson et al. [24]. Another significant limitation of the fibre suspension method is that this method is only feasible for relatively low volatility fuels because of the time required for suspending the droplet and reaching the desired testing conditions. This is a problem that is even more pronounced when multicomponent fuels are used because the fuels composition can be altered from prepared values significantly before testing can occur.

2.5.1 Quartz Fibre and Holder

Droplet formation inside the chamber is accomplished through the interaction of two systems: the quartz fibre and the injector. The fuel droplets are deposited on the tip of a quartz filament suspended in the centre of the combustion chamber (see Figure 2.23). In order for the fibre to be held rigidly a reinforced holder was required. The holder is comprised of a series of cylinders that are sized progressively smaller to allow for the insertion into the previous one. The description of the assembly of the holder is detailed in the next paragraph.

The quartz fibre is epoxied into a supporting needle which is then epoxied into a larger needle in order to make it robust enough to sustain strong flow motions. The second larger needle is then epoxied into a steel sleeve. The steel sleeve fits inside the slot of a rod that projects vertically downward from the top of the chamber. The filament and steel sleeve are held in place by a magnet near the end of the rod. Once the filament

is located at the correct vertical height, the steel sleeve is locked down by a thumb screw on the side of the rod (see Figure 2.16 below).

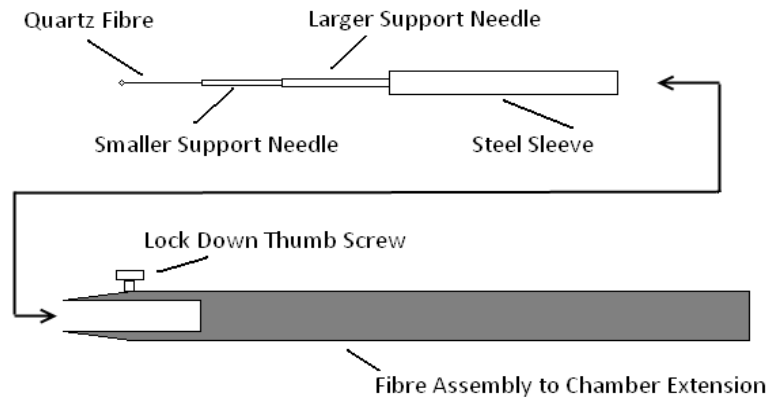


Figure 2.16) Quartz filament Assembly consisting of a Fibre, needle supports and holder.

2.5.2 Injector and Syringe Pump

Fuel droplets are deposited onto the end of the quartz fibre using a retractable injection system. The system is composed of a syringe pump mounted on the end of an actuating tube and cylinder assembly, as shown in Figure 2.17. The fuel is fed through a small diameter tube that runs through the centre of the large support tube. At the end of the tubes is an injection head that supports a small needle used for forming the droplets and two insulated protrusions that hold the ignition leads. The syringe pump used for creating a droplet is a stepper actuated screw drive mechanism attached to 10 ml metal syringe. The stepper is a standard four wire stepper with a 3° full step. The stepper driver is a custom (in-house) made circuit that provides switchable direction capability as well as

step actuation through the generation of pulses. The actuating stepper screw is a ½ inch UNF thread which has a sixteen threads per inch. This produces a single step actuation travel of

$$1/16 \text{ inches} \times 3^\circ/360^\circ = 0.00052 \text{ inches}$$

which provides a volume actuation of

$$0.00052 \text{ inches} \times \pi \times (0.25 \text{ inches})^2 = 0.0001 \text{ inches}^3 \text{ or } 0.0016 \text{ millilitres}$$

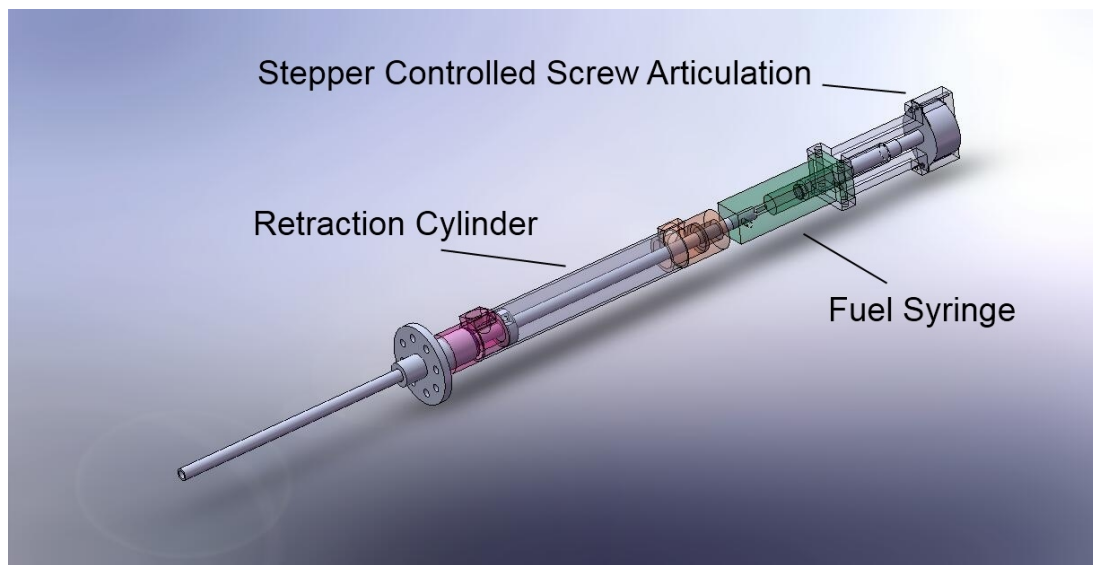


Figure 2.17) Injection system with syringe pump

2.6 Ignition System

In order to be able to study droplet combustion the experimental setup must be capable of igniting a fuel droplet as soon it is formed. Various devices and multiple attempts have been made to produce a reliable ignition system. The main focus of the ignition system centred around the creation of a spark that ignites a fuel droplet. These

attempts were made using a piezoelectric system similar to the ones used in gas barbeques. This type of system was able to ignite more volatile fuels like ethyl alcohol but was not able to ignite hydrocarbons such as heptane. The subsequent attempts were made using an ignition coil setup with various electronic controls. This system was similar to what is available in cars in the 1970's and 1980's. This system was only capable of igniting heptane in still environments and failed to operate consistently in flow conditions. Attempts were made to increase the voltage potential by utilizing more than one coil and different methods of control but no system proved successful. It became obvious that it was not a matter of current or voltage but rather a lack of a combustible fuel mixture around the outer surface of the droplet at ambient temperatures. In order to solve this problem a heating element igniter was designed and manufactured (see Figure 2.18).

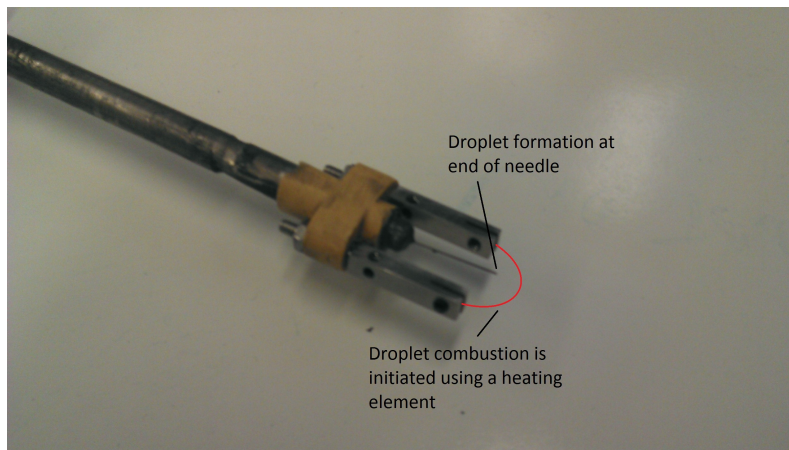


Figure 2.18) *Wire Element Ignition Head.*

2.7 Instrumentation and Control

The instrumentation and control for this combustion chamber are complicated by

the need for various pressure and temperature sensors as well as the required safety systems that are involved with high pressure and temperature testing. The instrumentation is listed in the subsequent sections along with descriptions of the safety systems. As well, illustrations and descriptions are provided for the various control panels that were used to provide control for the apparatus.

2.7.1 Sensors and Outputs

The following is a list of the sensors and controls signals that were connected to the chamber during testing.

- Pressure transducer sensor (millivolt detection)
- Outer wall temperature sensor (thermocouple)
- Inner air temperature sensor (thermocouple)
- Seal temperature sensor (thermocouple)
- leak detector sensor (0-5 Volts)
- 8 – Frequency channels sensors (0-150000Hz)
- Servomotors command signal (0-10volt signal)
- Servomotor enable (5 volt enable signal)

2.7.2 Over Pressure Safety System

A mechanical pressure release valve is attached to the top of the chamber to prevent an over pressure situation. This is backed up by an electronically controlled valve that is actuated by the LabView™ control panel. The control system monitors the pressure using the pressure transducer attached to the chamber and actuates the pneumatic

valve at a set point. The common set point for the chamber safety mechanisms both mechanical and electronic are adjustable; however, in the present thesis' work, it was set to the maximum operational pressure inside the chamber (21 atm).

2.7.3 Control Panels

The combustion chamber requires a set of systems that need to work together to provide the required testing functionality. Each of these systems requires different levels of user control that allow for their adjustment during testing. To accomplish these different functional levels, the controls are broken into three panels. The three panels and their operation are presented in the following three sections along with their layout.

2.7.3.1 Main Electrical Panel

The main electrical panel provides a power lock out for the entire system as well as the master control for the servomotors, servo-drives and heating system (see Figure 2.19). Each of the servo drives are powered and fused through the main panel. The main panel also provides trip detection which is useful for detecting individual motor faults during testing. Along with the switching and fusing capabilities each of the motor drives have thermal protection in case of over heating. The power on function for the heating system is located on the main electrical panel as well. Similar to the servo motor setup the heating system is fused to the required setting and has a trip detect function in the case of a short. Attached to the master electrical panel is a motor isolation sub-panel. The sub-panel allows for the individual isolation of the servo motors. The isolation of individual motors (using the control sub panel switches as indicated in Figure 2.21) is necessary for

trouble shooting wiring problems and may be necessary during some experiments to alter the structure of turbulence in the chamber.

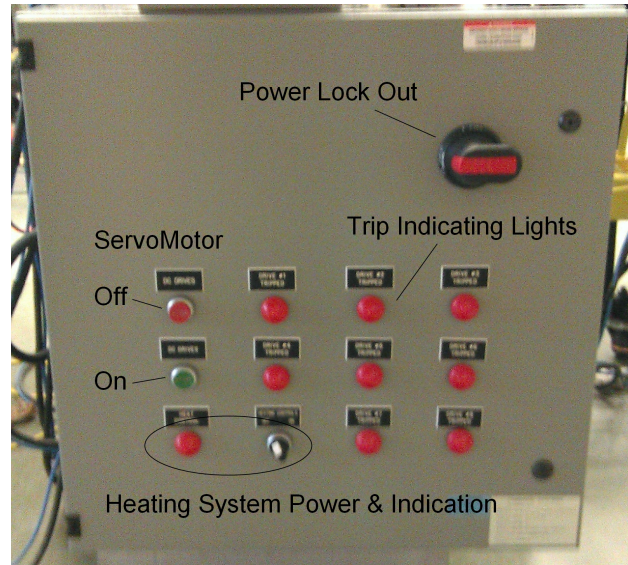


Figure 2.19) Main electrical panel

2.7.3.2 Electronic & Pneumatic Control Panel

The electronic control panel provides access to each of the sensor wires and low power accessory wires that are used on the chamber. The main sensor wires from the data acquisition system are connected to terminal blocks mounted on the control panel. This provides easy fault isolation and the ability to add and remove sensors as necessary without rewiring the entire panel. The use of power bars on the panel allows for the supply of 12 volts to various sensors and the cooling fans that are used on the fan assemblies (as shown in Figure 2.20). Along with the electronic systems the pneumatic leak-detection system is mounted to the panel. This system is comprised of eight low pressure lines that are fed into a collecting manifold. This manifold is then fed into a 0-100 ml thermal mass flow meter that is also located on the control panel (see Figure 2.20).

When in normal operation all of the eight lines are fed together to the flow meter which acts as a leak detector. When a larger total flow is detected the manifold is adjustable to allow for the diversion of each of the eight lines so that individual line fault detection can be performed.

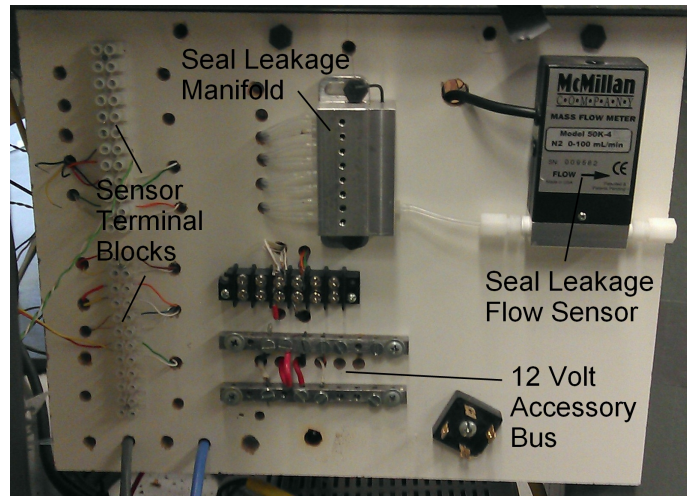


Figure 2.20) Electronic Control Panel

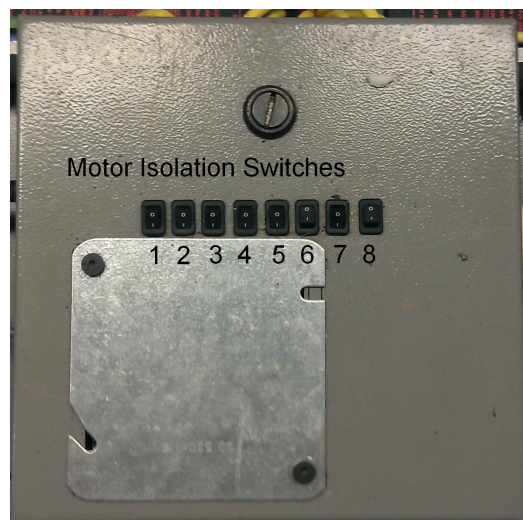


Figure 2.21) Electronic Control Sub Pane

2.7.3.3 LabView™ Experiment Control Panel

The experimental control panel provides the monitoring interface and experimental system control for the entire apparatus (combustion chamber facility). Using the main panel on the computer screen each of the sensors can be monitored as well as the control of the fan speed and actuation of the various injection and ignition components. Because the control panel is configurable and automation capable, the experiment control panel has the potential to provide high speed synchronization between systems. This makes experiments that could not previously be accomplished due to the slow reaction times of the human operators, now realizable with the use of precision timing.

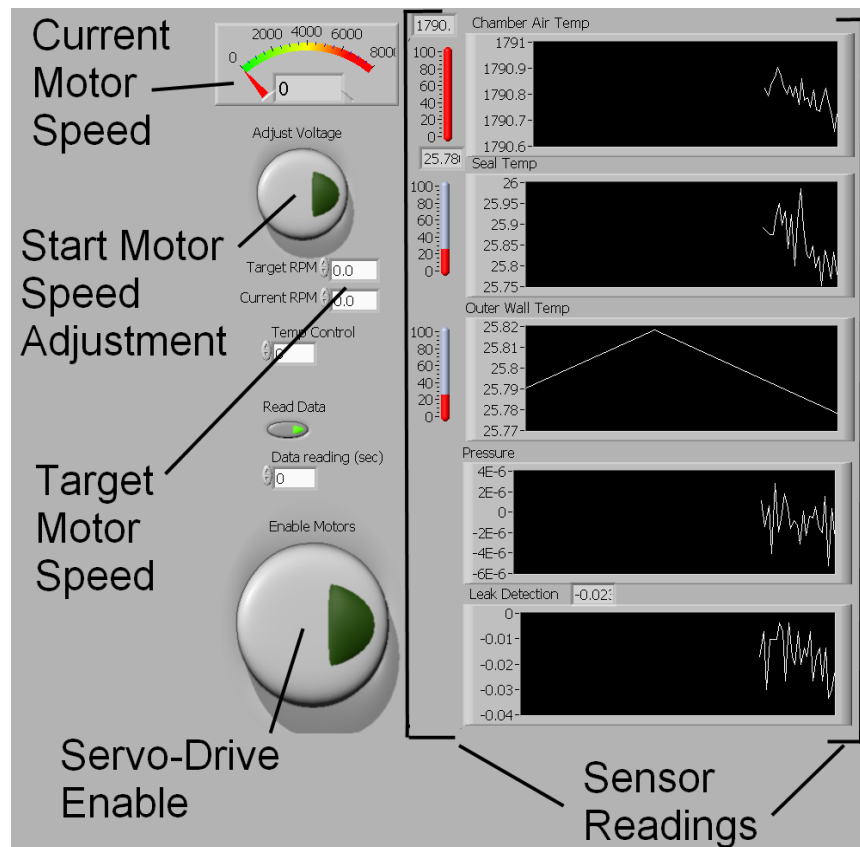


Figure 2.22) LabView™ Control Panel

2.8 Image Capture Set-up and Procedure

A fuel droplet is deposited onto the quartz filament suspended in the central region of the combustion chamber. In order to image the droplet surface area, the droplet is back lit using a bright light source behind the droplet allowing the droplets outline to become visible. The white light was generated using an LED array which was developed in-house. The LEDs used in the array are ultra-bright white light LEDs with a 60° viewing angle. The temporal regression of the projected droplet area is captured using a Nanosence MKIII high speed CCD camera having a resolution of 1280 x 1024 pixels and speed of up to 1000 fps.

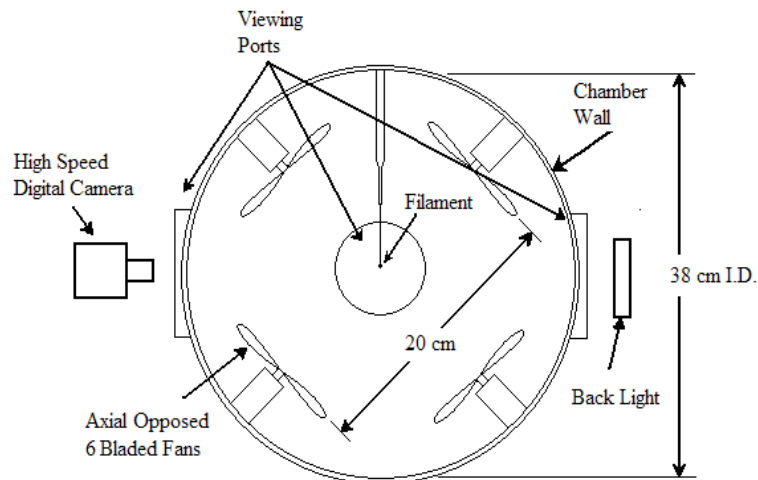


Figure 2.23) Schematic diagram of image capture setup in the high-pressure spherical vessel/chamber

A shutter speed was selected for each experiment and held constant while the image capture rate was adjusted to take advantage of the camera's memory capacity of 815 images. A 3X teleconverter magnifying lens was used in series with a 70-210mm

telephoto lens and a 4X magnifying lens filter to allow for very small viewing areas to be used at a large standoff distance. The resulting lens magnification gives an effective pixel size of 4.9 μm . This allows the camera to view an area of 6.3 mm x 5 mm in the centre of the chamber at a stand-off distance of about 24 cm.

2.9 Image Processing Procedure

The images were processed to determine the droplet size by analyzing the image contrast and defining the droplet border. Once the droplet border is determined, the central area is calculated in pixels and converted into a spherical volume by taking the profile and sweeping it 180° to form a spherical shape. The scale was determined using a known dimension (i.e. the filament thickness) in the same plane as the droplet. An in-house developed Matlab code was used to process each image individually and append the resulting droplet diameter and time stamp to a single file. As a result one file is created for each experimental run. The quartz filament was found to range from 150 to 290 microns at the stem with an approximately 500 micron diameter spherical nodule/sphere at the tip to support the droplet. It was therefore necessary to measure and record the filament thickness of each of the fibres used in the experiments. The measurement was then inserted into the processing code to generate the correct scaling. Detailed information about the calculation of the droplet surface area along with the complete Matlab code used and measurement uncertainties are provided in Appendix B.

Chapter 3: Results and Discussion

3.1 Introduction

Results for turbulence characterization and droplet vaporization are presented in this section. Characterization of the turbulence was performed at standard pressure and temperature conditions as well as at elevated temperatures (up to 80C) and elevated pressures (up to 21atms). Turbulence characterization of the flow inside the chamber was a pre-requisite for studying the droplet vaporization process. Experiments on droplet evaporation were conducted at standard conditions for turbulence levels up to 4.6m/s, and also at elevated pressures up to 21 atm but with a reduced turbulence level (of up to 1.5m/s). Ambient temperature was varied up to 50°C with turbulence levels up to 3.1m/s.

3.2 Turbulence Characterization

3.2.1 Introduction

Characterizing the flow within the chamber was limited by the largest window size of the chamber. There were some technical challenges encountered during LDV characterization of the flow. At high turbulence levels, the seeding particles would not remain in the flow, which necessitated a continuous weak flow of seeding particles. This challenge became even worse at elevated pressure and temperature conditions. To facilitate the addition of seeding particles at elevated pressures, the seeding system was modified. These modifications allowed the seeder to operate at high pressures and thus deliver a small mass of seeding particles that enabled the characterization of turbulence

without influencing the flow dynamics generated by the fans.

3.2.2 Characterization Procedure

Two-component Laser Doppler Velocimetry (TSI 2D-LDV) was used to characterize turbulence within the central region of the chamber/vessel, an area with a diameter of 80 mm. For the majority of the characterization experiments, the airflow was seeded using micro olive-oil droplets. The oil droplets were formed using a modified LaVision fog generator, capable of operating at pressures up to 21 bars. The results from the oil based seeding were also verified using seeding particles generated by burning incense. It was found that the results from the oil based seeding were within 10% of the incense seeding. A minimum of 200,000 LDV data points were taken for each location along x and y axis at 10 mm intervals. The data point were then used to determine the orthogonal mean velocities U and V, and their mean fluctuating components u' and v'. These values were established for a range of turbulence levels at standard conditions as well as elevated temperature and pressure conditions. The characterization results are presented in terms of kinetic turbulent energy (q) which is defined as:

$$q = \frac{u'^2 + v'^2 + w'^2}{2}$$

Since the w' component is not available (only 2D LDV was used), u' is substituted for w'. Experimentation was performed to verify that w' is in fact similar to u' (the LDV system was installed at 90° from the normal orientation). The above equation then becomes;

$$q = \frac{2u'^2 + v'^2}{2}$$

3.2.3 Characterization Results

The results revealed that the mean velocity components were in fact very weak (nearly zero in most cases) as expected, and their values are negligible compared with their corresponding fluctuating mean values. The turbulent field generated in the central region of the vessel appears to be isotropic where the level of anisotropy of turbulence is less than 10% within the 40 mm in radius spherical region of the vessel, as shown in Figure 3.1. The same figure also shows that the isotropy of the turbulent field in this central region of the vessel does not change significantly when the chamber is pressurized from 1 to 21 atm. Figure 3.2 shows the homogeneity level of the turbulent field generated inside the vessel for various fan speeds. Note that in this figure the \sqrt{q} (m/s) profiles were plotted instead of individual mean values of the three fluctuating components (i.e., u' , v' and w'). This was done because the three values are nearly identical, as shown in Figure 3.1, and thus the \sqrt{q} (m/s) would be more suitable as it represents the variation of the averaged value of the three components. This figure shows that turbulence is reasonably homogeneous within a spherical volume of about 40 mm in diameter. Outside of this volume the non-homogeneity level becomes greater than 10%. An examination of this behaviour revealed that this departure of turbulence homogeneity is attributed to the aerodynamics of the fan blades. At present, this issue has not yet been resolved but since the original fans blades produce results that are acceptable within the 40 mm central region these fans were deemed adequate for the experiments conducted for this thesis.

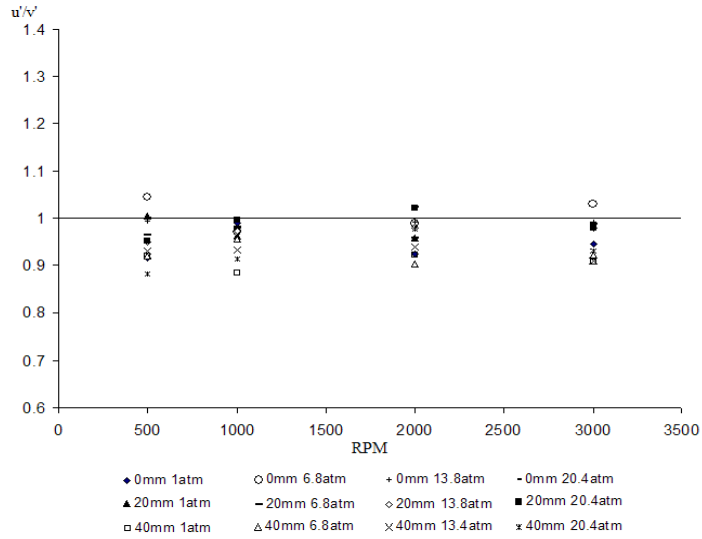


Figure 3.1) Variation of u'/v' for various fan speeds under different ambient conditions

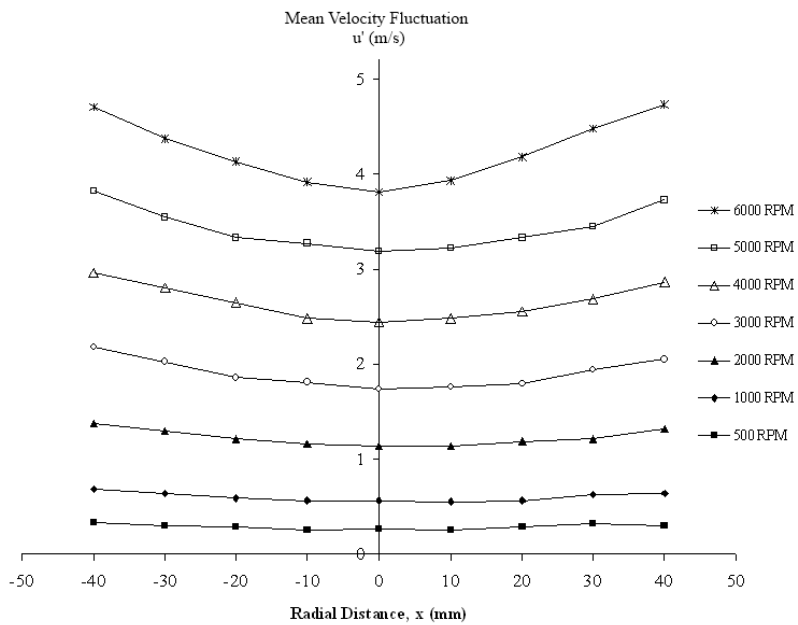


Figure 3.2) Variation of mean velocity fluctuation u' (m/s), in the central spherical region of the vessel at various fan speeds.

As expected the results showed an approximately linear relationship between the speed of the fan and the turbulence intensity (i.e., \sqrt{q} , m/s), as shown in Figure 3.3. This figure reveals that the value of the turbulence intensity is noticeably higher at flow locations farther away from the centre of the vessel (that is closer to the fan location). As mentioned above, the occurrence of higher mean fluctuating turbulence velocity components, which magnifies with an increase in the fan speed, might be caused by the aerodynamics of the fan blades. However, investigation of the data shows that, within the central 40 mm in diameter spherical region shows a single relation would suffice to represent the change of turbulence intensity as a function of the fan speed. Figure 3.4 shows the best fit that correlates turbulence intensity with the fan speed. This best fit line is plotted for zero to six thousand rpm in the centre of the chamber. The correlation (equation) displayed in this figure is used to express the variation in fans' speed in terms of turbulence intensity.

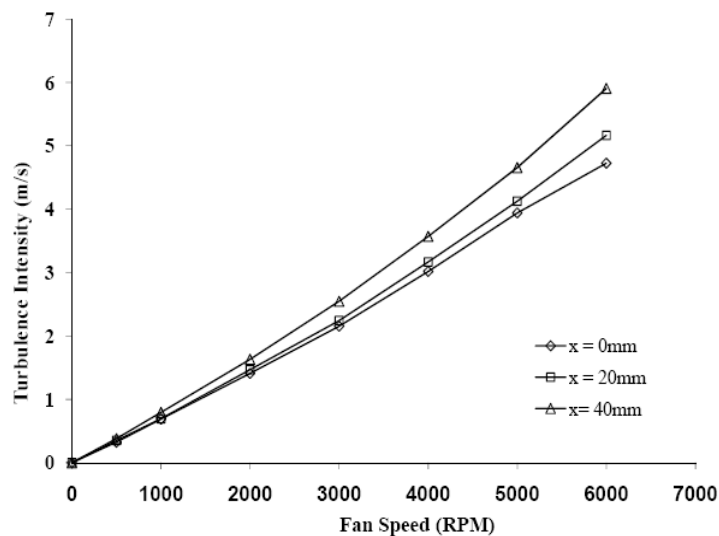


Figure 3.3) Variation of turbulence intensity, (m/s), versus fan speed at varying flow locations in the vessel at atmospheric conditions

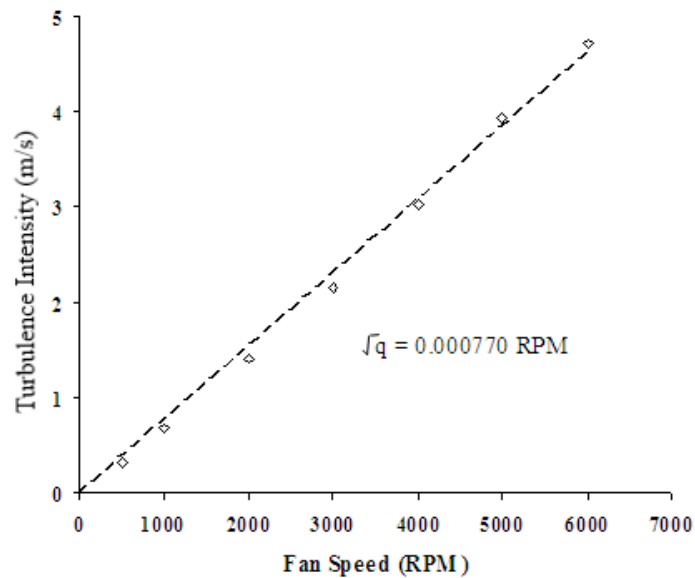


Figure 3.4) Best Fit for Turbulence Kinetic Energy, \sqrt{q} (m/s) vs. fan speed in the centre of the vessel at atmospheric conditions

3.3 Turbulent Droplet Vaporization

3.3.1 Introduction

Over the last fifty years, research has focused on the study of the gasification process of droplets, which resulted in acquiring considerable knowledge that helped better understand spray combustion and hence facilitate the design of more efficient spray combustion systems. However, several related aspects of combustion are still not fully understood. One of these aspects is the role of turbulence on the droplet gasification via either pure vaporization or combustion. This is a controversial subject for many reasons;

for example, it was believed that droplets do not feel the presences of turbulence since the most energetic turbulence eddies are larger than the droplets themselves. This argument was supported by the fact that droplet size range encountered in most practical combustors is much smaller than the size of the most energetic turbulence eddies. In addition, creating laboratory turbulence that is characterized by energetic eddies smaller than droplets size presented a significant challenge. However, research effort devoted to this particular subject, especially in recent decades, has provided evidence that the gasification (via pure evaporation) process of droplets can be greatly affected by ambient turbulence. Indeed, it was experimentally demonstrated that turbulence can play a vital role even if the droplet is much smaller than the size of the most energetic turbulence eddies (e.g., Birouk and co-workers [10,12,22,23,26-29,33,43-45,], and other research groups [9,19,29,46-51]. The present work is a continuation of these previous efforts aimed at clarifying the role of turbulence on the gasification process of fuel droplets. The ultimate objective is to develop new results over as a wide a range as possible of conditions of practical importance.

3.3.2 Experimental Procedure

Droplets are deposited on the quartz fibre through the injector which contains the fluid in a syringe that is held at room temperature outside of the vessel. Because there is no mechanical disconnect (valve) between the fuel inside the injector and the combustion chamber (vessel), the fluid maintains pressure equilibrium with the chamber. The droplet evaporation rates are determined using the equation commonly known as the D^2 -law, which is defined as follows:

$$d_0^2 - d^2 = Kt$$

Where d is the instantaneous diameter, d_0 is the initial diameter (that is d at $t = 0$ sec), t is time and K is the evaporation constant (rate).

For elevated temperature experiments, the combustion chamber was heated to its set temperature, and then the droplet was deposited on the fibre. During the evaporation process, the heating system was shut off in order to limit radiative effects resulting in a near zero heat flux (minor negative flux due to heat losses). The injection system was also retracted during the evaporation capture which left only a very small portion of the injector exposed to elevated temperatures (basically just the injector head) limiting heat transfer from the chamber to the fuel.

For elevated pressure experiments the chamber was pressurized and the temperature was allowed to return to room temperature. Before each experiment, the chamber was evacuated in order to prevent saturation of the atmosphere surrounding the fuel droplet. Although leakage was minimal, the injection of a weak flow of pressurized nitrogen was necessary to maintain the testing at constant pressures for long experiments (which happen especially at low turbulence and high pressures).

3.3.3 Results

3.3.3.1 Standard Pressures and Temperatures

The results presented in this section are concerned only with the vaporization process of n-heptane droplet in a turbulent atmosphere where the ambient pressure and temperature were kept at standard conditions; that is at 1atm and 25°C. From Figure 3.5 it

can be shown that the temporal variation of the droplet normalized squared diameter is linear for all turbulent flow intensities. The same figure shows also that the droplet lifetime shortens as turbulent flow intensity increases. Figure 3.6 presents the variation of the evaporation rate of n-heptane droplet as a function of the fan speed (i.e., turbulence intensity) at standard pressure and temperature conditions. The figure shows that the evaporation rate increases with turbulence intensity; however, this increase is more pronounced at the lower range of turbulence intensity.

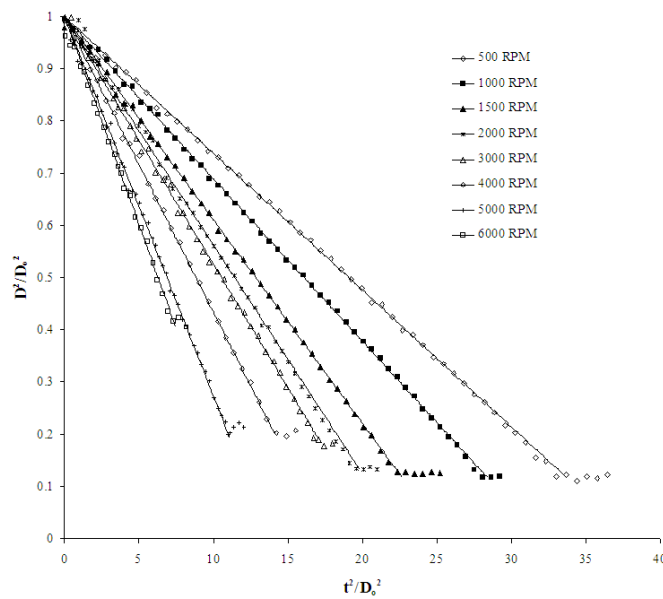


Figure 3.5) Time history for the squared normalized diameter of n-heptane droplet for various turbulence intensities at atmospheric pressure

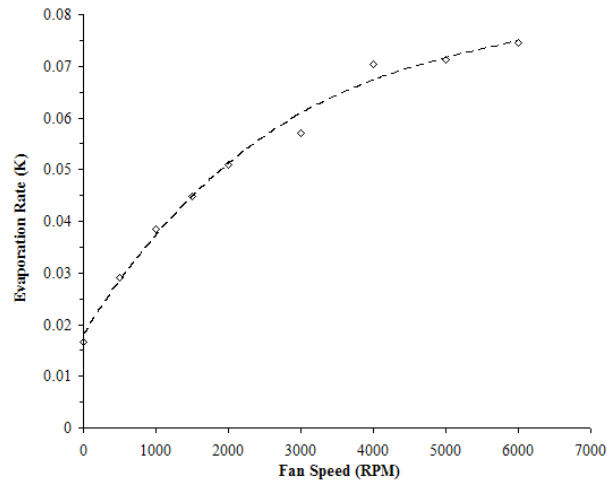


Figure 3.6) Evaporate rate K vs. RPM at atmospheric pressure

3.3.3.2 Elevated Temperatures

Figure 3.7 presents the results for the effect of turbulence on the droplet vaporization process at standard (atmospheric) pressure and an ambient air temperature of 50°C. Note that the slope of the squared droplet diameter represents the rate of droplet evaporation. This figure shows that the droplet vaporization process is enhanced (i.e., reduced droplet lifetime) as the surrounding air turbulence is increased. In addition, Figure 3.7 clearly shows that the droplet lifetime decreased significantly as the droplet surrounding air temperature was increased from room temperature to 50°C. It should be noted that even at elevated temperature a high level of turbulence still influences the droplet vaporization process. By observing the normalized evaporation rate (Figure 3.8) it can be seen that even at 4000 RPM (i.e., $u = 3.08$ m/s) the turbulence is still has an effect on the evaporation rate. However, comparing the normalized evaporation rates at both standard and elevated temperature, it becomes clear that effect of turbulence on evaporation diminishes as the temperature increases.

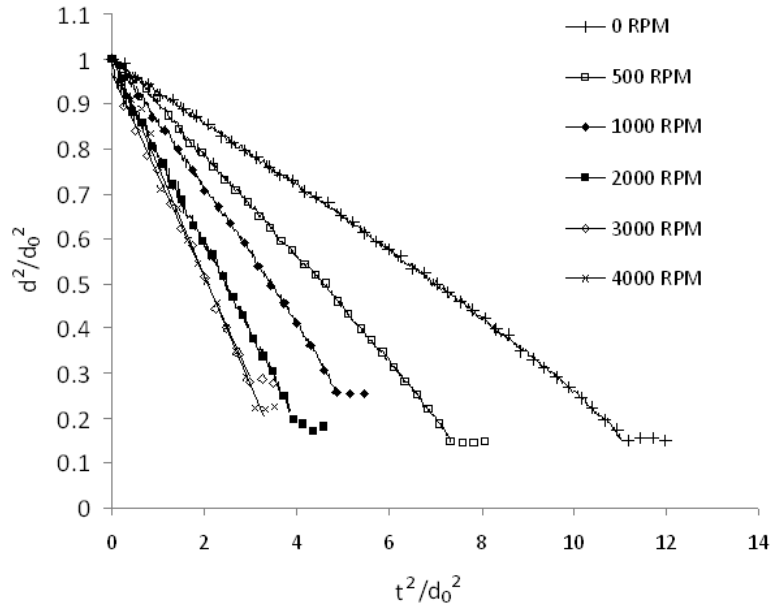


Figure 3.7) *Evaporation of heptane in elevated temperature*

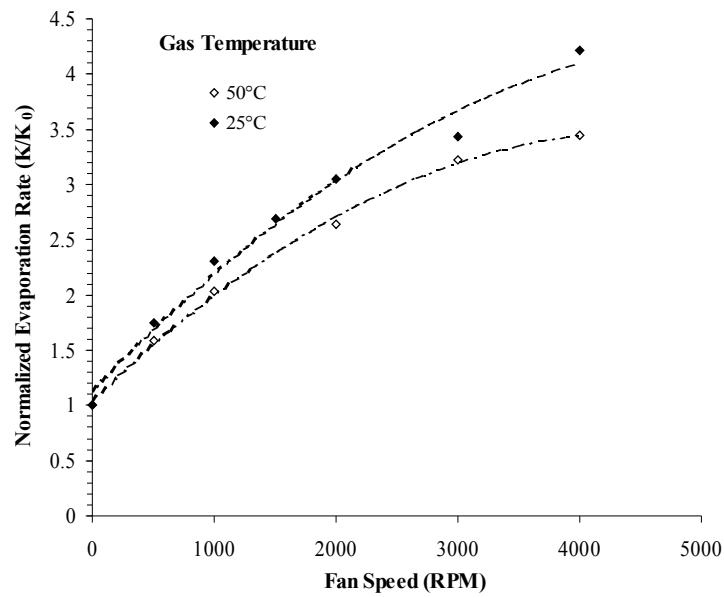


Figure 3.8) *Normalized evaporation rate versus fan speed plotted, at standard and elevated temperatures*

3.3.3.3 Elevated Pressures

The variation of n-heptane droplet averaged evaporation rate as a function of ambient pressure for various flow conditions is presented in Figure 3.9. The figure shows that the droplet evaporation rate decreases as the ambient pressure increases. This trend appears to be identical for quiescent and turbulent flow environments. This figure also shows that the present data in quiescent environment at different ambient pressures agree well with published data (Sato [14]). Moreover, the same figure shows that for a given ambient pressure, the evaporation rate increases with turbulence intensity. This is clearly demonstrated in Figure 3.10 which shows that turbulence enhances the droplet evaporation rate. Figure 3.10 also reveals that the droplet evaporation rate when normalized by its value in quiescent flow conditions increases with pressure for all given turbulent flow intensities.

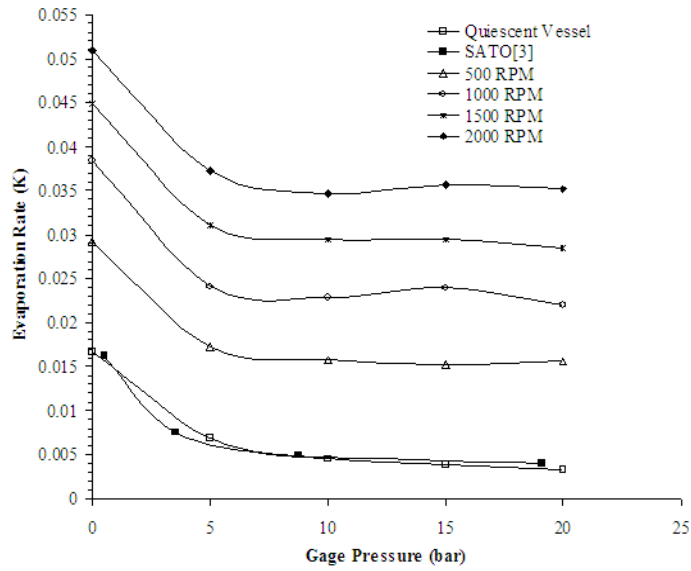


Figure 3.9) Dependency of evaporation rate on ambient pressure and turbulence intensity for *n*-Heptane.

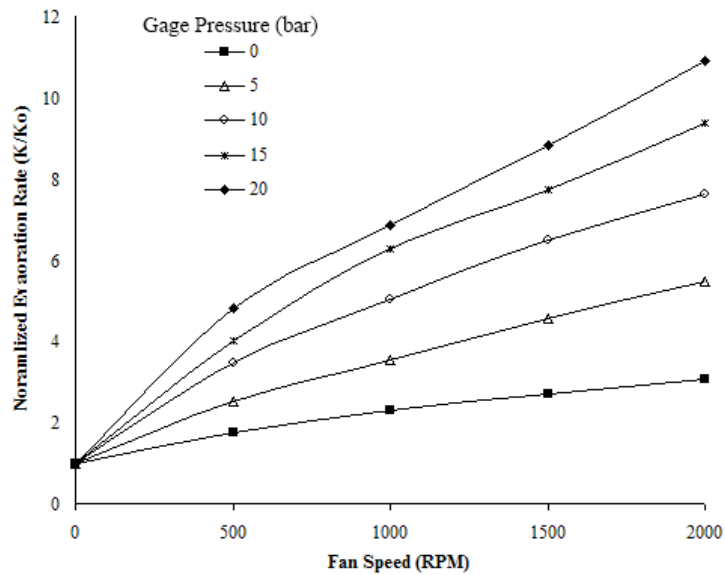


Figure 3.0) Evaporation rates normalized by the zero turbulence value vs. fan speed for various pressures (K_0 is the droplet vaporization rate in quiescent environment; i.e. at zero-RPM).

Chapter 4: Conclusions and Recommendations

4.1 Conclusions

A spherical chamber was developed to generate isotropic and homogeneous turbulence with high turbulence intensity levels. This test facility is also designed to enable testing under elevated pressure and temperature conditions of practical importance to combustion study. Turbulence characterization revealed that a very high level of turbulence (up to around 5 m/s) using axially opposed fans can be produced in the central volume of the chamber. Although the flow homogeneity drops off away from the central region of the chamber, it remains satisfactory within the flow zone of interest to the droplet gasification process. The preliminary results shown in the previous section concerning the droplet vaporization revealed that the effect of turbulence on the droplet lifetime is significant at atmospheric as well as elevated pressure and temperature conditions. Indeed, very high levels of turbulence – in the order of 5 m/s – appear to continue enhancing the droplet vaporization rate at every point tested. In addition, this effect does not seem to weaken as the gas surrounding the droplet increases in temperature. More importantly, the preliminary results revealed that turbulence becomes much more effective in increasing the droplet gasification at elevated ambient pressure.

4.2 Recommendations for Future work

Out of the course of this research, a number of recommendations can be made for either improvements to the test rig or methodology, or for further exploration into the phenomena encountered. They are summarized in this section as follows:

Recommendations for future research:

- Characterization of the flow with the installed heating panels. With the installation of the new heating system the internal dimensions of the chamber have been changed. In order to determine if the loss of space will change the turbulence, the flow will require the re-characterization.
- With the addition of the new camera stand and the arrival of the optics that are necessary for two point LDV, turbulent integral length scale experiments can be now be performed.
- Testing of the new heating system and evaporation droplet testing at elevated temperatures beyond what is in this thesis should be performed. As well the testing of the combined effects of pressure and temperature in the presence of turbulence.
- Testing of the modified ignition should be performed. Followed by droplet combustion experiments at elevated pressures and temperatures.

Recommendations for improvements to the testing apparatus:

- Automation of the injection and ignition systems will be a necessity if high volatility fuels at elevated temperatures and pressures are going to be studied. This is because the reaction times that will be required to perform combustion experiments at high temperatures and turbulence levels are beyond human capabilities. Since most of the systems are already in place to allow for automation it is only a matter of setting up the controls and timing them.
- Automation of data analysis could allow for quasi-real time results. This would

provide a method for determining the validity of the results being taken. This would also eliminate wasting time on collecting results when a fault has occurred in one of the systems.

General Recommendations:

- A systematic approach must be followed when planning experiments. With each new addition of equipment effort should be placed on understanding how the new equipment may impact the existing equipment as well as the future experimental results.
- Each experiment should be planned out in advance and the data from the previous round of experiments analyzed before the next set is performed. When the results are known the next set of planned experiments should be evaluated before proceeding.

References

1. G.A.E. Godsave, Study of the Combustion of Drops in a Fuel Spray – the Burning of Single Drops of Fuel, *Fourth Symposium (International) in Combustion*, (1953) pp 818-830.
2. D.B. Spalding, The Combustion of Liquid Fuels, *Fourth Symposium (International) in Combustion*, (1953) pp 847-864.
3. G.M. Faeth, Current Status of Droplet and Liquid Combustion, *Progress in Energy and Combustion Science*, Vol. 3 Issue 4. (1977) 191-224.
4. G.M. Faeth, Evaporation and Combustion of Sprays, *Progress in Energy and Combustion Science*, Vol. 9 Issue 1-2. (1983) 1-76.
5. G.M. Faeth, Spray Combustion Phenomena, Twenty-Sixth International Symposium on Combustion, the Combustion Institute, (1996) 1593-1612.
6. C.K. Law, Recent Advances in Droplet Vaporization and Combustion, *Progress of Energy and Combustion Science*, Vol. 8 No. 3 (1982) 360-1285.
7. W.A. Sirignano, Fuel Droplet Vaporization and Spray Combustion Theory, *Progress of Energy and Combustion Science*, Vol. 9 No. 4 (1983) 291-322.
8. A. Williams, Combustion of Droplets of Liquid Fuels: A Review, *Combustion and Flame*, Vol. 21 Issue 1 (1973) 1-31.
9. Y. Ohta, K. Shimiyama, S. Ohigashi, Vaporization and Combustion of Single Liquid Fuel Droplets in a Turbulent Environment, *JSME*, Vol. 18 No. 115, (1975) 47-56.
10. M. Birouk, and I. Gökalp, A new correlation for turbulent mass transfer from liquid droplets, *International Journal of Heat and Mass Transfer* 45 (2000) 37-45.
11. B. Abramzon, W.A. Sirignano, Droplet evaporation model for spray combustion calculations, *International Journal of Heat and Mass Transfer*, Vol. 32 No. 9 (1989) 1605-1618.
12. M. Birouk, C. Chauveau, B. Sarh, A. Quilgars, I. Gökalp, Turbulence effects on the vaporization of mono-component single droplets, *Combust. Sci. Technol.* 113-114 (1996) 413-428.
13. V. Yang, N.N. Lin, J. S. Sheun, Vaporization of Liquid Oxygen (LOX) Droplets in Supercritical Hydrogen Environments, *Combustion Science Technologies*, Vol. 97 (1994) 247-270.
14. Sato, J. Studies on droplet evaporation and combustion in high pressures, 31st Aerospace Sciences Meeting and Exhibit, Reno Nevada, (1993). AIAA Paper 93-0813.
15. A.J. Marchese, F.L. Dryer, V.Nayagam, Numerical Modelling of Isolated N-Alkane Droplet Flames: Initial Comparison with Ground and Space Based

- Microgravity Experiments, Combustion and Flame, Vol. 116 (1999) 432-459.
16. V. Yang, Modeling of supercritical vaporization, mixing, and combustion processes in liquid-filled propulsion systems, Proceeding of the Combustion Institute, Vol. 28 (2000) 925-942.
 17. S.S. Sazhin, I.N. Shishkova, A.P. Kryukov, V.Y. Levashov, M.R. Heikal, Evaporation of droplets into a background gas: Kinetic modelling, International Journal of Heat and Mass Transfer, Vol. 50 (2007), 2675-2691.
 18. M. Masoudi, W. A. Sirignano, Collision of a vortex with a vaporizing droplet, International Journal of Multiphase Flow 26 (2000) 1925-1949.
 19. J-S. Wu, Y-J. Lin, H-J. Sheen, Effects of Ambient Turbulence and Fuel Properties on the Evaporation Rate of single Droplets, Int. J. Heat Mass Transfer 44 (2001) 4593-4603.
 20. M. Jangi, H. Kobayashi, Heat and mass transfer of a fuel droplet evaporating in oscillatory flow, International Journal of Heat and Fluid flow, Vol. 30 (2009), 729-740.
 21. K.L. Pan, J.W. Li, C.P. Chen, C.H. Wang, On droplet combustion of biodeisel fuel mixed with diesel/alkanes in microgravity condition, Combustion and Flame, Vol. 156 (2009) 1926-1936.
 22. Abou Al-Sood, M. M. and Birouk, M., Numerical simulation of the effects of droplet initial conditions on the vaporization process. Computational Thermal Sciences, 1(2009) 159-187.
 23. C. Chauveau, M. Birouk, I. Gökalp, An analysis of the d₂-law departure during droplet evaporation in microgravity, International Journal of Multiphase flow, (2010)
 24. G.S Jackson, C.T. Avedisian, The Effect of Initial Diameter in Spherically Symmetric Droplet Combustion of Sooting Fuels, Mathematical and Physical Sciences, Vol. 446, No. 1927 (1994) pp. 255-276.
 25. M.T. Monaghan, R.G. Siddall, M.W. Thring, The influence of initial diameter on the combustion of single drops of liquid fuels. Combustion and Flame, Vol. 12, (1968) 45-53.
 26. Abou Al-Sood, M. M. and Birouk, M., Droplet heat and mass transfer in turbulent airstream. International Journal of Heat and Mass Transfer, 51 (2008) 1313-1324.
 27. Abou Al-Sood, M. M. and Birouk, M., A numerical model for calculating the vaporization rate of a fuel droplet exposed to a convective turbulent flow, International Journal of Numerical Methods for Heat and Fluid Flow 18 (2008) 146-159.
 28. Abou Al-Sood, M. M. and Birouk, M., A numerical study of the effect on turbulence mass transfer from a single fuel droplet evaporating in a hot convective turbulent flow. International Journal of Thermal Sciences 46 (2007) 779-789.
 29. C. Morin et al., Vaporization and Oxidation of Liquid Fuel Droplets at High

Temperature and High Pressure: Application to N-Alkanes and Vegetable Oil Methyl Esters, *Combustion. Sci. and Tech.* 176 (2004) 499-529.

30. G.K. Batchelor, A.A. Townsend, Decay of isotropic turbulence in the initial period, *Proceeding of the Royal Society A Mathematical, Physical and Engineering Sciences*, (1948) 193-539
31. G. Comte-Bellot, S. Corrsin, Simple Eulerian time correlation of full and narrow-band velocity signals in grid generation, *Journal of fluid mechanics*, Vol. 391 (1971) 359-372.
32. L. Mydlarski, Z. Warhaft, On the onset of high-Reynolds number grid generated wind tunnel turbulence. *Journal of fluid Mechanics*, Vol. 320 (1996) 331-368.
33. M. Birouk, B. Sarh, I. Gökalp, An attempt to realize experimental isotropic turbulence at low Reynolds number, *Flow, Turbulence and Combustion*, Vol. 70 (2003) 325-348.
34. E.S. Semenov, Measurements of turbulence characteristics in a closed vessel with artificial turbulence, *combustion, Explosion and Shockwaves* 1 (1965) 57-62.
35. T.D. Fansler, D. Todd, Turbulence Characteristics of a Fan-Stirred Combustion Vessel, *Combustion and Flame*, 80 (1990) 350-354.
36. H. Meng, G. Pan, Y. Pu, S.H. Woodward, Holographic particle image velocity: from film to digital recording, *Measurement Science and technology*, Vol. 15 (2004) 673-685.
37. T. Fallon, C.B. Rogers, Turbulence-induced preferential concentration of solid particles in microgravity conditions, *Experiments in Fluids*, Vol. 33 (2002) 233-241.
38. J. de Jong, L. Cao, S.H. Woodward, J.P.L.C. Salazar, L.R. Collins, H. Meng. Dissipation rate estimation from PIV in zero-mean isotropic turbulence, *Experimental Fluids*, Vol. 46 (2009) 499-515
39. M. Birouk, I. Gökalp, Current status of droplet evaporation in turbulent flows, *Progress in Energy and Combustion Science* 32(2006) 408-423.
40. A. Grierson, T. Grodecki, Design/development of a fan using propeller theory, *University of Manitoba Undergraduate Thesis* (2008)
41. C.K. Law, C.H. Lee and N. Srinivasan, Combustion Characteristics of Water-in-oil Emulsion Droplets, *Combustion and Flame*, 37 (1980) 125-143.
42. K. Miyasaka, C.K. Law, Combustion of Strongly interacting linear droplet arrays, *Eighteenth International Symposium on Combustion*, the Combustion Institute, Pittsburgh, Pa, (1981) 283-292.
43. M. M. Abou Al-Sood, M. Birouk, A numerical model for calculating the vaporization rate of a fuel droplet exposed to a convective turbulent airflow, *Int. J. Num. Meth. Heat Fluid Flow* 18 (2008) 146-159.
44. Birouk, M. and Abou Al-Sood, M. M., Droplet evaporation in a turbulent high-pressure free stream – A numerical study. *International Journal of Thermal*

Sciences, 49 (2010) 264-271.

45. Birouk, M., Abou Al-Sood, M. M. and Gökalp, I., Droplet evaporation in a turbulent environment at elevated pressure and temperature conditions. *Combustion Science and Technology*, 180(2008) 1987-2014.
46. I. Gökalp, C. Chauveau, C. Morin, B. Vieille, M. Birouk, Improving droplet breakup and vaporization models by including high pressure and turbulence effects, *Atomization and Sprays*, Vol. 10 (2000) 475-510.
47. I. Gökalp, C. Chauveau, O. Simon, X. Chesneau, Mass transfer from liquid fuel droplets in turbulent flow, *Combustion Flame* 89 (1992) 286-298.
48. J-S. Wu, K-H. Hsu, P-M. Kuo, H-J. Sheen, Evaporation model of a single hydrocarbon fuel droplet due to ambient turbulence at intermediate Reynolds numbers, *Int. J. Heat Mass Transfer* 46 (2003) 4741-4745.
49. J-K Park, Droplet Vaporization in Turbulent Flow, Ph.D. thesis, University of Wisconsin-Madison, USA, 1987.
50. J.M. Tishkoff, Interaction between droplets and gas-phase turbulent flows, Third joint ASCE/ACME Mechanics conference (1989) 1-6.
51. S.C. Fabbro, M. Birouk, Experimental Study of n-Heptane Droplet Evaporation in a Turbulent Hot Atmosphere, *CICS2010*, pp. 76-80.
52. S. Okajima, S. Kumagai, Further Investigation of Combustion of Free Droplets in Free Falling chamber Including moving droplets, *Fifteenth International Symposium on Combustion*, the Combustion Institute, Pittsburgh, Pa, (1975) 401-417.
53. S. Kumagai, H. Isoda, Combustion of Fuel Droplets in a Falling Chamber, *Sixth International Symposium on Combustion*, the Combustion Institute, Reinhold, N.Y., (1957) 726-731.
54. N. Hiromitsu, Influence of Flow Turbulence on the Evaporation Rate of a Suspended Droplet in a Hot Air Flow, *Heat Transfer: Japanese Research*, Vol. 24 No. 8 (1995) 689-700.
55. J.S. Shuen, V. Yang, C.C. Hsiao, Combustion of Liquid Droplets in Super-critical Conditions, *Combustion and Flame*, Vol. 89 No. 3-4 (1992) 299-319.
56. P. R. Yearling, Experimental determination of convective heat and mass transfer rates from single evaporating droplets in a turbulent air flow, Ph.D. thesis, North Carolina State University, USA, 1995.
57. Sidhu, M.S., and A.A. Burluka, Average vaporization rate in turbulent sub-critical two-phase flow, *Combust. Scie. Technol.* 180 (2008) 975-996.
58. W. Hwang, J.K. Eaton, Creating homogenous and isotropic turbulence without a mean flow, *Experiments in Fluids*, Vol. 36 (2004) 444-454.
59. C. Goepfert, J.L. Marié, D. Chareyron, M. Lance, Characterization of a system generating homogenous isotropic turbulence field by free synthetic jets, *Experimental Fluids*, Vol. 48 (2010) 809-822.

60. J Thompson. Design a fan blade assembly for a high pressure vessel, University of Manitoba Undergraduate Thesis (2003)
61. D. Surminski. Testing and evaluation of a fan blade assembly, University of Manitoba Undergraduate Thesis (2004)
62. DynaDrive 1224-BLS servo-drive user guide, Servo Dynamics, Ver. 1.01, October 28, 2004

Appendices

Appendix A – Seal Manufacturing Procedure

Seal Manufacturing Procedure

A range of materials can be used to produce the seals, however it is recommended that poly-amide filled Teflon be used due to its high service temperature and low coefficient of friction. The cutter is manufactured by wire Electrical Discharge Machining (EDM) using the two programs loaded on the wire EDM machine located in the mechanical engineering material laboratory at the University of Manitoba.

Lip cutting program - Tsealv1.26

Outer o-ring groove cutting program - Tsealv1.20s.

Method for cutting the seals using the designed cutting tool.

Step 1.) Turn the rod down to the required outer diameter – 1.125 inches

Step 2.) Centre drill the rod using a 0.375 inch drill bit.

Step 3.) Feed the inner lip cutting tool into the 0.375 inch hole and spin at lowest spindle speed available or by hand.

Step 4.) Traverse the tool outwards till the I.D. of the forward facing section is 0.625 inch.

Step 5.) Move the tool to the centre of the hole so the cutting figures are free of the machined lips and back the tool out.

Step 6.) Remove the inner lip cutting tool from the lathe and install the o-ring groove cutting tool.

Step 7.) Line up the edge of the cutting tool to the forward edge that was formed from the lip cutting tool.

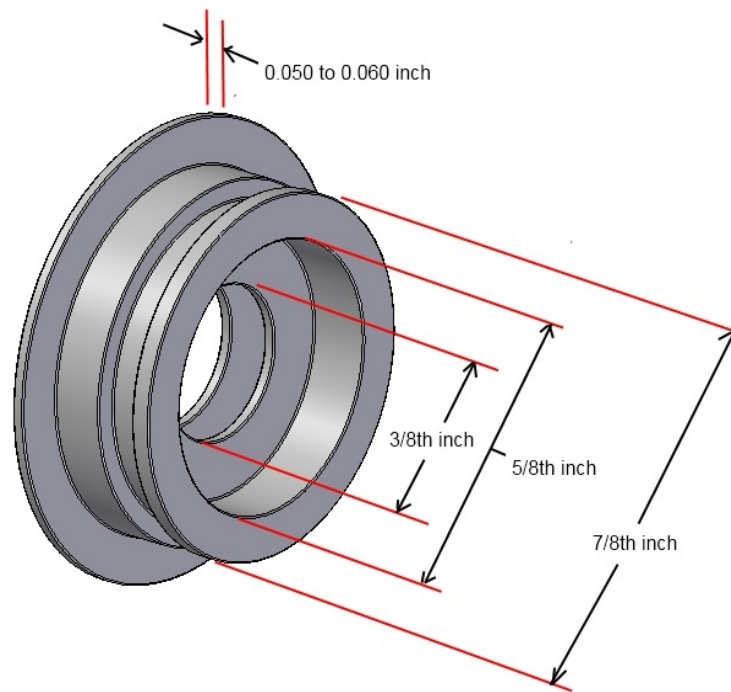
Step 8.) Machine the O.D. of the seal by traversing the tool inwards till the O.D. is 0.875 inch.

Step 9.) Back off the o-ring cutting tool from the material.

Step 10.) Part the seal from the rod leaving about 0.100 inch of the large O.D. intact.

Step 11.) Take the end that has been parted and feed it carefully into the jaws of the lathe grabbing it firmly without deforming it.

Step 12.) Machine the lip down leaving a outer flange of 0.050 – 0.060 inches. Be careful not to damage the inner lip when taking the edge down.



Appendix B - Matlab Code and Error Calculations

Matlab Image Processing Code

```
clear all
close all
%subplot(221)

%%%%%%%%%%

TubeDiameter = 250;
firstpic = 0;
picstep = 1;
lastpic = 815;
mst = 'ImgA000000';

%%%%%%%%%%

for fco = 1 : 6
    cd(int2str(fco));
    hf = fopen('test.dat','wt');
    mmco = 0;
    for mco = firstpic: picstep: lastpic
        mmco = mmco + 1;
        fprintf('mco = %d\tfco = %d\n',mco,fco);
        % SPECIFY FILE NAME NEXT

        %%%%%%%%%%%

        sno=num2str(mco);
        strng=[mst,sno];
        strng(5:(length(strng)-10+5-1))='';
        strng=[strng,'.tif'];

        %%%%%%%%%%%

        if (exist(strng,'file')==0)
            continue;
        end
        ima = imread(strng); % Load image
        ima = ima';
        %sz = size(ima);
        %for i = 1 : sz(1)
        %   ima3(i,:) = ima(sz(1)+1-i,:);
        %end
```

```

%ima = ima3;
clear ima3 ima2 level1 L Lm pos tama maxi BW2 salir s1 s2 renglon;

%%%%%%%%%%%%%%%%%%%%%%%%%%%%%%%%%%%%%%%%%%%%%%%%%%%%%%%%%%%%%%%%%%%%%%%%

%ima = 255-double(ima);
ima2 = ima<120; % 128 You may need to play with this threshold
ima = uint8(ima);
%%% level = graythresh(ima);
%%% ima2 = im2bw(ima,level);
%%%figure
L = bwlabel(ima2);
Lm = max(max(L));
for i = 1:Lm
    pos=find(L==i);
    tama(i)= length(pos);
end
maxi = find(tama==max(tama));
BW2=zeros(size(ima2));
pos=find(L==maxi);
BW2(pos)=1;
%BW2 = edge((BW2),'canny');
%%%imagesc(BW2)

[s1 s2] = size(BW2);
% There are rows at the bottom with zeroes, find how many
salir = 0;
while salir == 0;
    renglon = BW2(s1,:);
    if sum(renglon) ~= 0;
        salir = 1;
    end
    s1 = s1-1;
end

%%%%%%%%%%%%%%%%%%%%%%%%%%%%%%%%%%%%%%%%%%%%%%%%%%%%%%%%%%%%%%%%%%%%%%%%
%%% Finding the diameter of tube

if (mco==firstpic)
    TubePixelPrecision = 5;
    for tpco = 1 : TubePixelPrecision
        renglonTPP = BW2(s1-tpco-1,:);
        posTPP = (find(renglonTPP == 1));
        TubePixelTPP(tpco) = posTPP(end) - posTPP(1);
    end
    TubePixel = mean(TubePixelTPP);

```

```

end
%TubePixel = 39; %Because of bad zooming, 219=33.2

%%%%%%%%%%%%%%%%%%%%%%%%%%%%%%%%%%%%%%%%%%%%%%%%%%%%%%%%%%%%%%%%%%%%%%%%

contador = 0;
salir = 0;
counter = 0;
while salir == 0;
    renglon = BW2(s1,:);
    pos = (find(renglon == 1));
    BW2(s1,pos(1):pos(end))=1;
    dista2 = pos(end)-pos(1);

    %%%%%%%%%%%%%%%%%%%%%%%%%%%%%%%%%%%%%%%%%%%%%%%%%%%%%%%%%%%%%%%%%%%%%%%%%

    Cnst = 1.2;
    T = TubePixel*Cnt; %Threshold Width of Filament

    %%%%%%%%%%%%%%%%%%%%%%%%%%%%%%%%%%%%%%%%%%%%%%%%%%%%%%%%%%%%%%%%%%%%%%%%%
    if dista2<T;
        contador = contador+1;
        counter = 0;
    end
    if dista2 > T; %Threshold
        counter = counter + 1;
        if counter > 4;
            salir = 1;
            s1 = s1 + 5;
        end
    end
    s1 = s1-1;
end

% Fill the holes in the drop
s2 = s1;
salir = 0;
while salir == 0;
    renglon = BW2(s2,:);
    pos = (find(renglon == 1));
    if isempty(pos)
        salir = 1;
    else
        BW2(s2,pos(1):pos(end))=1;
        s2 = s2-1;
    end
end

```

```

end

%BW2(1:s1+1,:)=0;
BW2(s1:end,:)=0;
%%%imagesc(ima)
are = sum(sum(BW2));
BW2 = edge(uint8(BW2),'canny');

%%%[pos3 pos4] = find(BW2==1);
%%%for i=1:length(pos3)
%%% text(pos4(i),pos3(i),'\bullet','Color','green','fontSize',6)
%%%end

Area = are*(TubeDiameter/TubePixel)^2*(1e-6); %MM^2
%%%colormap gray(256)
%%%title(['Area in pixel numbers = ',num2str(are)])

%%%%%%%%%%%%%%%%%%%%%%%%%%%%%%%%%%%%%%%%
fprintf(hf,'%d\t%d\n',mco,Area);
%%%%%%%%%%%%%%%%%%%%%%%%%%%%%%%%%%%%%%%%
end
%%%%%%%%%%%%%%%%%%%%%%%%%%%%%%%%%%%%%%%%
fclose(hf);
%%%%%%%%%%%%%%%%%%%%%%%%%%%%%%%%%%%%%%%%
cd ..
end

```

Measurement Uncertainty in Calculated Droplet Size and Evaporation Rate

Part A - Measurement Uncertainty in Calculated Droplet Size

The measurement uncertainty associated with droplet size calculations is determined by the magnification and the imaging resolution error. The magnification that is obtained in the experiments through the use of the magnifying lenses and the telephoto lens provides an image that is approximately 6.3 mm by 5.0 mm. Since the pixels on the camera are square and have a resolution of 1280 by 1024 the size of the pixel is calculated at 4.92 μm in both the horizontal and vertical directions. This gives a spacial resolution of 41311 pixels/ mm^2 . The Matlab code that is used in determining the droplet edge has an associated maximum error in detecting the edge of the droplet estimated at 2 pixels. Since the edge detection error is constant the largest percentage error would be when the droplet is at its smallest. Since the droplet at its smallest when it is nearly completely evaporated the estimated minimum droplet size is approximately the size of the nodal on the end of the fibre. For the error calculation the size is estimated at 600 μm , this is because even though the nodal is approximately 500 μm , the very end of the droplet evaporation is not included when determining the evaporation rate. The error is then calculated as;

600 μm +/- 4 pixels (2 pixels on either side)

600 μm / 4.92 $\mu\text{m}/\text{pixel}$ gives approximately 122 pixels +/- 4 pixels

The area of the droplet in pixels is calculated as;

Area in pixels = $\pi \cdot \text{radius}^2 = \pi \cdot (122/2)^2 = 11690$ pixels

The error in estimating the droplet size then calculated as;

Area associated with the largest error - the area in pixels which is,

$$\pi \cdot (126/2)^2 - \pi \cdot (122/2)^2 = 12469 - 11690 \text{ pixels} = 779 \text{ pixels}$$

The maximum percentage error in estimating the smallest droplet size is therefore;

779 pixels/11690 pixels or 6.7%

Part B - Measurement Uncertainty in Calculated Evaporation Rate

The measurement uncertainty associated with evaporation rate calculations is determined by using the error in the calculated droplet size at the beginning of the droplet evaporation as well as the end. The percent error at the end of the droplet life has already been calculated in the previous sections. The estimated size of the droplet at the beginning of evaporation is approximately 1.5mm. Using the method given in the preceding section, this gives the droplet size of 73003 pixels. The error associated with a droplet of this size is 1503 pixels or 2%. The error in the evaporation rate is then calculated using the 2% at the beginning of the droplet and 6.7%, this is represented graphically below.

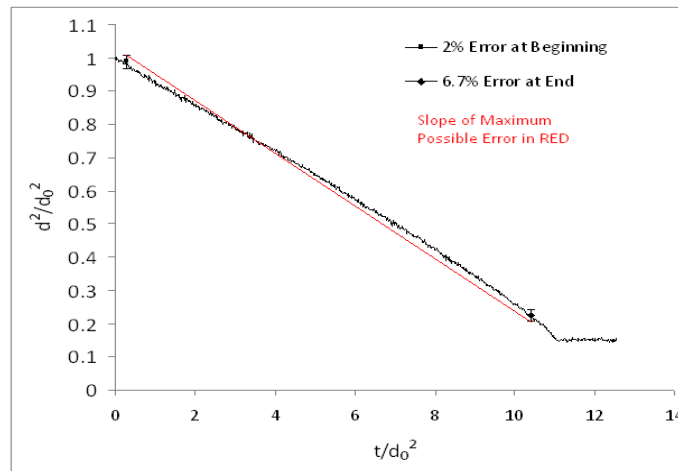


Figure D1.) The maximum error in evaporation rate.

The slope of the evaporation rate for the example in Figure D1 can be calculated as;

$$\frac{y_2 - y_1}{x_2 - x_1} = \frac{.99 - .225}{.260 - 10.4} = 0.075 \text{ mm}^2/\text{s}$$

The error in droplet diameter is calculated given the droplet size times the percent error.

Using the initial and final droplet diameters the error in the evaporation rate can be calculated as;

$$\frac{\text{Error in } y_2 + \text{Error in } y_1}{x_2 - x_1} = \frac{.0198 + .0045}{.260 - 10.4} = 0.0024 \text{ mm}^2/\text{s}$$

This gives a evaporation rate percent error of;

$$\frac{0.0024 \text{ mm}^2/\text{s}}{0.075 \text{ mm}^2/\text{s}} = 0.032 \text{ or } 3.2\%$$

Since the normalized initial droplet size is unity, the final droplet size which was estimated to be 600 μm is constant and the percent error at the beginning and end of the droplet life is constant, the maximum percent error for all of the evaporation rates can be calculated as follows;

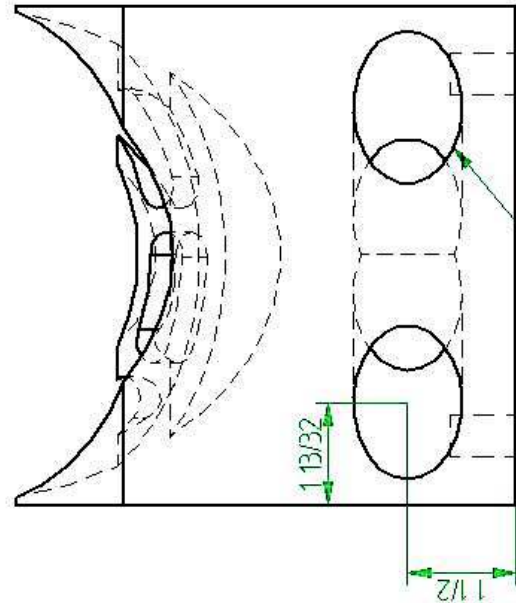
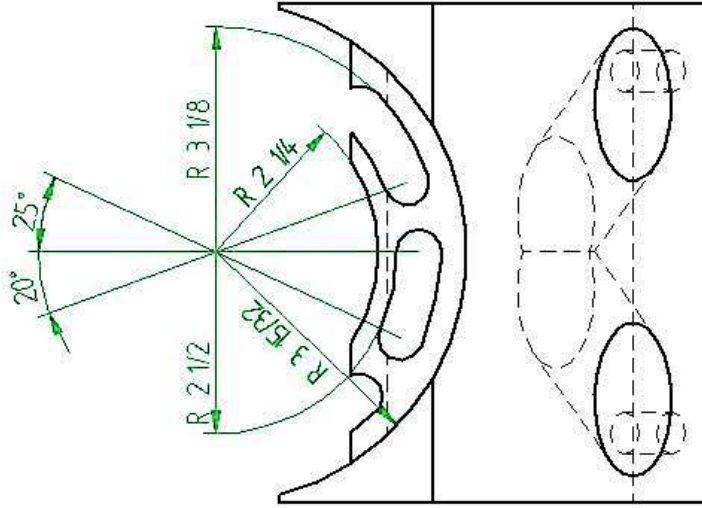
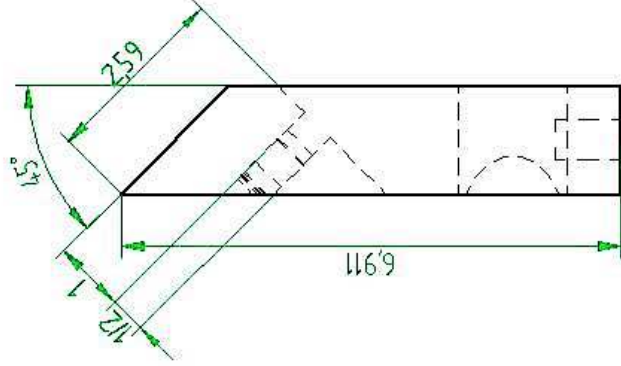
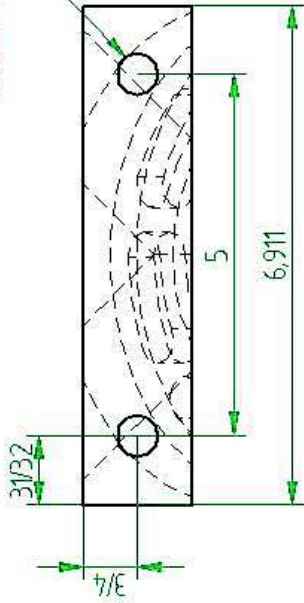
$$\frac{\text{Error in } y_2 + \text{Error in } y_1}{y_2 - y_1} = \frac{.02 + .0045}{1 - 0.225} = 0.00316 \text{ or } 3.16\%$$

Appendix C – Drawings

Chamber Stand Parts

Date: July 10, 2006 Version: 1.1

5/8 UNF threaded hole 1 in. Depth

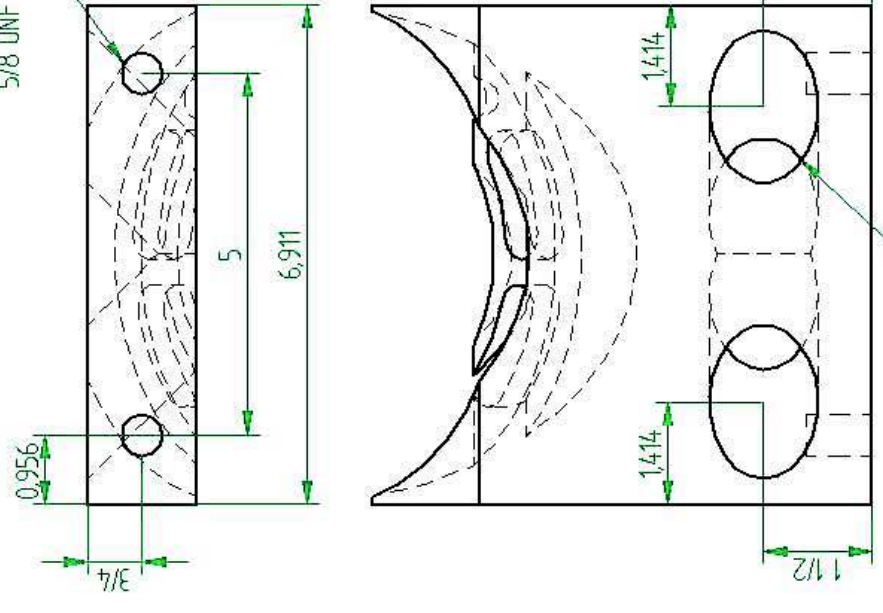
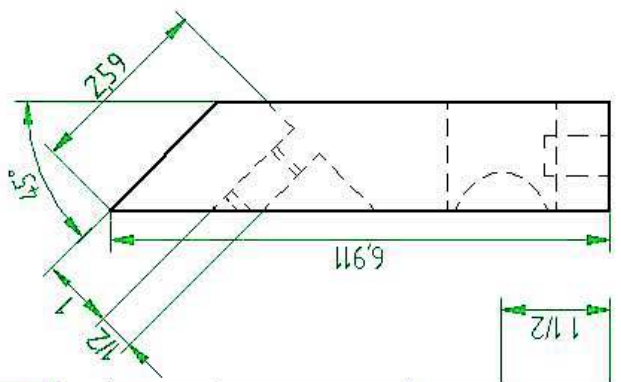
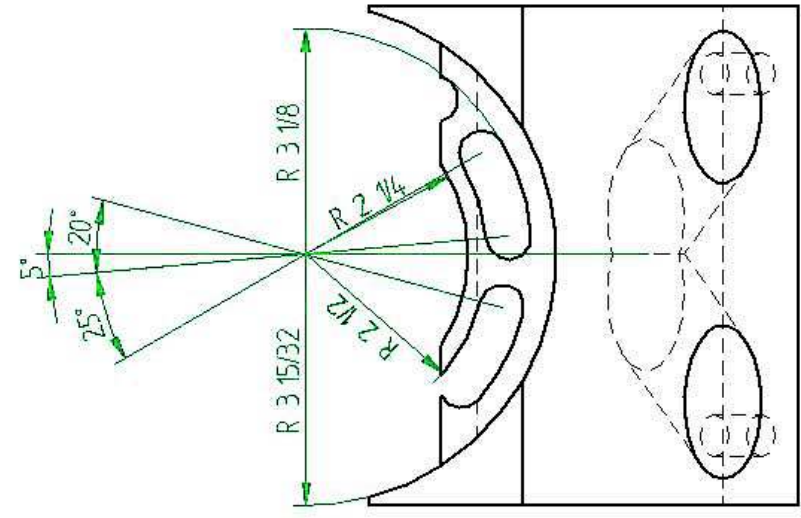


1 1/2 in. Hole cut at 45 degrees

SOLID EDGE NEXT RELEASE	
Title:	Bracket3_13
Material:	Steel
Author:	Sean Fabbro

Date: July 10, 2006 | Version: 1.1

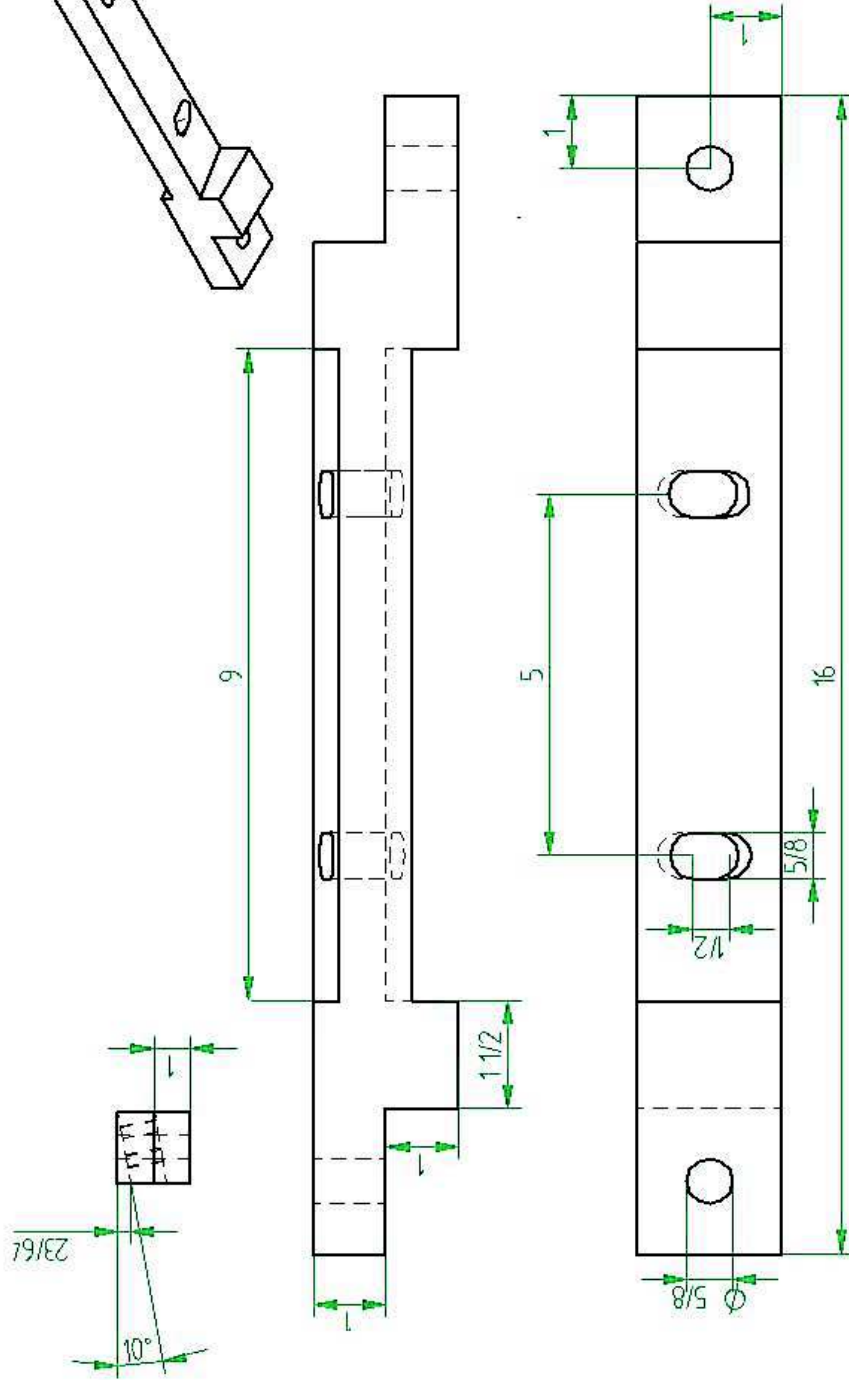
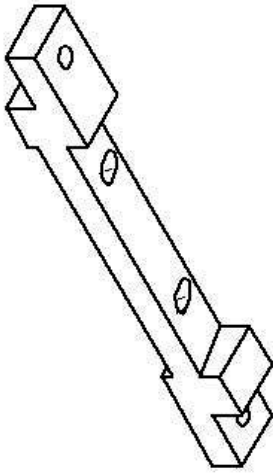
5/8 UNF threaded hole 1 in. Depth



1 1/2 in. Hole cut at 45 degrees

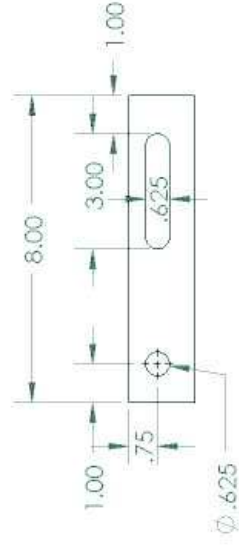
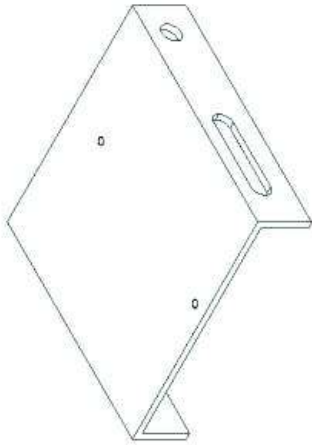
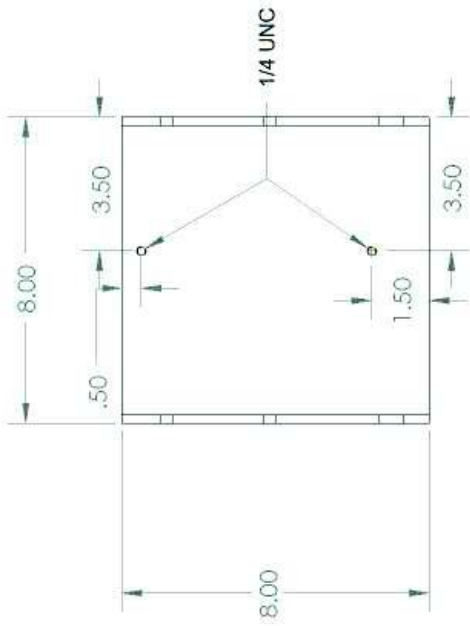
SOLID EDGE NEXT AUTOCAD	
Title:	Bracket3_24
Material:	Steel
Author:	Sean Fabbro

Date: Oct. 6, 2006 Version: 1.1



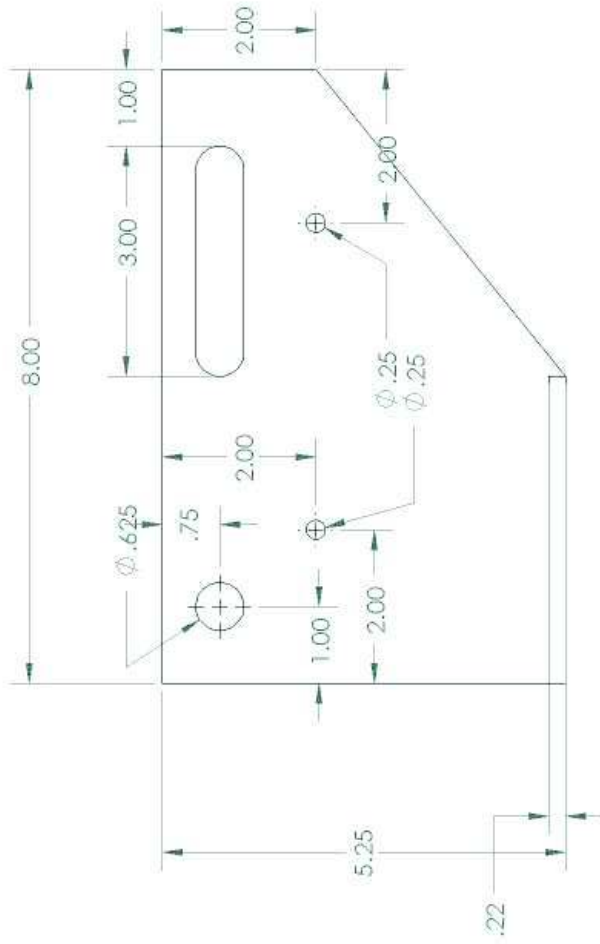
SOLID EDGE PART NUMBER	
Title:	Stand Adapter
Material:	Steel
Author:	Sean Fabbro

Camera Stand Parts



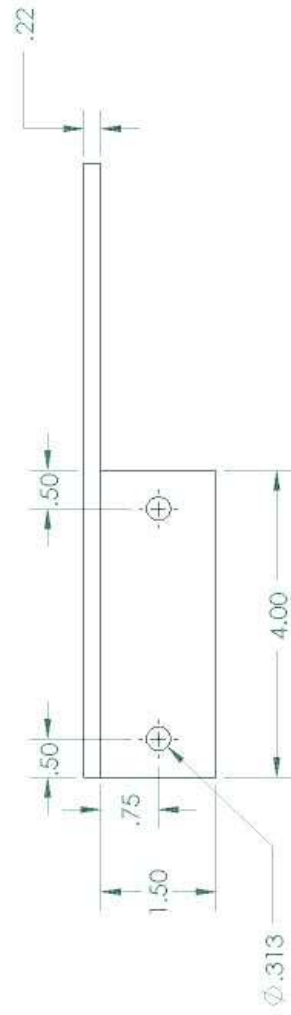
Material - Steel
Quantity - 1

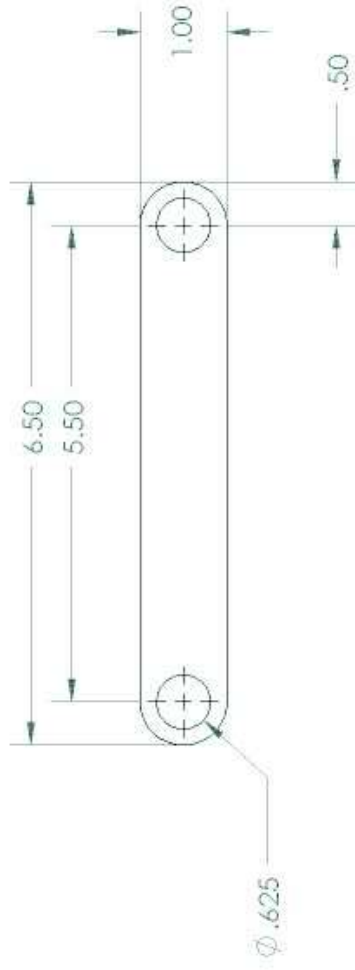
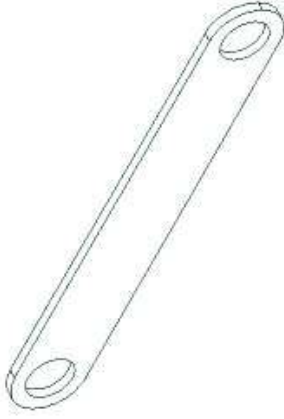
** made from 8x11.5 C channel



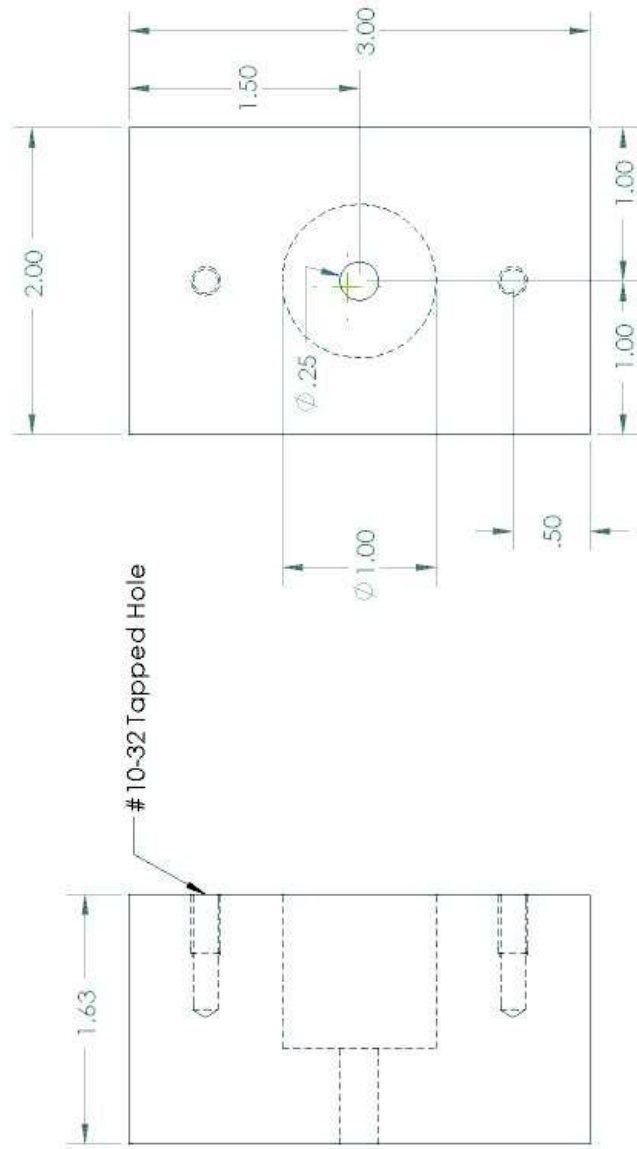
Material - Steel
Quantity - 1

** Make from 8x11.5 C-Channel

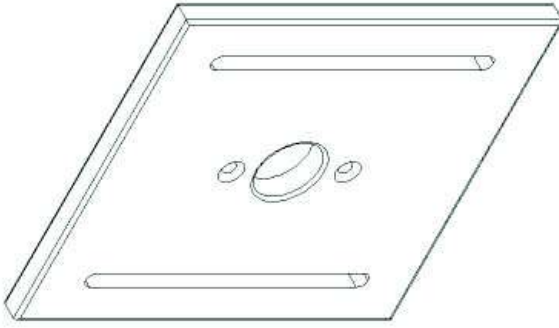




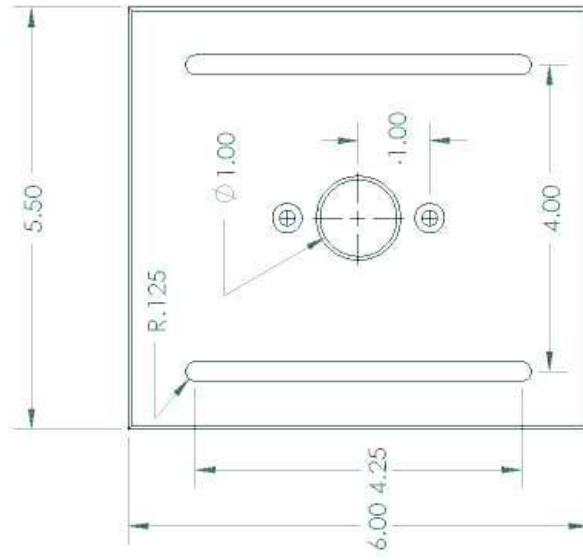
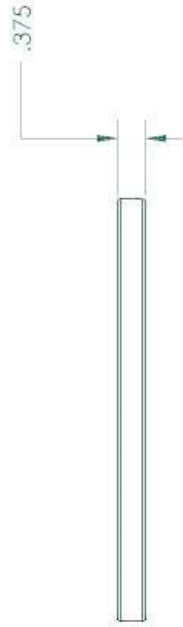
Material - Steel
Quantity - 1

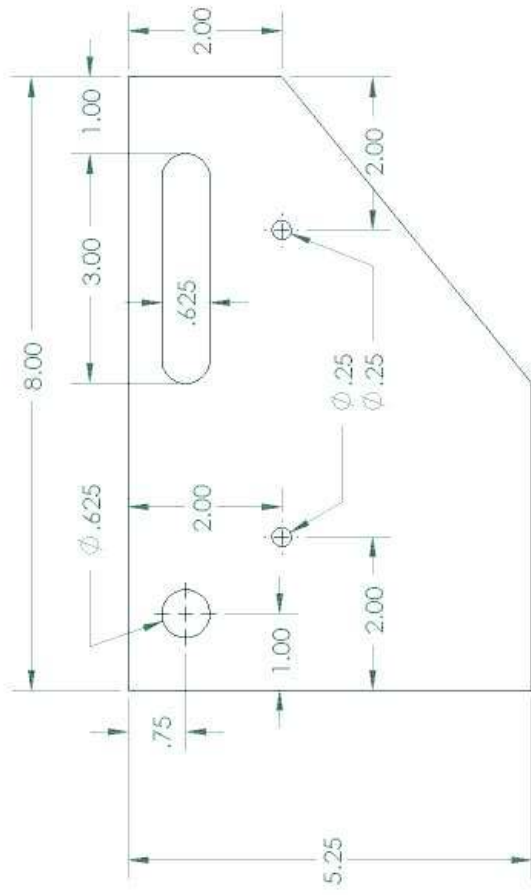


Material - Aluminium
Quantity - 1



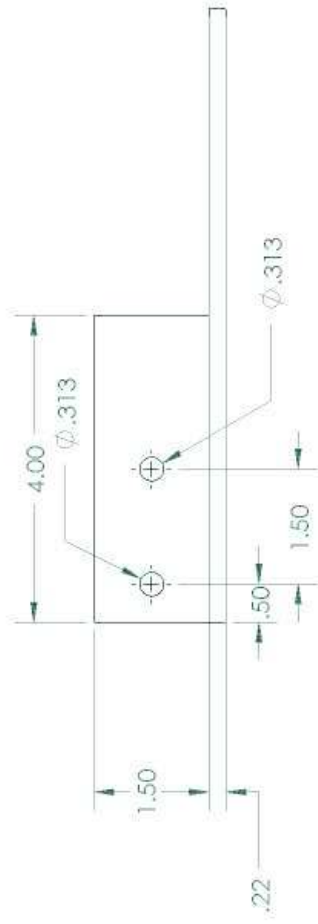
Material - Aluminium
 Quantity - 1
 **Radius center hole and
 edges of plate

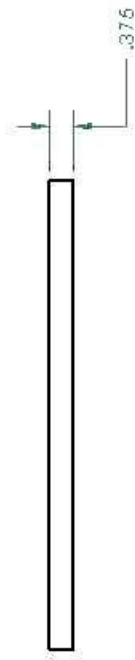
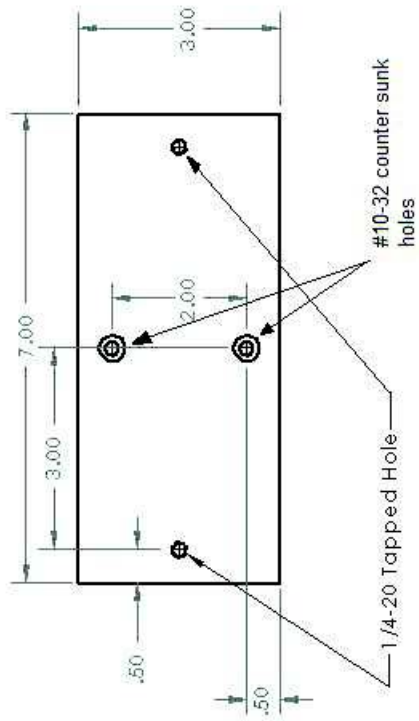




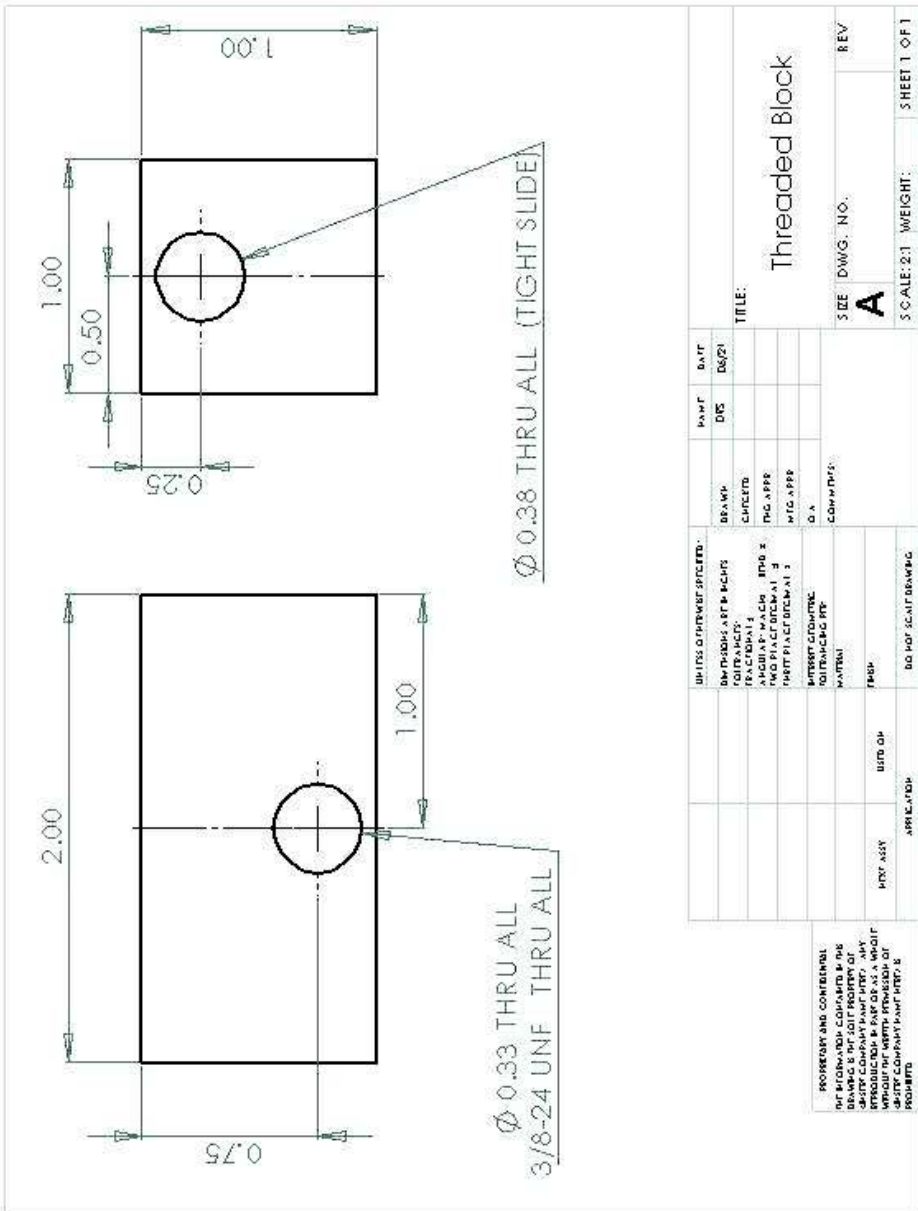
Material - Steel
 Quantity - 1

** Make from 8x11.5 C-Channel





Material - aluminium
Quantity - 1

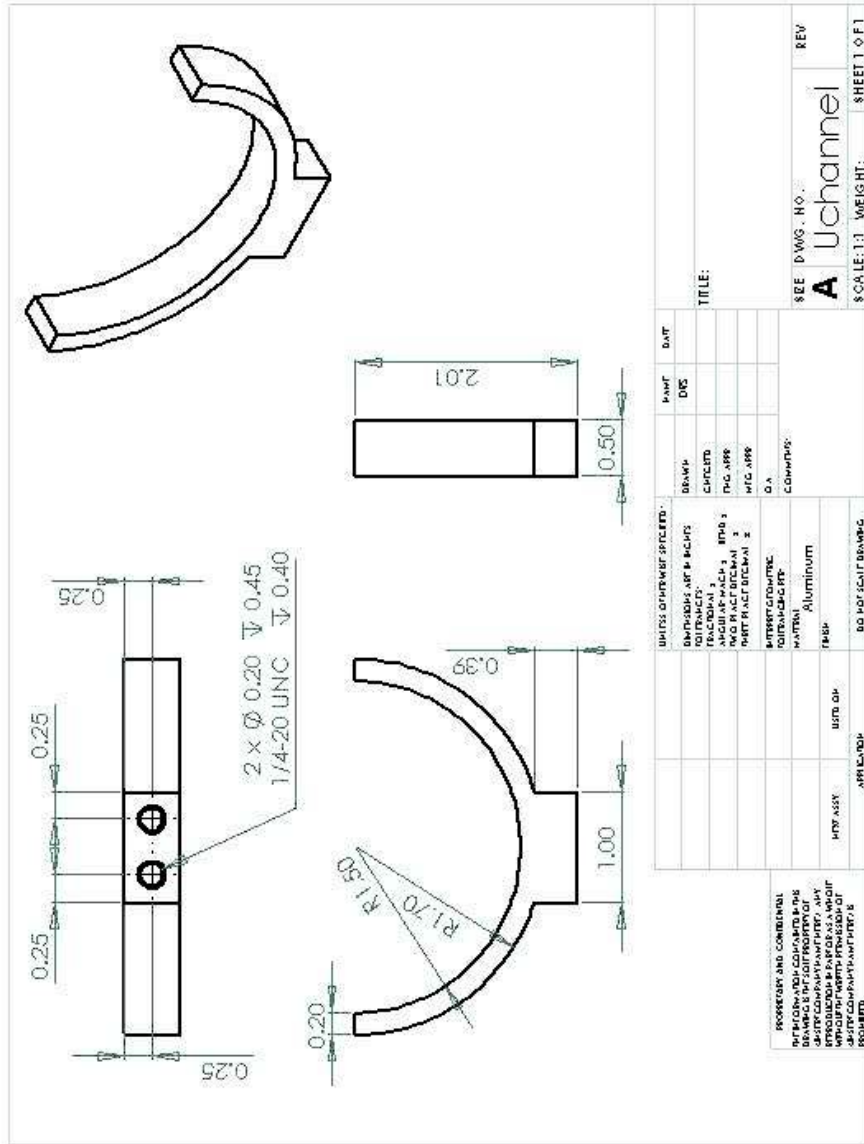


PROSESSOR AND CONTAINER
 NOT BE CONSIDERED COMPARTS & THIS
 DRAWING IS THE SOLE PROPERTY OF
 THE COMPANY AND IS NOT TO BE REPRODUCED
 WITHOUT THE WRITTEN PERMISSION OF
 THE COMPANY. PART NUMBER IS
 1000000

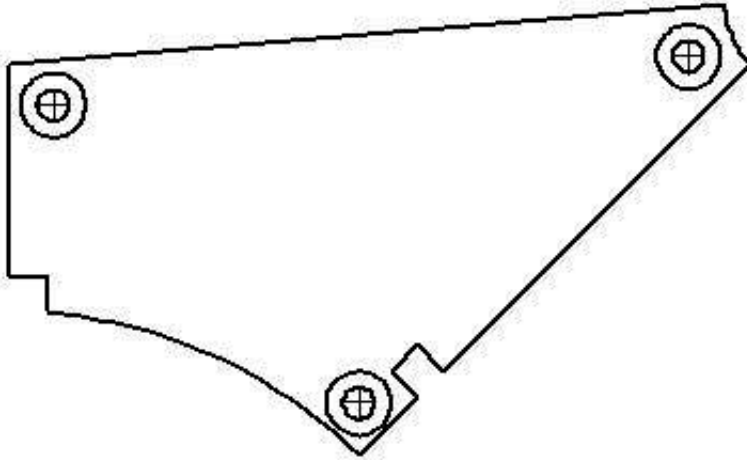
UNITS OF MEASURE SPECIFIED:	DESIGN	DATE
DEPARTMENTS: APPR & ECLIPS	DESIGN	DATE
TOLERANCES:	DESIGN	DATE
ANGULARS: MAXIMUM	DESIGN	DATE
TWO PLACE DECIMAL	DESIGN	DATE
THREE PLACE DECIMAL	DESIGN	DATE
INTERSECTING CONTINUOUS	DESIGN	DATE
INTERSECTING POINT	DESIGN	DATE
MATERIAL	DESIGN	DATE
FINISH	DESIGN	DATE
DO NOT SCALE DRAWING	DESIGN	DATE
DATE ASSEMBLY	DESIGN	DATE
APPROVAL	DESIGN	DATE
DATE OF DRAWING	DESIGN	DATE

Threaded Block

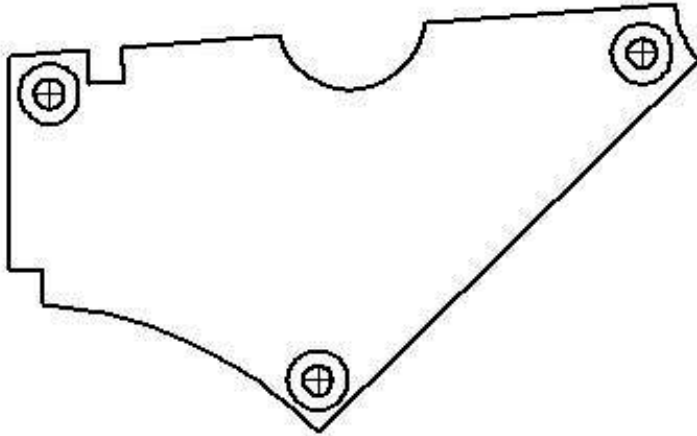
SIZE DWG. NO. **A** REV
 SCALE: 2:1 WEIGHT: SHEET 1 OF 1



Heating System Parts



<p>UNLESS OTHERWISE SPECIFIED:</p> <p>DRAWING: PART # RP</p> <p>CONTRACT: RP</p> <p>PROJECT: RP</p> <p>APPLIC: RP</p> <p>REV: RP</p> <p>DATE: RP</p> <p>BY: RP</p> <p>CHECKED: RP</p> <p>APPROVED: RP</p> <p>SCALE: 1:1</p>		<p>REV</p>
<p>PROPERTY AND CONFIDENTIALITY NOTICE: THIS DRAWING IS THE PROPERTY OF JERRY'S COMPANY AND IS NOT TO BE REPRODUCED OR TRANSMITTED IN ANY FORM OR BY ANY MEANS, ELECTRONIC OR MECHANICAL, WITHOUT THE WRITTEN PERMISSION OF JERRY'S COMPANY. VIOLATION IS PROHIBITED.</p>		<p>SIZE: DWG. NO. A</p>
<p>APPLICATION: RP</p>		<p>SCALE: 1:1 WEIGHT: SHEET 1 OF 1</p>
<p>UNLESS OTHERWISE SPECIFIED:</p> <p>DRAWING: PART # RP</p> <p>CONTRACT: RP</p> <p>PROJECT: RP</p> <p>APPLIC: RP</p> <p>REV: RP</p> <p>DATE: RP</p> <p>BY: RP</p> <p>CHECKED: RP</p> <p>APPROVED: RP</p> <p>SCALE: 1:1</p>	<p>REV</p>	<p>SIZE: DWG. NO. A</p>
<p>PROPERTY AND CONFIDENTIALITY NOTICE: THIS DRAWING IS THE PROPERTY OF JERRY'S COMPANY AND IS NOT TO BE REPRODUCED OR TRANSMITTED IN ANY FORM OR BY ANY MEANS, ELECTRONIC OR MECHANICAL, WITHOUT THE WRITTEN PERMISSION OF JERRY'S COMPANY. VIOLATION IS PROHIBITED.</p>	<p>APPLICATION: RP</p>	<p>SCALE: 1:1 WEIGHT: SHEET 1 OF 1</p>



Left Top Piece

\$ DE DWG. NO.

A

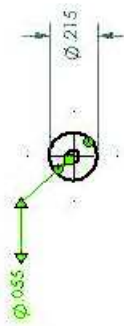
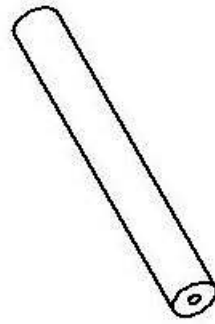
REV

\$ SCALE: 1:2 WEIGHT: \$ SHEET 1 OF 1

UNITS OF MEASURE SPECIFIED	DATE	DATE	DATE
DESIGNER: [blank]	DATE: [blank]	DATE: [blank]	DATE: [blank]
CHECKED: [blank]	DATE: [blank]	DATE: [blank]	DATE: [blank]
APPROVED: [blank]	DATE: [blank]	DATE: [blank]	DATE: [blank]
PROJECT: [blank]	DATE: [blank]	DATE: [blank]	DATE: [blank]
COMPANY: [blank]	DATE: [blank]	DATE: [blank]	DATE: [blank]
MATERIAL: [blank]	DATE: [blank]	DATE: [blank]	DATE: [blank]
FINISH: [blank]	DATE: [blank]	DATE: [blank]	DATE: [blank]
UNIT OF MEASURE: [blank]	DATE: [blank]	DATE: [blank]	DATE: [blank]
SCALE: [blank]	DATE: [blank]	DATE: [blank]	DATE: [blank]
WEIGHT: [blank]	DATE: [blank]	DATE: [blank]	DATE: [blank]
SHEET: [blank]	DATE: [blank]	DATE: [blank]	DATE: [blank]

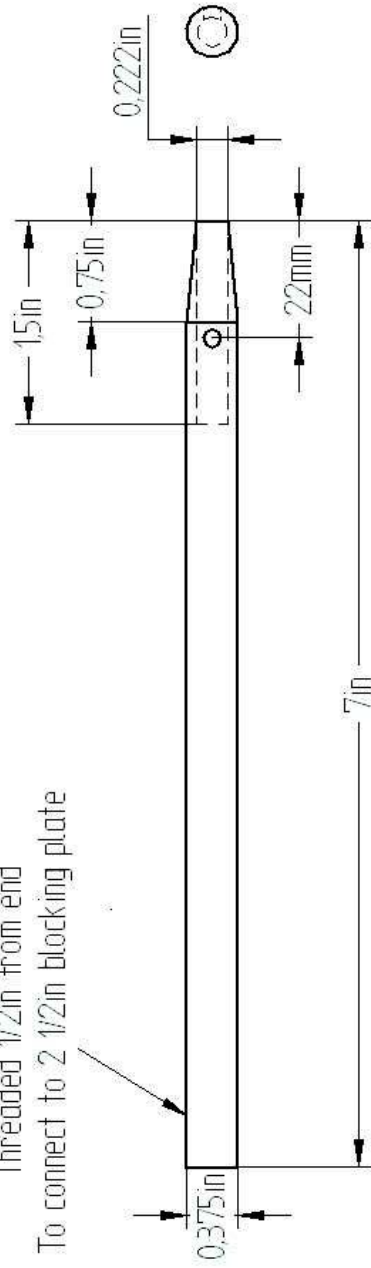
PROPERTY AND CONFIDENTIALITY INFORMATION CONTAINED IN THIS DRAWING IS THE SOLE PROPERTY OF GEORGE COMPANY. ANY REPRODUCTION OR TRANSMISSION OF THIS DRAWING WITHOUT THE WRITTEN PERMISSION OF GEORGE COMPANY IS STRICTLY PROHIBITED.

Ignition & Injection System Parts

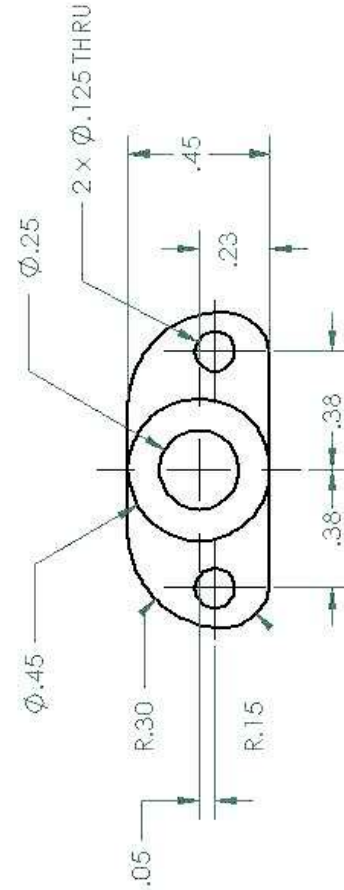
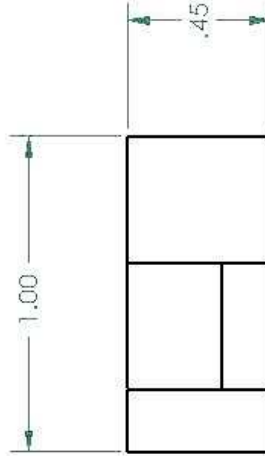
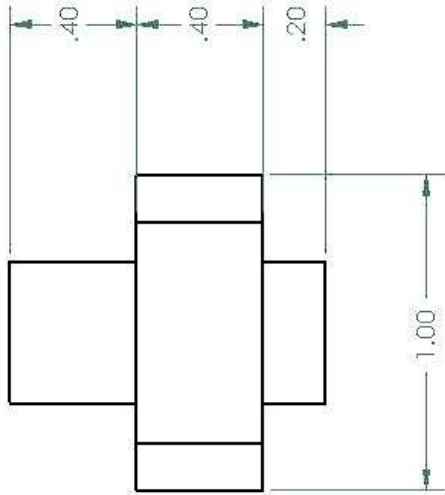
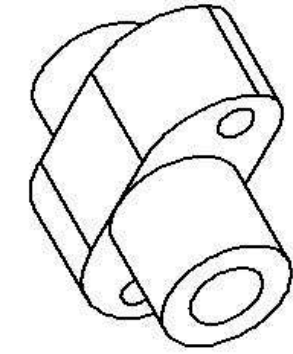


mild steel
qty 5

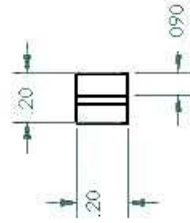
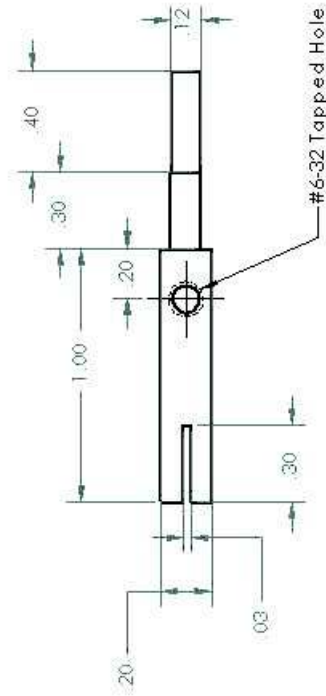
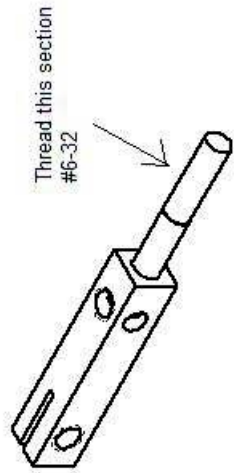
Threaded 1/2in from end
To connect to 2 1/2in blocking plate



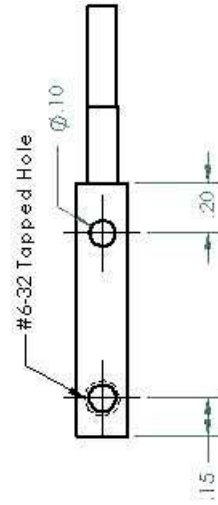
Drawing Name: Filament Holder
Designed By: Sean Fabbro Tel# 204-795-7989
Date: August 14, 2007
Material: Stainless Steel

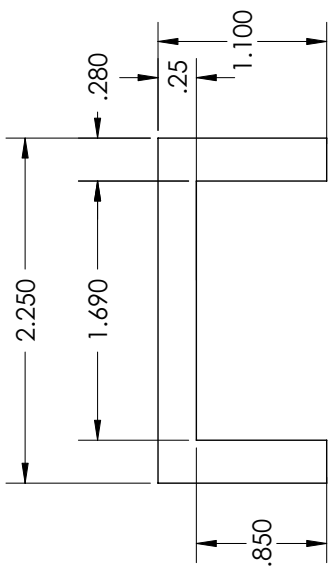
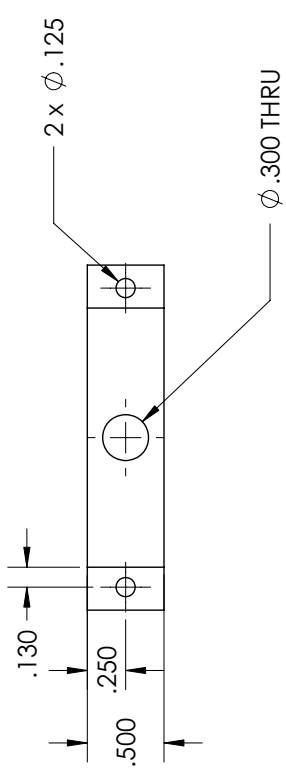
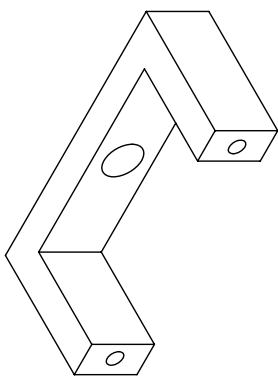


UNLESS OTHERWISE SPECIFIED:		NAME	DATE	Sean Fabbro Ph# 795-7999	
DIMENSIONS ARE IN INCHES	DRAWN	July 8, 2008	TITLE: Ignition Head		
TOLERANCES:	CHECKED		SIZE DWG. NO. REV		
FRACTIONALLY	ENG APPR.		Ignition Head		
ANGULAR DIM CH 1 BEND 1	MFG APPR.		SCALE: 2:1 WEIGHT: SHEET 1 OF 1		
TWO PLACES DECIMAL 1	Q. A.		INSULATIVE material		
THREE PLACES DECIMAL 1	COMMENTS:	Insulative material			
INTERPRET GEOMETRIC TOLERANCING PER MATERIAL	FINISH	DO NOT SCALE DRAWING			
PROPRIETARY AND CONFIDENTIAL	APPLICATION	4			
THE INFORMATION CONTAINED IN THIS DRAWING IS THE SOLE PROPERTY OF <INSERT COMPANY NAME HERE>. ANY REPRODUCTION IN PART OR AS A WHOLE WITHOUT THE WRITTEN PERMISSION OF <INSERT COMPANY NAME HERE> IS PROHIBITED.	5	3			
		2			
		1			



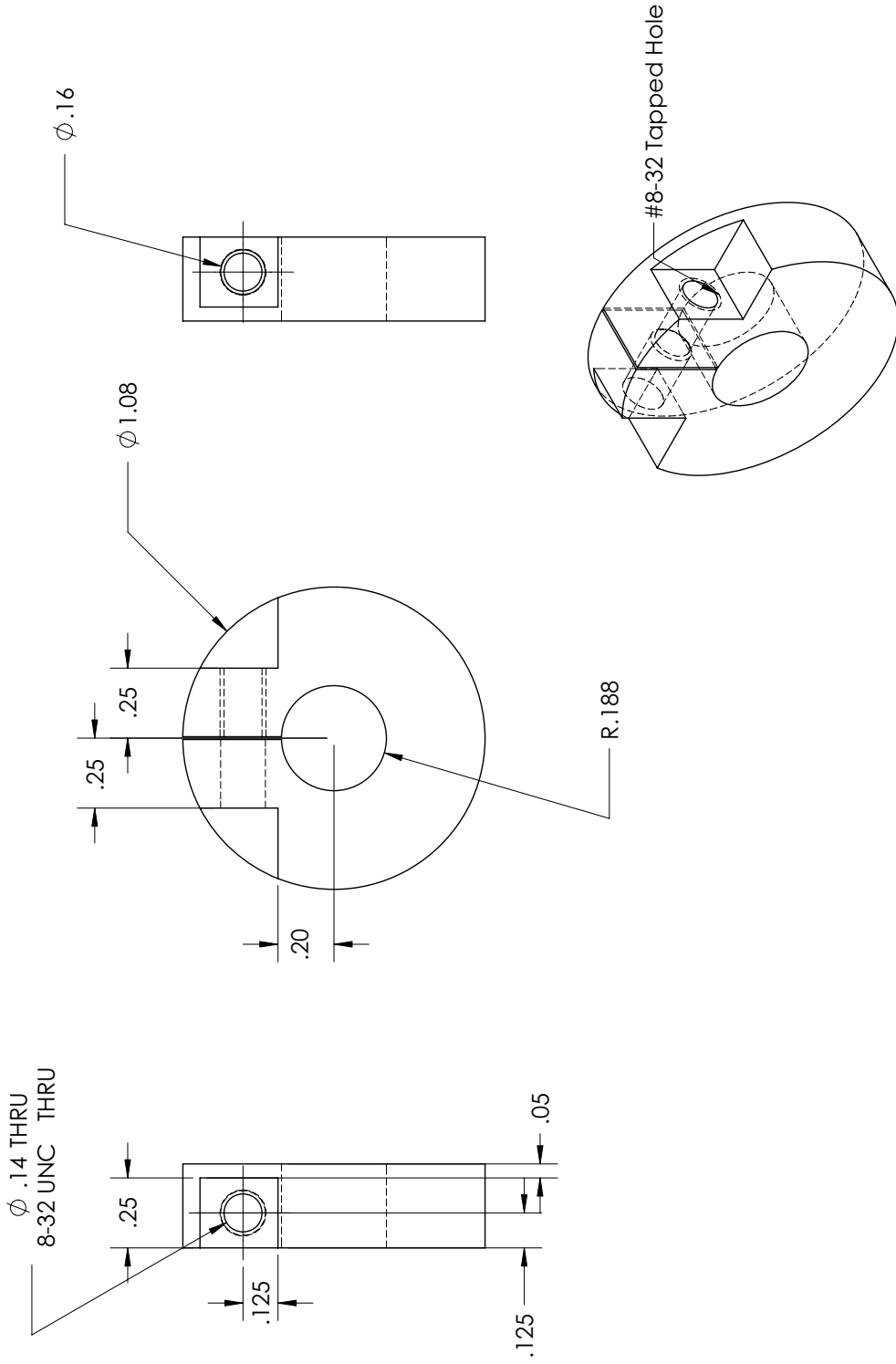
Stainless Steel
Quantity 2
Designer Sean - 795-7999



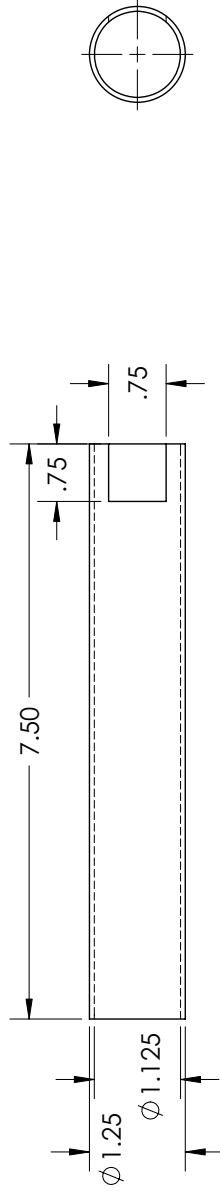
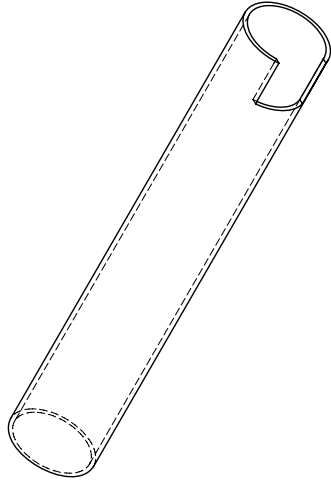


ITEM NO.	PART NUMBER	Material	QTY.
1	stepper backing V2	Aluminium	1

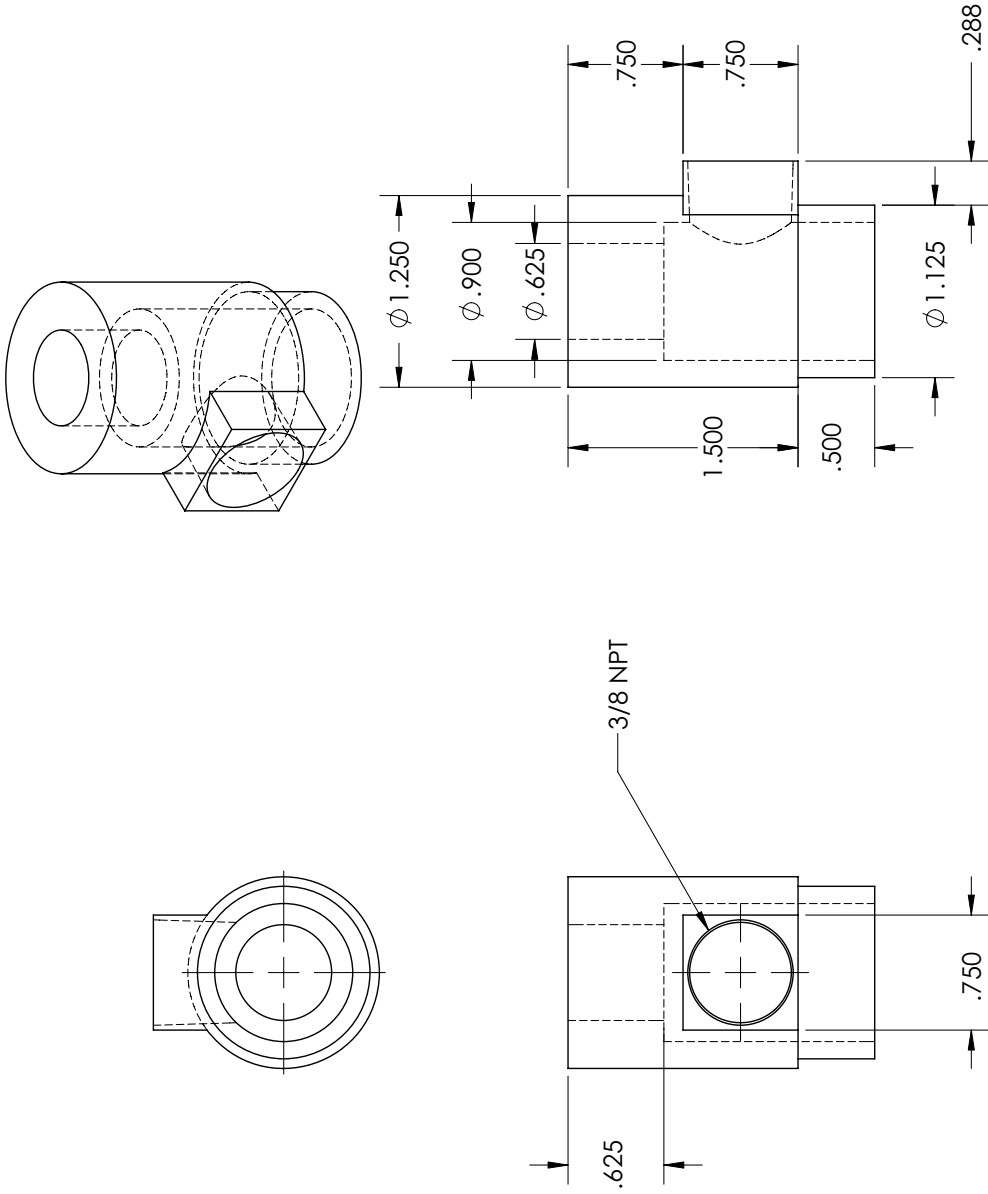
SolidWorks Student License
 Academic Use Only



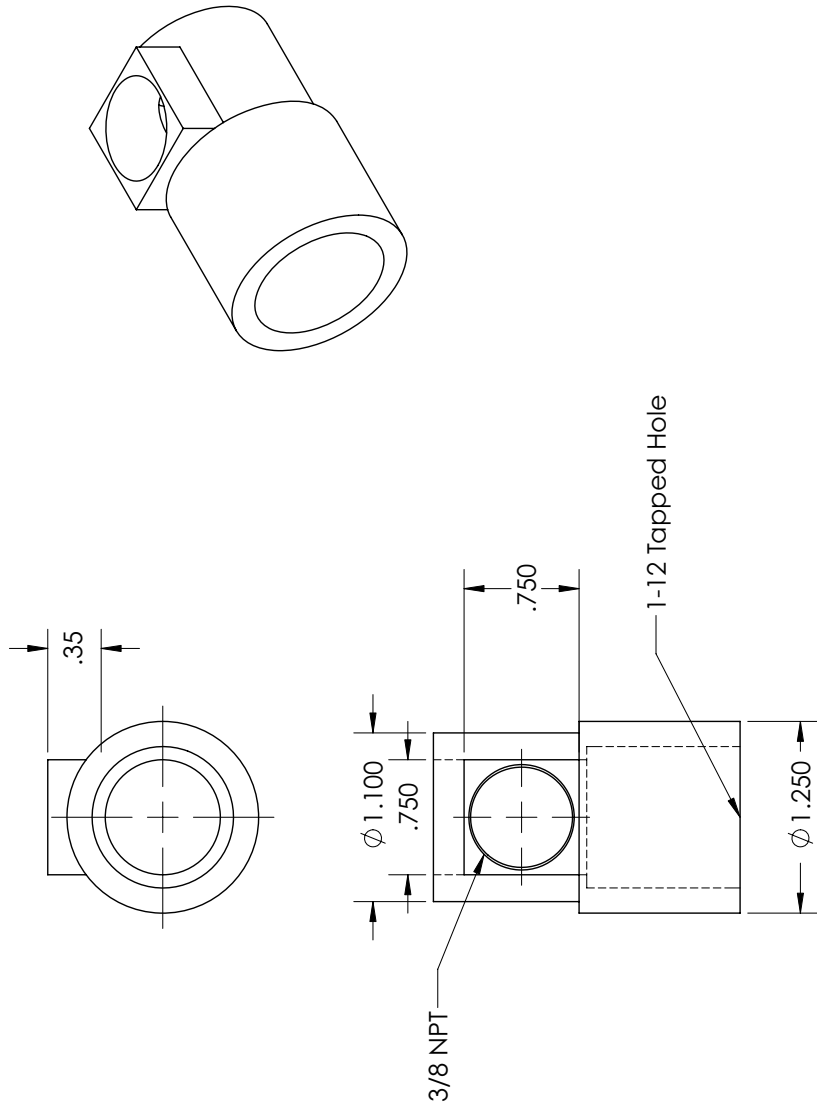
ITEM NO.	PART NUMBER	Material	QTY.
1	retractor plate V2	Aluminium	1



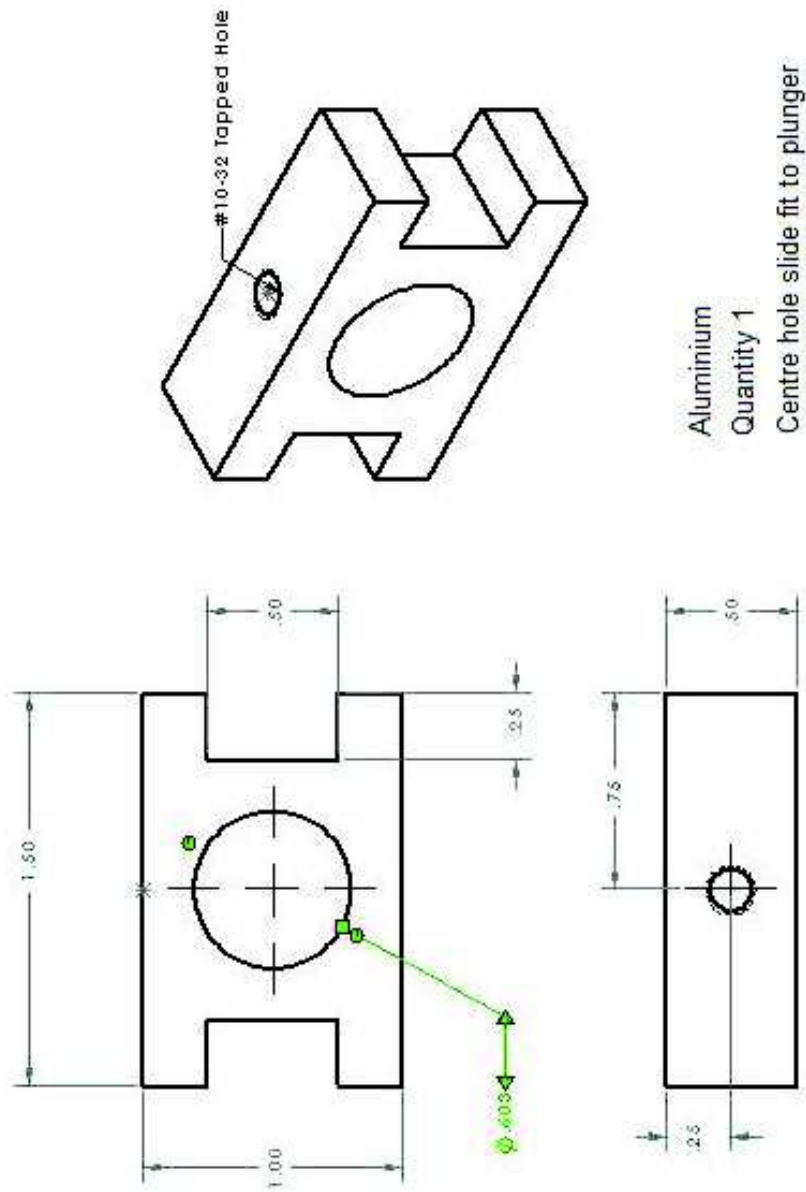
ITEM NO.	PART NUMBER	Material	QTY.
1	Retraction Tube V2	Aluminium	1

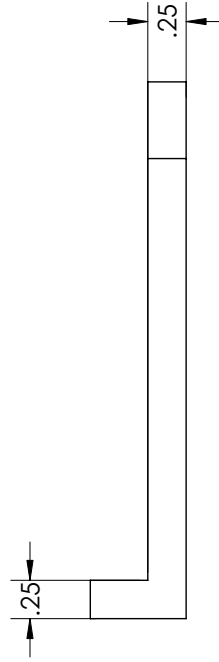
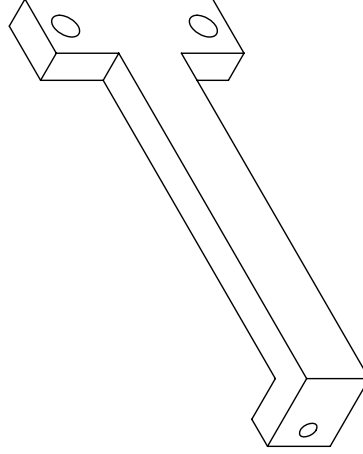
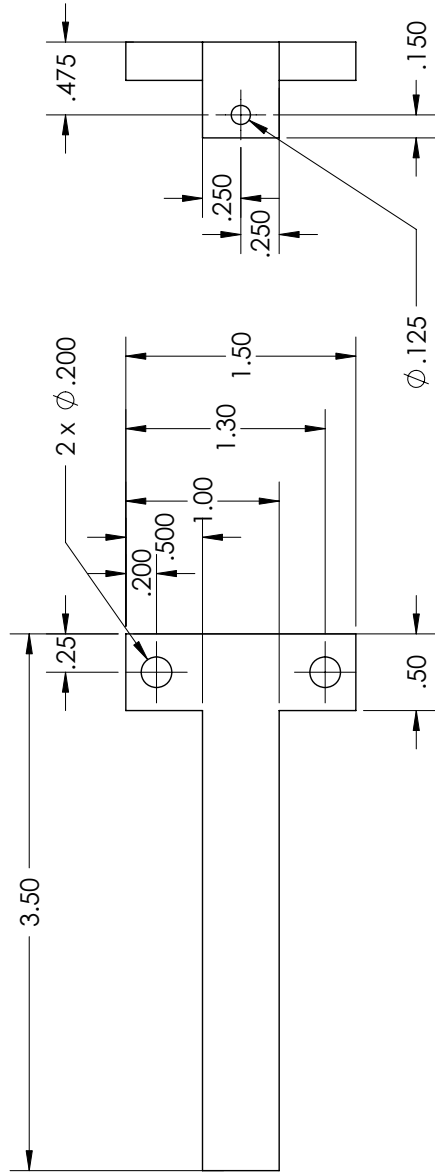


ITEM NO.	PART NUMBER	Material	QTY.
1	retractor tube end V2	Aluminium	1



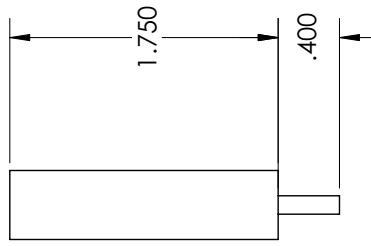
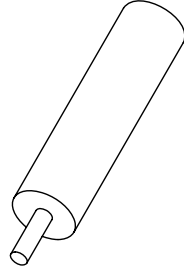
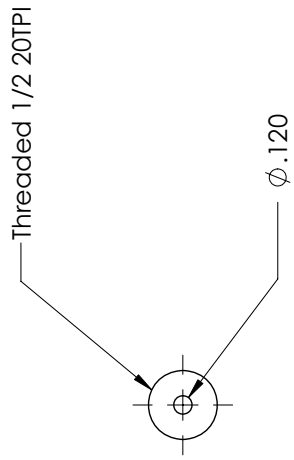
ITEM NO.	PART NUMBER	Material	QTY.
1	retraction cylinder adapter	Aluminium	1





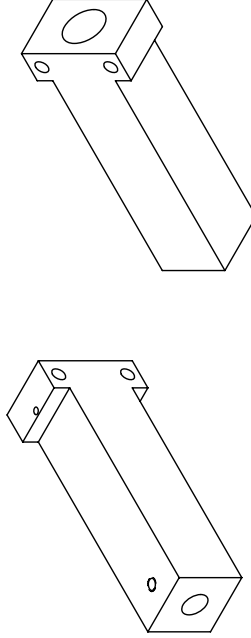
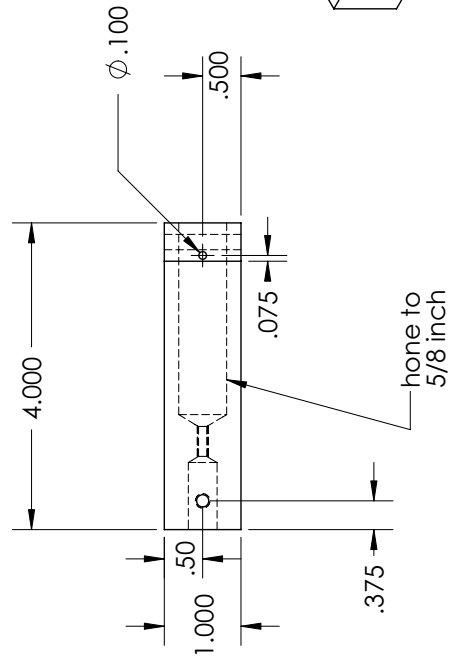
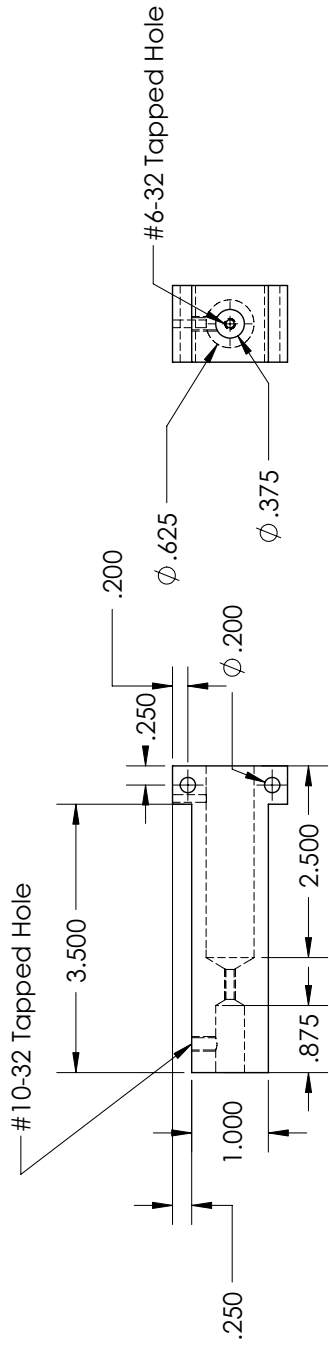
ITEM NO.	PART NUMBER	Material	QTY.
1	stepper side support V2	Aluminium	2

**SolidWorks Student License
Academic Use Only**

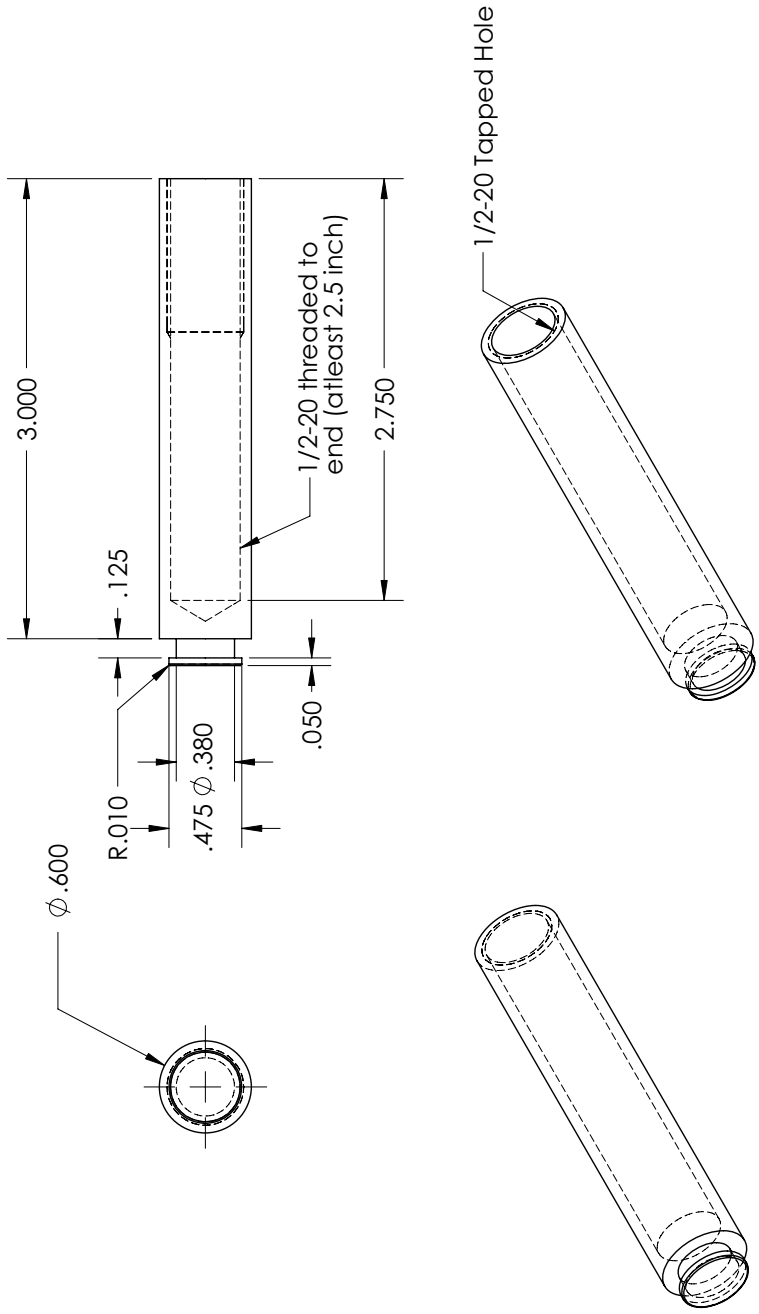


ITEM NO.	PART NUMBER	Material	QTY.
1	threaded rod V2	Stainless Steel	1

**SolidWorks Student License
Academic Use Only**

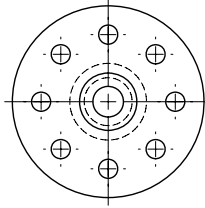
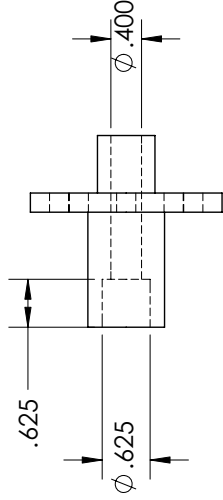
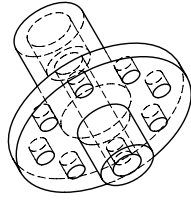


ITEM NO.	PART NUMBER	Material	QTY.
1	Plunger case V2	Aluminium	1



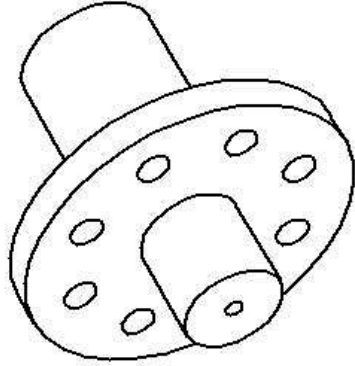
ITEM NO.	PART NUMBER	Material	QTY.
1	Plunger Injector V2	Stainless Steel	1

Chamber Port Adaptors

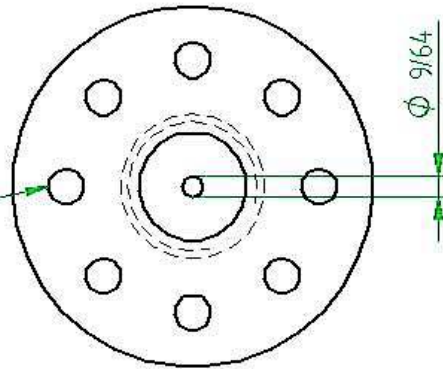
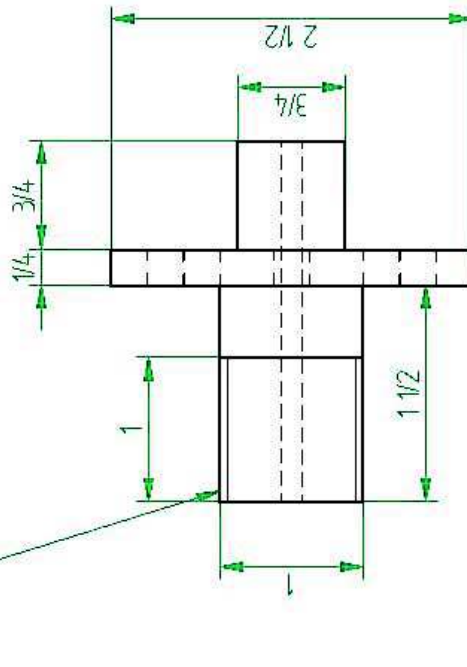


ITEM NO.	PART NUMBER	Material	QTY.
1	Injector to chamber adapter	Stainless Steel	1

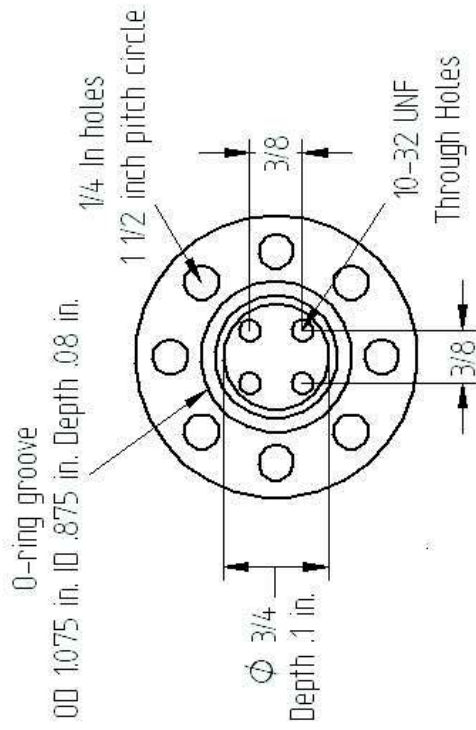
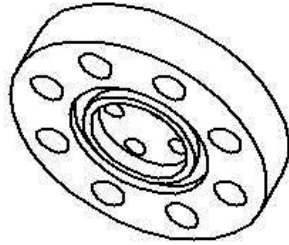
Date: June 6, 2006 Version: 1.1



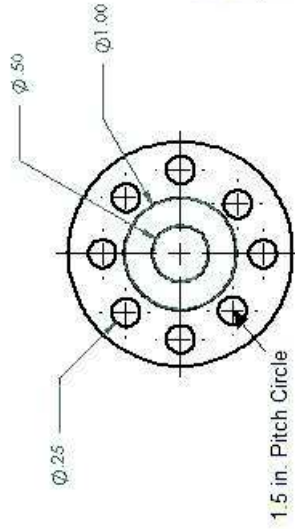
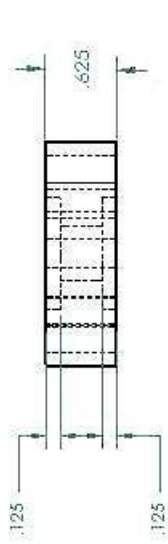
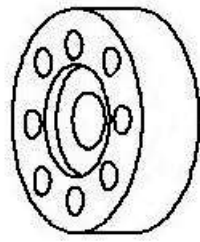
8 thru holes evenly spaced
1/4 inch hole 1.75 inch pitch circle



SOLID EDGE PART NUMBER	
Title:	Injector Adaptor
Material:	Stainless Steel
Author:	Sean Fabbro

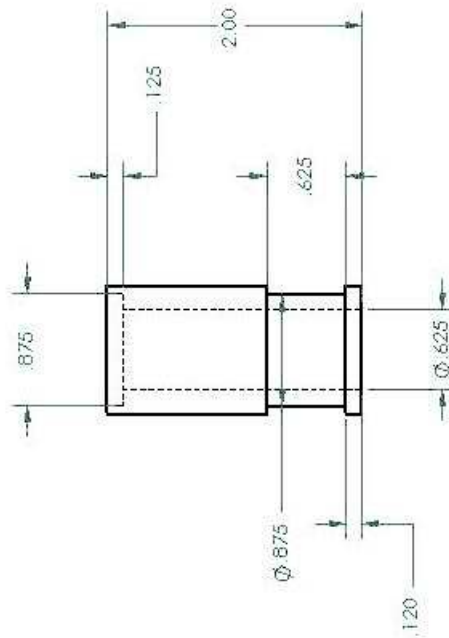
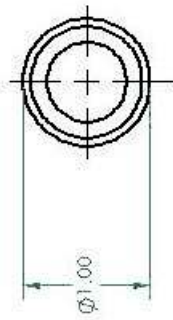
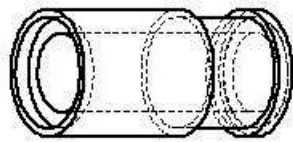


Drawing Name: High Pressure Power Coupler
Designed By: Sean Fabbro Tel# 204-795-7989
Date: July 27, 2007
Material: Macor



Part Name - New Injector Seal Backing
Material - Stainless Steel

* All dimensions are in inches unless otherwise stated

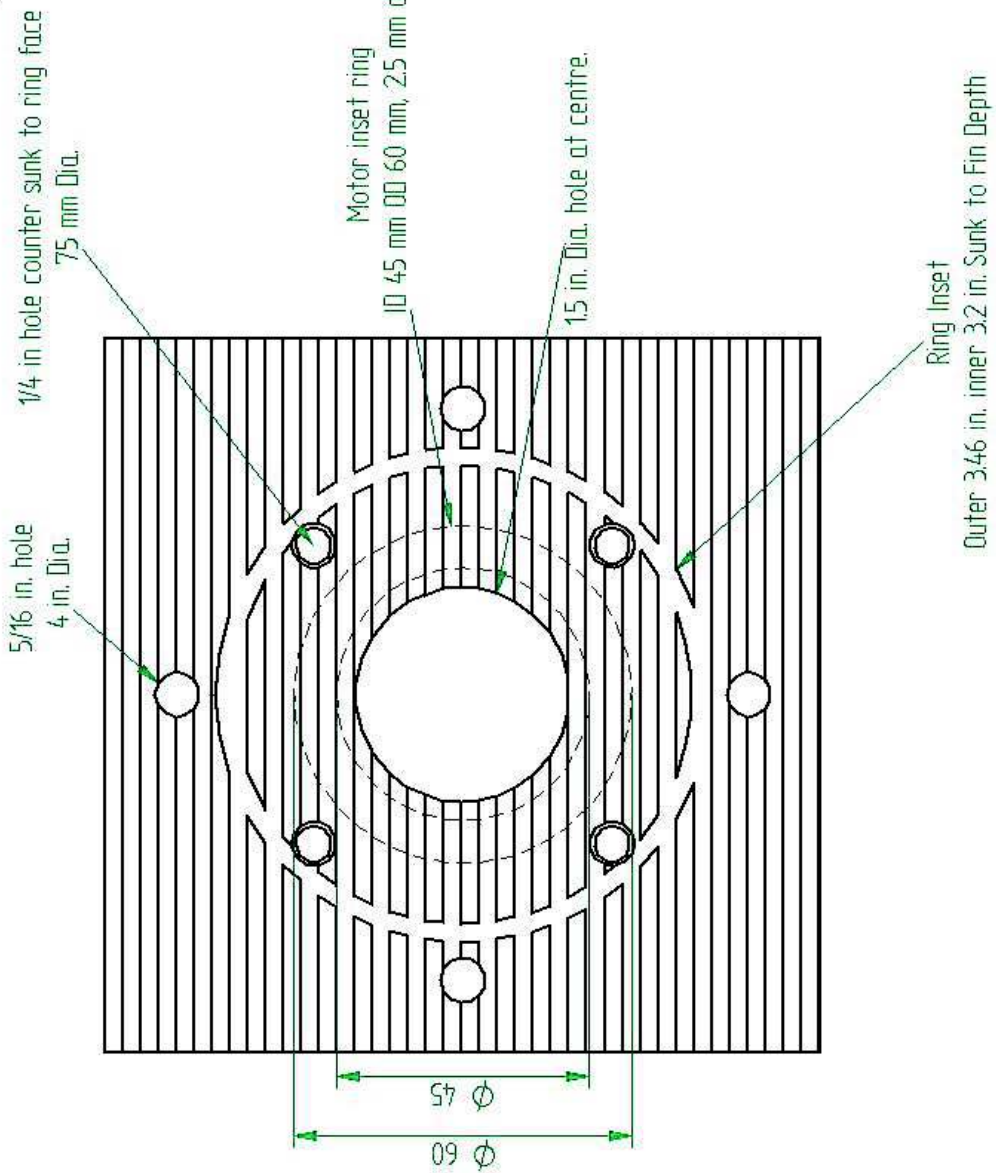
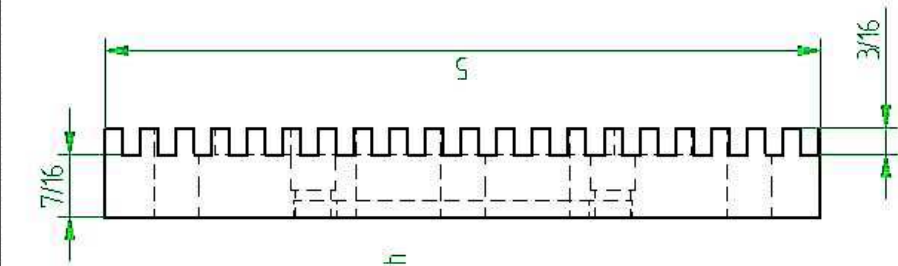


Part Name - New Injector Alignment Body
Material - Stainless Steel

* All dimensions are in inches unless otherwise stated

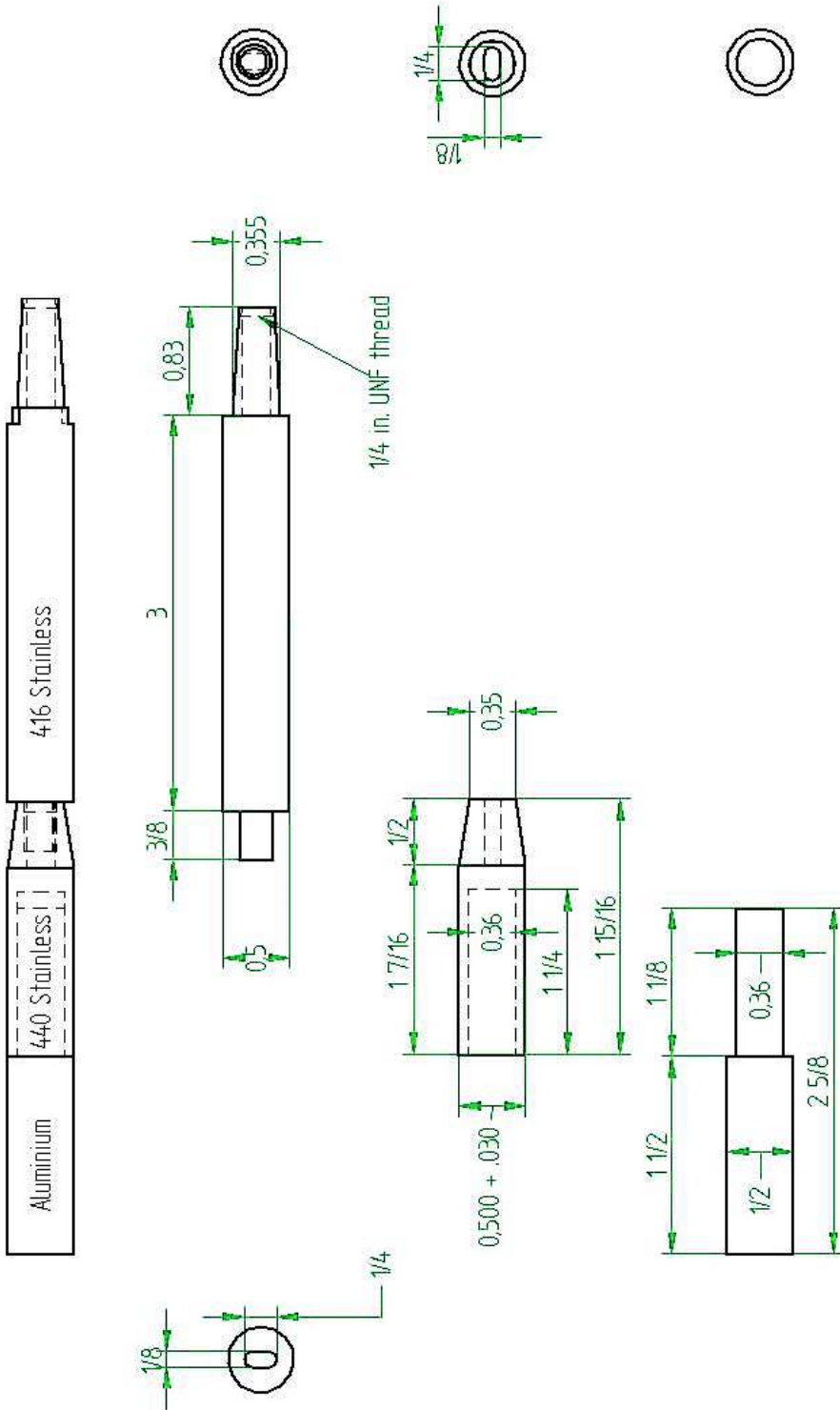
Fan Assembly Parts

Date: April 28, 2006 Version: 1.1



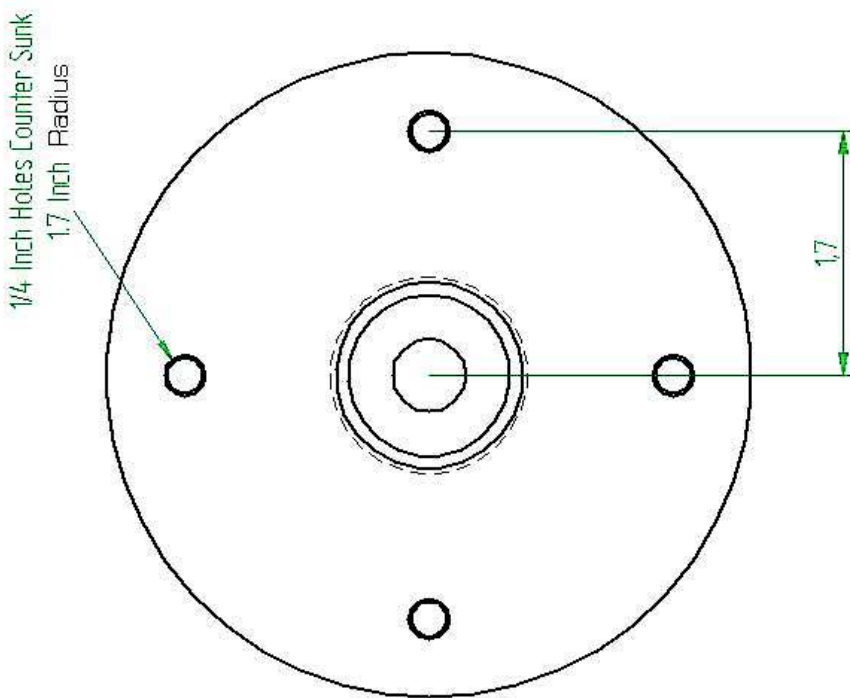
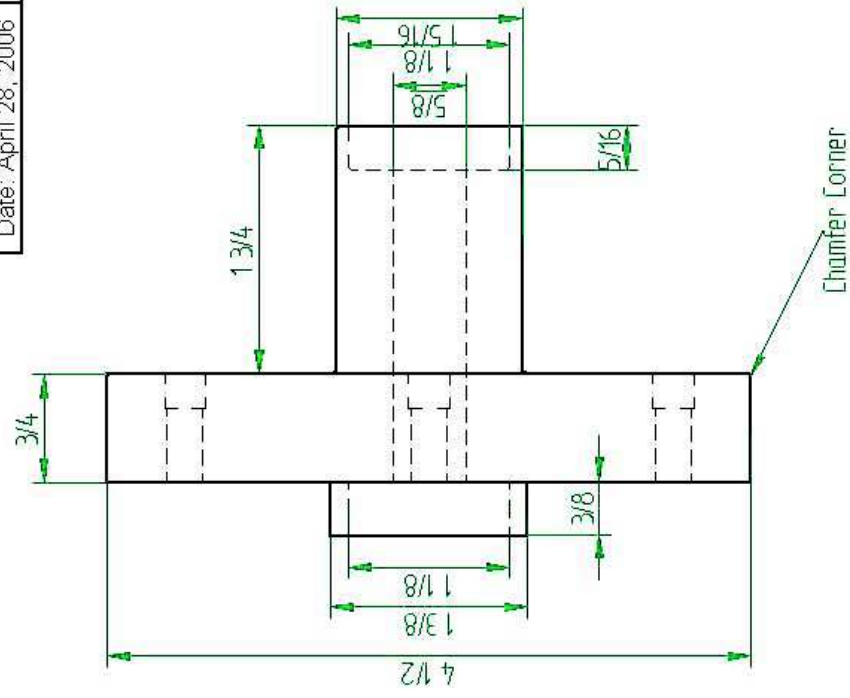
SOLID EDGE user manuals	
Title:	Housing Plate Motor Side
Material:	Aluminium
Author:	Sean Fabbro

Date: July 20, 2006 Version 3.1



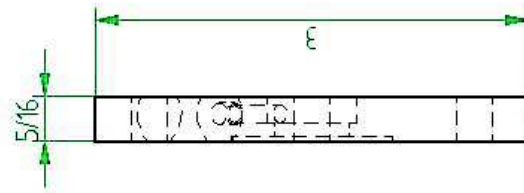
SOLID EDGE 16-214 011016	
Title:	Rod Assembly
Material:	440 Stainless Steel
Author:	Sean Fabbro

Date: April 28, 2006 Version: 1.1



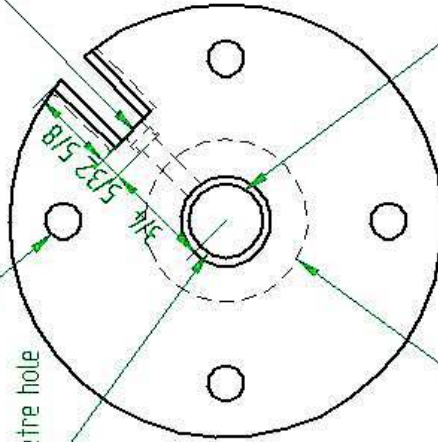
SOLID EDGE PART NUMBER	
Title:	Shaft Housing
Material:	Stainless Steel
Author:	Sean Fabbro

1/8 in. hole with #10-32 threaded entrance
 .375 counter sunk with seal retainer part a



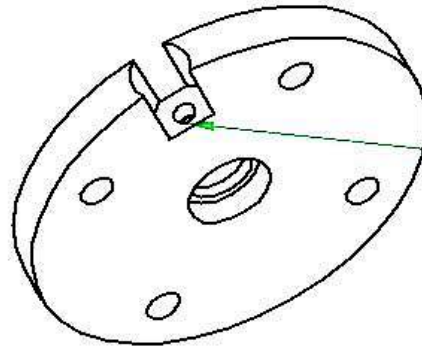
1/4 in. hole 2 1/4 in. pitch circle

.505 - .510 in diameter hole



5/8 in. diameter hole
 3/16 in. depth

1 1/8 in. diameter hole
 .026 in. depth



1/8 in. hole
 located 1/8 in. from front face

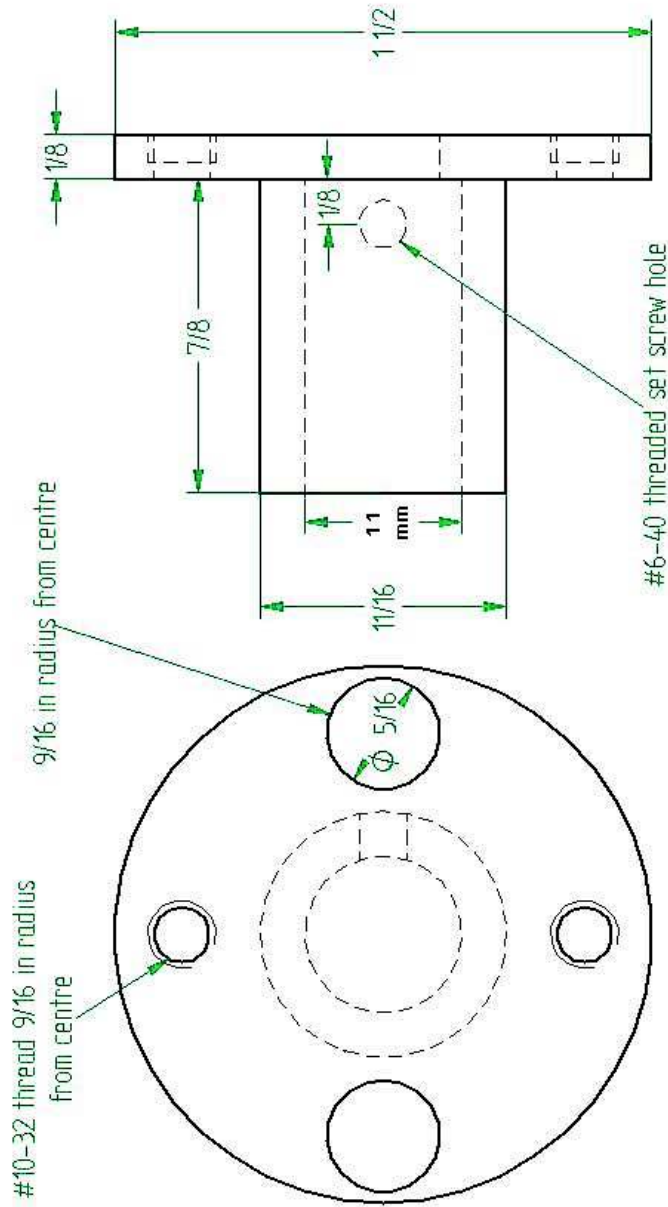
SOLID EDGE
 PART NUMBER

Title: Seal Retainer Part B

Material: Aluminium

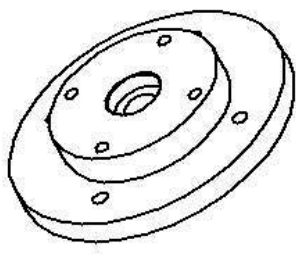
Author: Sean Fabbro

Date: April 28, 2006 Version: 1.1

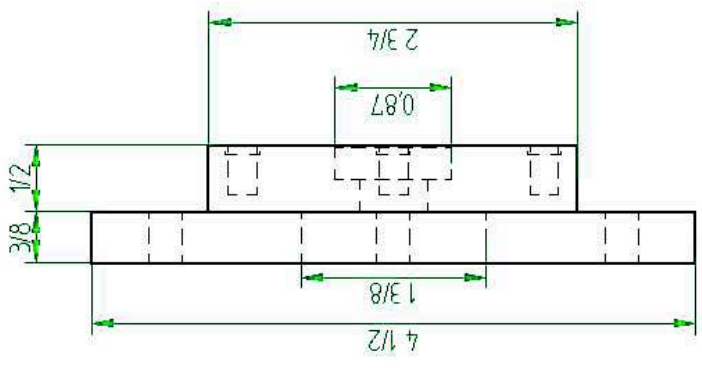


SOLID EDGE PART NUMBER	
Title:	Coupler Sdesign
Material:	Stainless Steel
Author:	Sean Fabbro

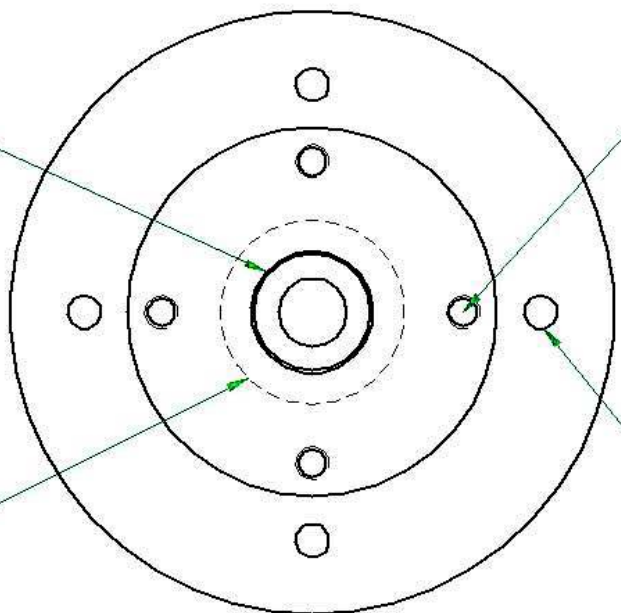
REV	DESCRIPTION	DATE	APPROVED



.870 inch hole .260 inch depth
inner round (.025 in max) outer chamfer (.030 in max)



1 3/8 inch hole 3/8 inch depth

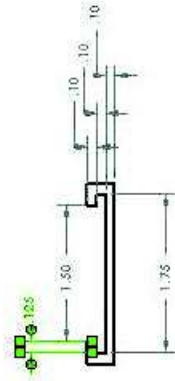
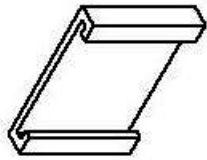


1/4 inch UNF 2 1/4 inch Centre

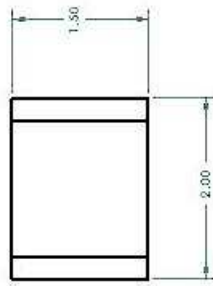
1/4 inch hole 1.7 inch radius

DATE	DATE	SOLID EDGE	
REVISED	DESIGNED	DR - PA SALDINE	
FILED	DATE	TITLE	
FILED	DATE	SIZE 1/4 IN	
UNLESS OTHERWISE SPECIFIED		FINISH: UNFINISHED	
DIMENSIONS ARE IN MILLIMETERS		SCALE: 1:1	
DIMENSIONS ARE IN INCHES		SHEET 1 OF 1	
2 IN X 3 1/2 IN X .0000		WEIGHT:	

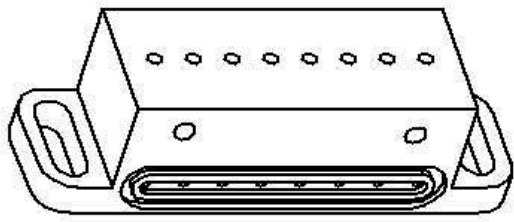
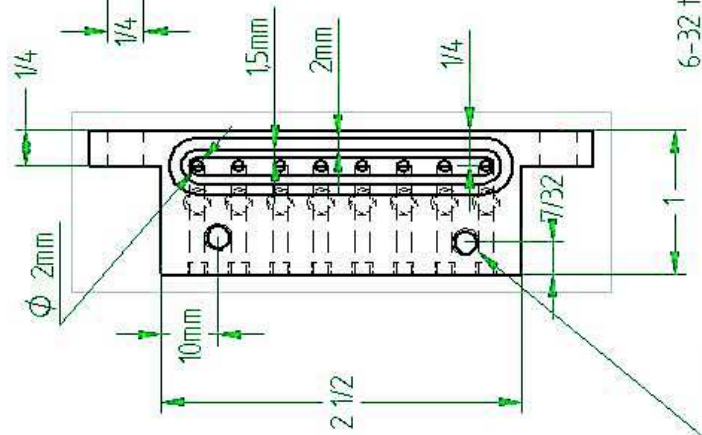
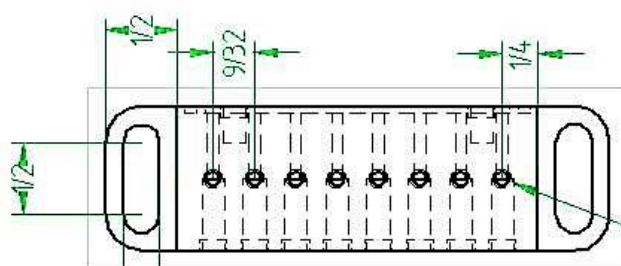
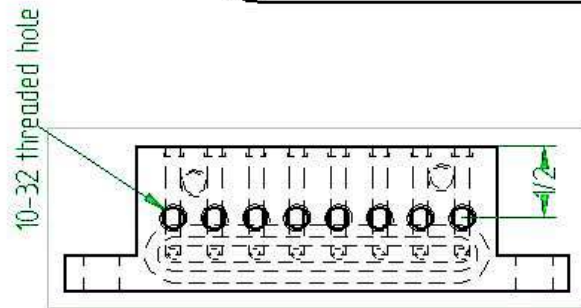
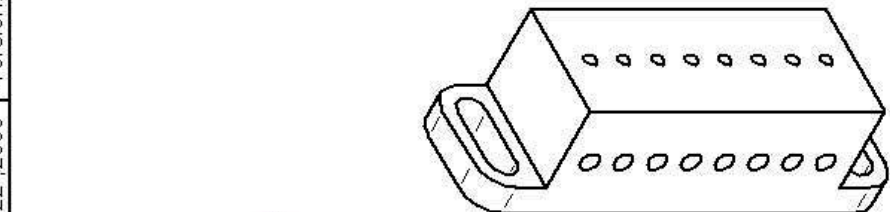
Miscellaneous Parts



Plastic
Qty 1

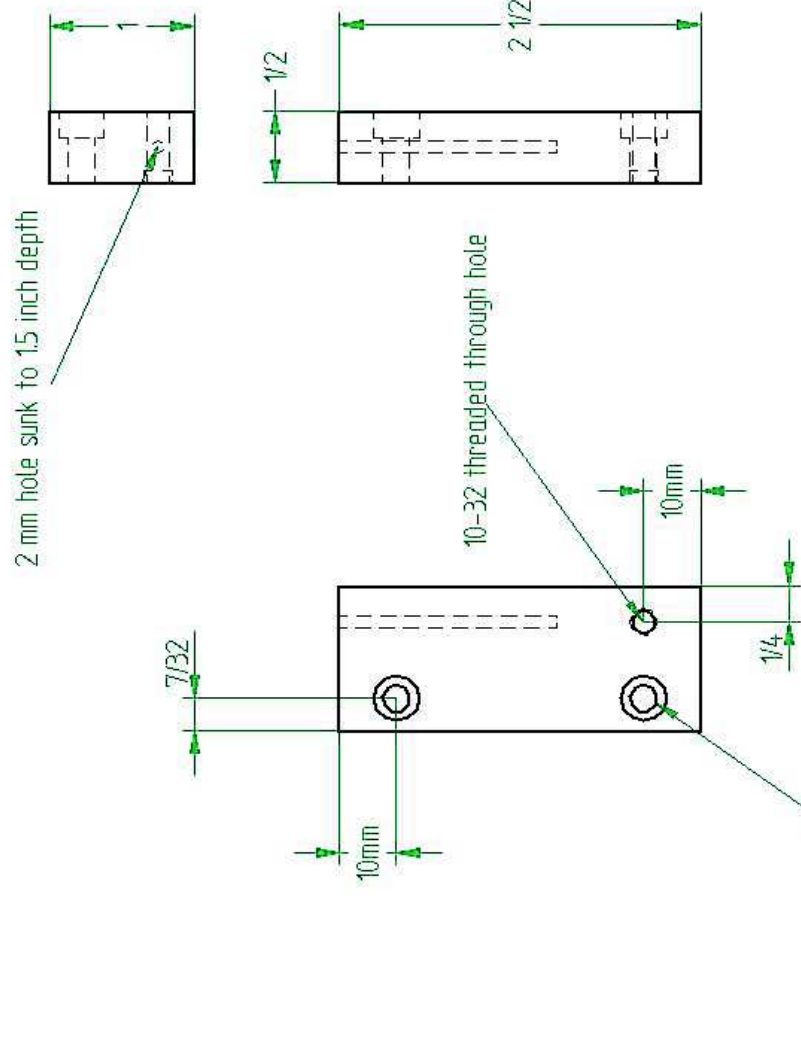
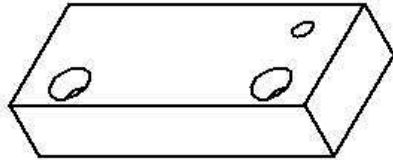


Date: Aug. 22, 2006 Version: 1.1



10-32 threaded hole

SOLID EDGE PART NUMBER	
Title:	Flow Block
Material:	Aluminium
Author:	Sean Fabbro



SOLID EDGE sheet format	
Title:	Flow Block Side Plate
Material:	Aluminium
Author:	Sean Fabbro